



Mathematical Modelling and Numerical Simulation with Applications

ISSN Online : 2791-8564

Year : 2023

Volume : 3

Issue : 2

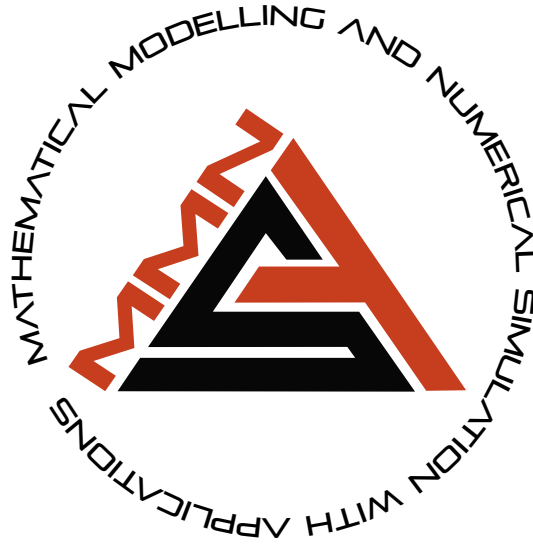


<https://dergipark.org.tr/en/pub/mmnsa>

Editor-in-Chief
Mehmet Yavuz, PhD

VOLUME: 3 ISSUE: 2
ISSN ONLINE: 2791-8564

June 2023
<https://dergipark.org.tr/en/pub/mmnsa>



MATHEMATICAL MODELLING AND NUMERICAL SIMULATION WITH APPLICATIONS

Editor-in-Chief and Publisher

Mehmet Yavuz
Department of Mathematics and Computer Sciences,
Faculty of Science, Necmettin Erbakan University,
Meram Yeniyol, 42090 Meram, Konya / TÜRKİYE
mehmetyavuz@erbakan.edu.tr

Editorial Board

Abdeljawad, Thabet
Prince Sultan University
Saudi Arabia

Agarwal, Praveen
Anand International College of Engineering
India

Aguilar, José Francisco Gómez
CONACyT- National Center for Technological Research
and Development
Mexico

Ahmad, Hijaz
International Telematic University Uninettuno
Italy

Arqub, Omar Abu
Al-Balqa Applied University
Jordan

Asjad, Muhammad Imran
University of Management and Technology
Pakistan

Atangana, Abdon
University of the Free State
South Africa

Baleanu, Dumitru
Cankaya University, *Türkiye*;
Institute of Space Sciences, Bucharest, *Romania*

Başkonuş, Hacı Mehmet
Harran University
Türkiye

Biswas, Md. Haider Ali
Khulna University
Bangladesh

Bonyah, Ebenezer
Department of Mathematics Education
Ghana

Bulai, Iulia Martina
University of Basilicata
Italy

Cabada, Alberto
University of Santiago de Compostela
Spain

Dassios, Ioannis
University College Dublin
Ireland

Eskandari, Zohreh
Shahrekord University
Iran

Flaut, Cristina
Ovidius University of Constanta
Romania

González, Francisco Martínez
Universidad Politécnica de Cartagena
Spain

Gürbüz, Burcu
Johannes Gutenberg-University Mainz, Institute of
Mathematics, *Germany*

Hammouch, Zakia
ENS Moulay Ismail University Morocco;
Thu Dau Mot University Vietnam and China Medical
University, *Taiwan*

Hristov, Jordan
University of Chemical Technology and Metallurgy
Bulgaria

Ibadula, Denis
Ovidius University of Constanta
Romania

Jafari, Hossein
University of Mazandaran, *Iran*;
University of South Africa, *South Africa*

Jajarmi, Amin
University of Bojnord
Iran

Jain, Shilpi
Poornima College of Engineering, Jaipur
India

Kaabar, Mohammed K.A.
Washington State University
USA

Kumar, Devendra
University of Rajasthan
India

Kumar, Sunil
National Institute of Technology
India

Lupulescu, Vasile
Constantin Brâncuși University of Târgu-Jiu
Romania

Merdan, Hüseyin
TOBB University of Economy and Technology
Türkiye

Mohammed S. Abdo
Hodeidah University, Al-Hodeidah, Department of
Mathematics
Yemen

Naik, Parvaiz Ahmad
School of Mathematics and Statistics, Xi'an Jiaotong
University, *China*

Noeiaghdam, Samad
Irkutsk National Research Technical University
Russian Federation

Owolabi, Kolade
Federal University of Technology
Nigeria

Otero-Espinar, Maria Victoria
University of Santiago de Compostela
Spain

Özdemir, Necati
Balıkesir University
Türkiye

Pinto, Carla M.A.
ISEP, *Portugal*

Povstenko, Yuriy
Jan Długosz University in Czestochowa
Poland

Qureshi, Sania
Mehran University of Engineering and Technology
Pakistan

Sabatier, Jocelyn
Bordeaux University
France

Safaei, Mohammad Reza
Florida International University
USA

Salahshour, Soheil
Bahçeşehir University
Türkiye

Sarı, Murat
Yıldız Technical University
Türkiye

Sarris, Ioannis E.
University of West Attica
Greece

Sene, Ndolane
Cheikh Anta Diop University
Senegal

Singh, Jagdev
JECRC University
India

Stamova, Ivanka
University of Texas at San Antonio
USA

Torres, Delfim F. M.
University of Aveiro
Portugal

Townley, Stuart
University of Exeter
United Kingdom

Valdés, Juan Eduardo Nápoles
Universidad Nacional del Nordeste
Argentina

Veerasha, Pundikala
Christ University
India

Weber, Gerhard-Wilhelm
Poznan University of Technology
Poland

Xu, Changjin
Guizhou University of Finance and Economics
China

Yalçınkaya, İbrahim
Necmettin Erbakan University
Türkiye

Yang, Xiao-Jun
China University of Mining and Technology
China

Yuan, Sanling
University of Shanghai for Science and Technology
China

Technical Editor

Kerim Sarıg ulr
Gazi University, Ankara / T RKİYE
kerimsarigul@gazi.edu.tr

English Editor

Abdulkadir  nal
School of Foreign Languages, Foreign Languages, Alanya
Alaaddin Keykubat University, Antalya / T RKİYE
abdulkadir.unal@alanya.edu.tr

Faruk T rk
Karamanođlu Mehmetbey University,
School of Foreign Languages,
Karaman / T RKİYE

Editorial Secretariat

Fatma  zlem Cořar
Department of Mathematics and Computer Sciences,
Faculty of Science, Necmettin Erbakan University,
Meram Yeniyol, 42090 Meram, Konya / T RKİYE

M zeyyen Akman
Department of Mathematics and Computer Sciences,
Faculty of Science, Necmettin Erbakan University,
Meram Yeniyol, 42090 Meram, Konya / T RKİYE

Contents

Research Articles

- 1 A study on the solutions of (1+1)-dimensional Mikhailov-Novikov-Wang equation
Şeyma Tülüce Demiray, Uğur Bayrakçı 101-110
- 2 Analysis of a model to control the co-dynamics of Chlamydia and Gonorrhoea
using Caputo fractional derivative
Udoka Benedict Odionyenma, Nometa Ikenna, Bolarinwa Bolaji 111-140
- 3 Generative adversarial network for load data generation: Türkiye energy market case
Bilgi Yılmaz 141-158
- 4 Artificial intelligence-assisted detection model for melanoma diagnosis using
deep learning techniques
Hediye Orhan, Emrehan Yavşan 159-169
- 5 A Caputo-Fabrizio fractional-order cholera model and its sensitivity analysis
Idris Ahmed, Ali Akgül, Fahd Jarad, Poom Kumam, Kamsing Nonlaopon 170-187



RESEARCH PAPER

A study on the solutions of (1+1)-dimensional Mikhailov-Novikov-Wang equation

Seyma Tuluçe Demiray ^{1,‡} and Ugur Bayrakci ^{1,*,‡}

¹Department of Mathematics, Faculty of Science and Letters, Osmaniye Korkut Ata University, Osmaniye, Türkiye

*Corresponding Author

‡seymatuluçe@gmail.com (Seyma Tuluçe Demiray); ubayrakci42@gmail.com (Ugur Bayrakci)

Abstract

The basic principle of this study is to obtain various solutions to the (1+1) dimensional Mikhailov-Novikov-Wang integrable equation (MNWIE). For this purpose, the generalized exponential rational function method (GERFM) is applied to this equation. Thus, several trigonometric functions, hyperbolic functions, and dark soliton solutions to the studied equation are acquired. In this way, some new solutions to the equation that have not been presented before have been obtained. In addition, 2D and 3D graphics of the acquired solutions are drawn for specific values. The obtained results and the graphic drawings of the results have been provided by using Wolfram Mathematica 12.

Keywords: Generalized exponential rational function method; (1+1)-dimensional Mikhailov-Novikov-Wang integrable equation; trigonometric function solution; hyperbolic function solution; dark soliton solution

AMS 2020 Classification: 35C07; 35A25; 35C08

1 Introduction

In this study, GERFM has been used, the solution methods of nonlinear evolution equations (NLEEs), and this method has been applied to the (1+1)-dimensional MNWIE, which is a variant of NLEEs. NLEEs have very important applications in areas such as mathematical physics, optical fibers, mathematical chemistry, hydrodynamics, fluid dynamics, geochemistry, control theory, meteorology, optics, mechanics, chemical kinematics, biophysics, biogenetics, and so on. A number of methods have been developed by various researchers in order to obtain solutions for NLEEs, which have such important areas of use in the scientific world:

Modified direct algebraic, modified Kudryashov and trigonometric-quantum B-spline methods [1], improved Bernoulli sub-equation function method [2], modified extended tanh-function

method [3], new extended generalized Kudryashov and generalized new Kudryashov methods [4], new function method [5], $\exp(-\phi(\zeta))$ method [6], double $(G'/G, 1/G)$ -expansion method [7], modified extended tanh-expansion based method [8], modified simple equation method [9], Jacobi elliptic function expansion method [10], modified $(1/G')$ -expansion method [11].

(1+1)-dimensional MNWIE is given as [12]:

$$u_{tt} - u_{xxx}t - 8u_x u_{xt} - 4u_{xx}u_t + 2u_x u_{xxx} + 4u_{xx}u_{xx} + 24u_x^2 u_{xx} = 0. \quad (1)$$

Eq. (1) was derived by using the perturbative symmetry approach to the classification of integrable equations. Also, this equation belongs to a hierarchy where the Boussinesq equation is a member of this class. Hence, studying this equation can provide a good understanding of various nonlinear scientific phenomena in physics [12, 13].

(1+1)-dimensional MNWIE has been studied by some researchers recently. Ray and Singh got the kink-type multisoliton solutions of the equation with the help of simplified Hirota's method [14]. Raza et al. obtained new soliton solutions of the equation using the $\exp(-\phi(\zeta))$ -expansion method, singular manifold method, and generalized projective Riccati equations method [15]. Akbulut et al. found exact solutions of the equation generalized Kudryashov method, exponential rational function method, and modified extended tanh-function method [16]. Bekir et al. obtained new exact soliton solutions of the equation using (G'/G) -expansion method [17]. This study, which was prepared to specify the solutions of the (1+1)-dimensional MNWIE using GERFM [18–23] was designed as follows: In Section 2, GERFM's basic principles are presented. In Section 3, some solutions of (1+1)-dimensional MNWIE have been obtained by applying GERFM. In Section 4, results and discussion are provided and finally, in Section 5, the concluding remarks are given.

2 Brief description of the GERFM

This section introduces an algorithm of the simplest version of the GERFM method, which is used for finding integrable solutions, whose essential steps are given as follows:

Step1: We consider NLPDE given below:

$$P(u, u_x, u_t, u_{xx}, \dots) = 0. \quad (2)$$

We first apply the wave transform given below to Eq. (2);

$$u(x, t) = u(\eta), \eta = x - ct, \quad (3)$$

where c values that are not taken into account will be calculated later. Eq. (2) is transformed into an ordinary differential equation by using Eq. (3):

$$R(u, u', u'', \dots) = 0. \quad (4)$$

Step2: Assume that we think that the solutions of Eq. (4) as:

$$u(\eta) = a_0 + \sum_{i=1}^M a_i \Phi(\eta)^i + \sum_{i=1}^M \frac{b_i}{\Phi(\eta)^i}, \quad (5)$$

where

$$\Phi(\eta) = \frac{p_1 e^{q_1 \eta} + p_2 e^{q_2 \eta}}{p_3 e^{q_3 \eta} + p_4 e^{q_4 \eta}}. \quad (6)$$

Here the value of M is determined through the homogeneous balance principle. $p_1, p_2, p_3, p_4, q_1, q_2, q_3, q_4$ are real or complex constants, $a_0, a_1, a_2, \dots, a_M, b_1, b_2, \dots, b_M$ are scalars and will be determined.

Step3: If Eq. (5) is taken into account in Eq. (4), $P(e^{q_1 \eta}, e^{q_2 \eta}, e^{q_3 \eta}, e^{q_4 \eta}) = 0$ equation system is obtained. A system of equations is obtained by equating all coefficients of P to zero.

Step4: If we solve the obtained system of equations and the found values consider in Eq. (5), the solutions of the discussed NLPDE are obtained.

3 Application of GERFM

To get the exact solutions of Eq. (1) we consider the following transformation:

$$u(x, t) = u(\eta), \eta = x - ct. \quad (7)$$

Replacing Eq. (7) into Eq. (1) and the resulting equation is integrated assuming the integration constant is zero. So the following equation is obtained,

$$c^2 u' + cu''' + 6c(u')^2 + 2u'''u' + (u'')^2 + 8(u')^3 = 0. \quad (8)$$

$u' = v$ transform is written in Eq. (8). Then take the integral and by considering the integration constant as zero, we obtain

$$c^2 v + cv'' + 6cv^2 + 2vv'' + (v')^2 + 8v^3 = 0. \quad (9)$$

By using the balance principle in Eq. (9), we obtain

$$M = 2. \quad (10)$$

If $M = 2$ is taken into account in Eq. (5), the following equality is achieved:

$$u(\eta) = a_0 + a_1 \Phi(\eta) + a_2 \Phi^2(\eta) + \frac{b_1}{\Phi(\eta)} + \frac{b_2}{\Phi^2(\eta)}. \quad (11)$$

So the obtained different states of the considered equation via GERFM are as follows:

Family one: For $p = [-2 - i, 2 - i, -1, 1]$ and $q = [i, -i, i, -i]$ values, Eq. (6) is converted into,

$$\Phi(\eta) = \frac{\cos(\eta) + 2\sin(\eta)}{\sin(\eta)}. \quad (12)$$

$$a_0 = -10, a_1 = 0, a_2 = 0, b_1 = 40, b_2 = -50, c = 4. \quad (13)$$

Embedding Eq. (13) in Eqs. (11) and (12), The trigonometric function solution of Eq. (1) is acquired

as,

$$u_1(x, t) = \frac{10\sin [4t - x]}{\cos [4t - x] - 2\sin [4t - x]}. \tag{14}$$

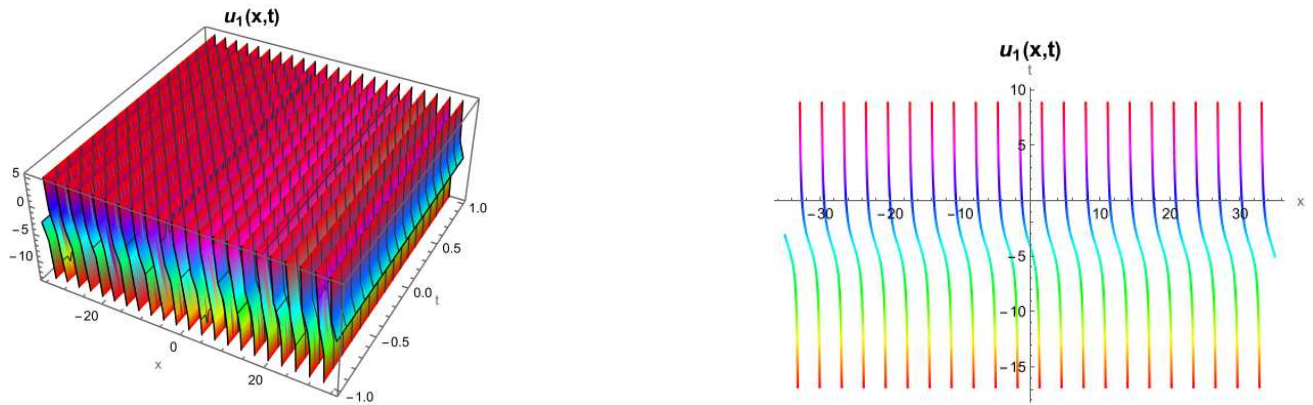


Figure 1. 3D plot of solution (14) for $-35 \leq x \leq 35, -1 \leq t \leq 1$ ranges and 2D plot of solution for $t = 0.5$ with this range.

Family two: For $p = [i, -i, 1, 1]$ and $q = [i, -i, i, -i]$ values, Eq. (6) is converted into,

$$\Phi(\eta) = \frac{-\sin(\eta)}{\cos(\eta)}. \tag{15}$$

$$a_0 = -4, a_1 = 0, a_2 = -2, b_1 = 0, b_2 = -2, c = 16. \tag{16}$$

Embedding Eq. (16) in Eqs. (11) and (15), The trigonometric function solution of Eq. (1) is acquired as,

$$u_2(x, t) = 4\cot [2x - 32t]. \tag{17}$$

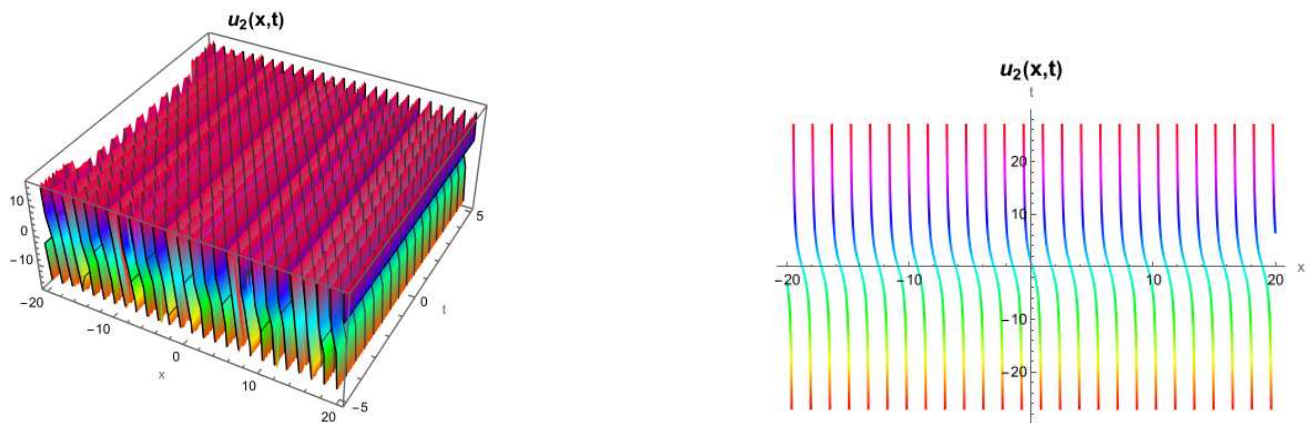


Figure 2. 3D plot of solution (17) for $-20 \leq x \leq 20, -5 \leq t \leq 5$ ranges and 2D plot of solution for $t = 3$ with this range.

Family three: For $p = [1, 1, -1, 1]$ and $q = [1, -1, 1, -1]$ values, Eq. (6) converted into,

$$\Phi(\eta) = \frac{-\cosh(\eta)}{\sinh(\eta)}. \tag{18}$$

Case-1:

$$a_0 = 4, a_1 = 0, a_2 = -2, b_1 = 0, b_2 = -2, c = -16. \tag{19}$$

Embedding Eq. (19) in Eqs. (11) and (18), The dark soliton solution of Eq. (1) is acquired as,

$$u_3(x, t) = 4\coth [2x + 32t]. \tag{20}$$

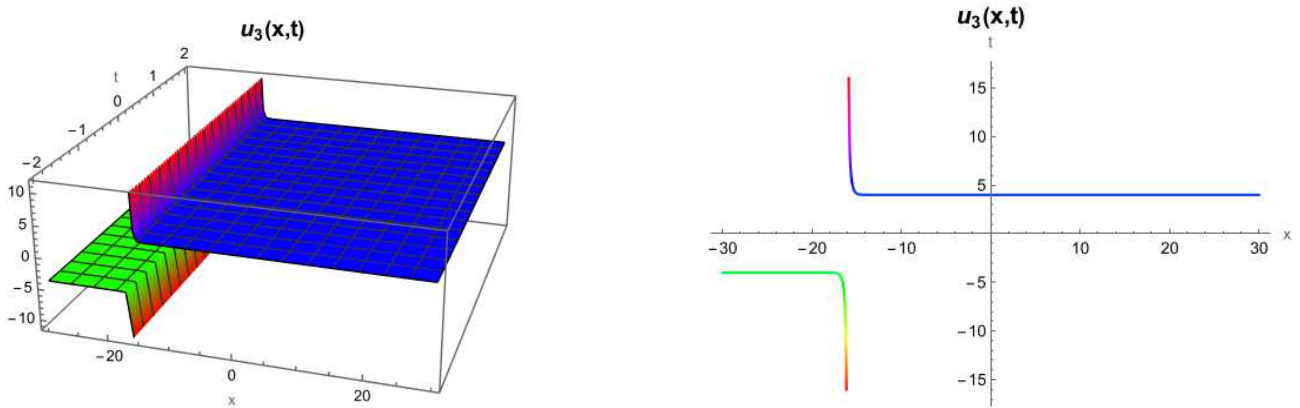


Figure 3. 3D plot of solution (20) for $-30 \leq x \leq 30, -2 \leq t \leq 2$ ranges and 2D plot of solution for $t = 1$ with this range.

Case-2:

$$a_0 = 2, a_1 = 0, a_2 = 0, b_1 = 0, b_2 = -2, c = -4. \tag{21}$$

Embedding Eq. (21) in Eqs. (11) and (18), The dark soliton solution of Eq. (1) is acquired as,

$$u_4(x, t) = 2\tanh [x + 4t]. \tag{22}$$

Family four: For $p = [-2, -3, 1, 1]$ and $q = [1, 0, 1, 0]$ values, Eq. (6) converted into,

$$\Phi(\eta) = \frac{-3 - 2e^\eta}{1 + e^\eta}, \tag{23}$$

$$a_0 = -12, a_1 = 0, a_2 = 0, b_1 = -60, b_2 = -72, c = -1. \tag{24}$$

Embedding Eq. (24) in Eqs. (11) and (23), The soliton solution of Eq. (1) is acquired as,

$$u_5(x, t) = -\frac{6}{3 + 2e^{(x+t)}}. \tag{25}$$

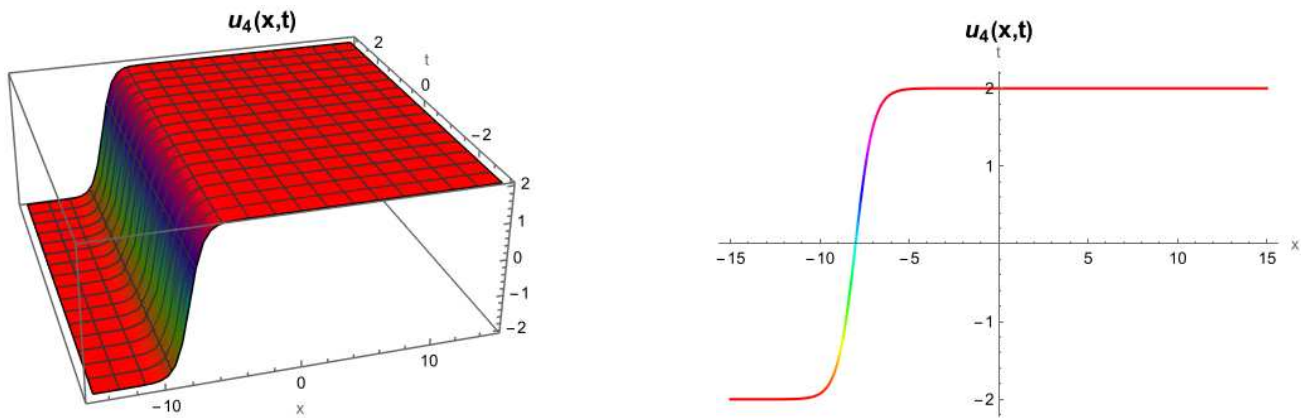


Figure 4. 3D plot of solution (22) for $-15 \leq x \leq 15, -3 \leq t \leq 3$ ranges and 2D plot of solution for $t = 2$ with this range.

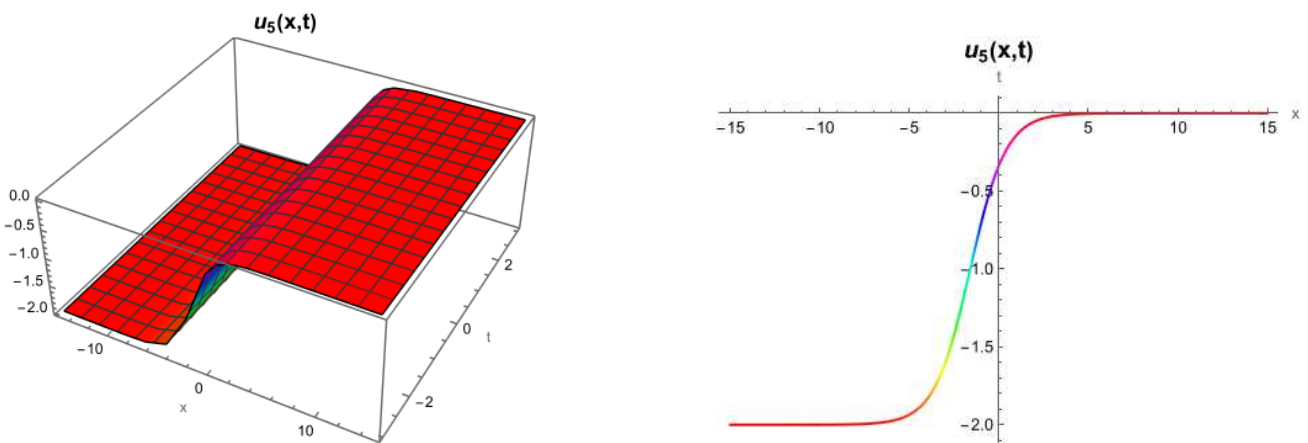


Figure 5. 3D plot of solution (25) for $-15 \leq x \leq 15, -3 \leq t \leq 3$ ranges and 2D plot of solution for $t = 2$ with this range.

Family five: For $p = [-2 - i, -2 + i, 1, 1]$ and $q = [i, -i, i, -i]$ values, Eq. (6) converted into,

$$\Phi(\eta) = \frac{-2\cos(\eta) + \sin(\eta)}{\cos(\eta)}. \tag{26}$$

$$a_0 = -10, a_1 = -8, a_2 = -2, b_1 = 0, b_2 = 0, c = 4. \tag{27}$$

Embedding Eq. (27) in Eqs. (11) and (26), The trigonometric function solution of Eq. (1) is acquired as,

$$u_6(x, t) = 2\tan [4t - x]. \tag{28}$$

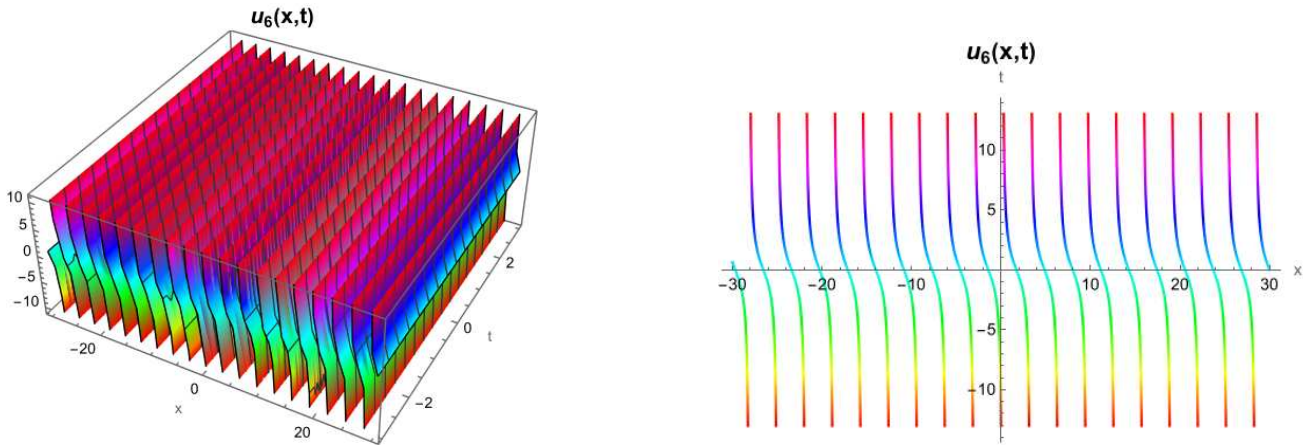


Figure 6. 3D plot of solution (28) for $-30 \leq x \leq 30, -3 \leq t \leq 3$ ranges and 2D plot of solution for $t = 2$ with this range.

Family six: For $p = [-3, -1, 1, 1]$ and $q = [1, -1, 1, -1]$ values, Eq. (6) converted into,

$$\Phi(\eta) = \frac{-2\cosh(\eta) - \sinh(\eta)}{\cosh(\eta)}. \tag{29}$$

$$a_0 = -6, a_1 = 0, a_2 = 0, b_1 = -24, b_2 = -18, c = -4. \tag{30}$$

Embedding Eq. (30) in Eqs. (11) and (29), the hyperbolic function solution of Eq. (1) is acquired as,

$$u_7(x, t) = \frac{3\sinh [x + 4t]}{2\cosh [x + 4t] + \sinh [x + 4t]}. \tag{31}$$

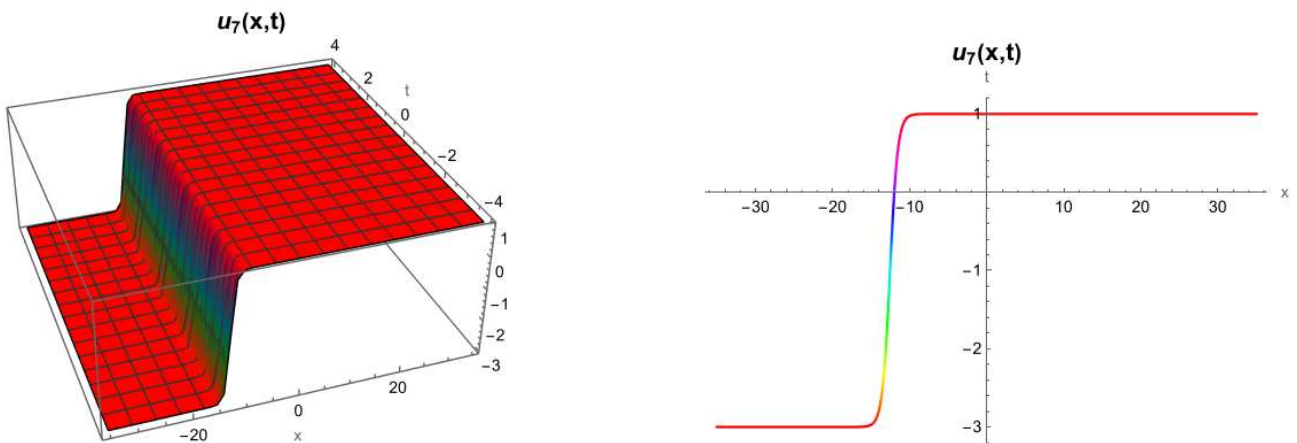


Figure 7. 3D plot of solution (31) for $-35 \leq x \leq 35, -4 \leq t \leq 4$ ranges and 2D plot of solution for $t = 3$ with this range.

4 Results and discussions

We have obtained several trigonometric function, hyperbolic function and dark soliton solutions of the (1+1)-dimensional MNWIE by applying the GERFM. Several methods were previously

applied by some authors to obtain the solutions of the (1+1)-dimensional MNWIE. When we compare the solutions we found with those of previously published papers, our $u_1(x, t)$ solution is similar to solution (31) given by Raza et al. [15]. In addition to our $u_3(x, t)$ solution is similar to (33) solution given by Raza et al. [15], and solutions (23)-(24) given by Akbulut et al. [16]. Our $u_4(x, t)$ solution is similar to (27) and (28) solutions given by Akbulut et al. [16]. Our $u_7(x, t)$ solution is similar to solution (24) given by Raza et al. [15]. According to our research, our other solutions have not been provided before. Thus, the GERFM appears to be an effective method for finding solutions to NLEEs.

5 Conclusion

In this study, (1+1)-dimensional MNWIE was investigated. GERFM, which is the solution method of NLEEs, was applied to this equation. Thus, several trigonometric function, hyperbolic function and dark soliton solutions of the equation were obtained. In order to understand the physical appearance of the found solutions, 2D and 3D graphics were drawn. These obtained results can be further extended and investigated to solve other equations of the Boussinesq type due to their significance in making sense of various nonlinear phenomena. In addition, this considered method can be applied to obtain solutions of equations used for various models. The most important advantage of the method used in this study is that a wide variety of solution families can be created. It is a more general method compared to other methods, as it offers a wide variety of solution families. Despite these advantages, since a different algebraic equation system is created for each solution family, the processing density increases.

Declarations

Consent for publication

Not applicable.

Conflicts of interest

The authors declare that they have no conflict of interests.

Funding

Not applicable.

Author's contributions

S.T.D.: Investigation, Resources, Data Curation, Writing - Review & Editing. U.B.: Conceptualization, Methodology, Writing - Original Draft. All authors discussed the results and contributed to the final manuscript.

Acknowledgements

Not applicable.

References

- [1] Khater, M.M.A. and Alabdali, A.M. Multiple novels and accurate traveling wave and numerical solutions of the (2+ 1) dimensional Fisher-Kolmogorov-Petrovskii-Piskunov equation. *Mathematics*, 9(12), 1-13, (2021). [[CrossRef](#)]
- [2] Dusunceli, F., Celik, E., Askin, M. and Bulut, H. New exact solutions for the doubly dispersive equation using the improved Bernoulli sub-equation function method. *Indian Journal of Physics*, 95(2), 309-314, (2021). [[CrossRef](#)]

- [3] Bakıcıerler, G., Alfaqeih, S. and Mısırlı, E. Analytic solutions of a (2+1)-dimensional nonlinear Heisenberg ferromagnetic spin chain equation. *Physica A: Statistical Mechanics and its Applications*, 582, 126255, (2021). [[CrossRef](#)]
- [4] Malik, S., Kumar, S., Nisar, K.S. and Saleel, C.A. Different analytical approaches for finding novel optical solitons with generalized third-order nonlinear Schrödinger equation. *Results in Physics*, 29, 104755, (2021). [[CrossRef](#)]
- [5] Aktürk, T., Gurefe, Y. and Pandir, Y. An application of the new function method to the Zhiber–Shabat equation. *An International Journal of Optimization and Control: Theories & Applications*, 7(3), 271–274, (2017). [[CrossRef](#)]
- [6] Akbulut, A., Kaplan, M. and Tascan, F. The investigation of exact solutions of nonlinear partial differential equations by using $\exp(-\phi(\xi))$ method. *Optik*, 132, 382–387, (2017). [[CrossRef](#)]
- [7] Ünal, M. and Ekici, M. The double $(G'/G, 1/G)$ -expansion method and its applications for some nonlinear partial differential equations. *Journal of the Institute of Science and Technology*, 11(1), 599–608, (2021). [[CrossRef](#)]
- [8] Nuruddeen, R.I., Aboodh, K.S. and Ali, K.K. Analytical investigation of soliton solutions to three quantum Zakharov-Kuznetsov equations. *Communications in Theoretical Physics*, 70(4), 405–412, (2018). [[CrossRef](#)]
- [9] Tahir, M. and Awan, A.U. Optical singular and dark solitons with Biswas–Arshed model by modified simple equation method. *Optik*, 202, 163523, (2020). [[CrossRef](#)]
- [10] Tasbozan, O., Çenesiz, Y. and Kurt, A. New solutions for conformable fractional Boussinesq and combined KdV-mKdV equations using Jacobi elliptic function expansion method. *The European Physical Journal Plus*, 131, 244, (2016). [[CrossRef](#)]
- [11] Yokuş, A., Durur, H. and Duran, S. Simulation and refraction event of complex hyperbolic type solitary wave in plasma and optical fiber for the perturbed Chen-Lee-Liu equation. *Optical and Quantum Electronics*, 53, 402, (2021). [[CrossRef](#)]
- [12] Mikhailov, A.V., Novikov, V.S. and Wang, J.P. On classification of integrable nonevolutionary equations. *Studies in Applied Mathematics*, 118(4), 419–457, (2007). [[CrossRef](#)]
- [13] Mikhailov, A.V. and Novikov, V.S. Perturbative symmetry approach. *Journal of Physics A: Mathematical and General*, 35(22), 4775, (2002). [[CrossRef](#)]
- [14] Ray, S.S. and Singh, S. New various multisoliton kink-type solutions of the (1+1)-dimensional Mikhailov–Novikov–Wang equation. *Mathematical Methods in the Applied Sciences*, 44(18), 14690–14702, (2021). [[CrossRef](#)]
- [15] Raza, N., Seadawy, A.R., Arshed S. and Rafiq, M.H. A variety of soliton solutions for the Mikhailov-Novikov-Wang dynamical equation via three analytical methods. *Journal of Geometry and Physics*, 176, 104515, (2022). [[CrossRef](#)]
- [16] Akbulut, A., Kaplan, M. and Kaabar, M.K.A. New exact solutions of the Mikhailov-Novikov-Wang equation via three novel techniques. *Journal of Ocean Engineering and Science*, 8(1), 103–110, (2021). [[CrossRef](#)]
- [17] Bekir, A., Shehata, M.S.M. and Zahran, E.H.M. Comparison between the new exact and numerical solutions of the Mikhailov–Novikov–Wang equation. *Numerical Methods for Partial Differential Equations*, (2021). [[CrossRef](#)]
- [18] Srivastava, H.M., Günerhan, H. and Ghanbari, B. Exact traveling wave solutions for resonance nonlinear Schrödinger equation with intermodal dispersions and the Kerr law nonlinearity. *Mathematical Methods in the Applied Sciences*, 42(18), 7210–7221, (2019). [[CrossRef](#)]

- [19] Ghanbari, B., Osman, M.S. and Baleanu, D. Generalized exponential rational function method for extended Zakharov Kuzetsov equation with conformable derivative. *Modern Physics Letters A*, 34(20), 1950155, (2019). [[CrossRef](#)]
- [20] Ismael, H.F., Bulut, H. and Baskonus, H.M. W-shaped surfaces to the nematic liquid crystals with three nonlinearity laws. *Soft Computing*, 25, 4513-4524, (2021). [[CrossRef](#)]
- [21] Sağlam Özkan, Y. The generalized exponential rational function and Elzaki–Adomian decomposition method for the Heisenberg ferromagnetic spin chain equation. *Modern Physics Letters B*, 35(12), 2150200, (2021). [[CrossRef](#)]
- [22] Duran, S. Breaking theory of solitary waves for the Riemann wave equation in fluid dynamics. *International Journal of Modern Physics B*, 35(09), 2150130, (2021). [[CrossRef](#)]
- [23] Duran, S. An investigation of the physical dynamics of a traveling wave solution called a bright soliton. *Physica Scripta*, 96(12), 125251, (2021). [[CrossRef](#)]

Mathematical Modelling and Numerical Simulation with Applications (MMNSA)
(<https://dergipark.org.tr/en/pub/mmnsa>)



Copyright: © 2023 by the authors. This work is licensed under a Creative Commons Attribution 4.0 (CC BY) International License. The authors retain ownership of the copyright for their article, but they allow anyone to download, reuse, reprint, modify, distribute, and/or copy articles in MMNSA, so long as the original authors and source are credited. To see the complete license contents, please visit (<http://creativecommons.org/licenses/by/4.0/>).

How to cite this article: Tuluce Demiray, S. & Bayrakci, U. (2023). A study on the solutions of (1+1)-dimensional Mikhailov-Novikov-Wang equation. *Mathematical Modelling and Numerical Simulation with Applications*, 3(2), 101-110. <https://doi.org/10.53391/mmnsa.1317989>



RESEARCH PAPER

Analysis of a model to control the co-dynamics of Chlamydia and Gonorrhea using Caputo fractional derivative

Udoka Benedict Odionyenma ^{1,*}, Nometa Ikenna ^{2,†} and Bolarinwa Bolaji ^{3,4,‡}

¹Department of Mathematics, African University of Science and Technology, Abuja F.C.T, Nigeria,

²Department of Mathematics, University of Hawaii Manoa, Hawaii 96822, U.S.A., ³Department of

Mathematical Sciences, Prince Abubakar Audu (Formerly Kogi State) University, Anyigba, Nigeria,

⁴Laboratory of Mathematical Epidemiology and Applied Sciences (LOMEAS), Prince Abubakar Audu (Formerly Kogi State) University, Anyigba, Nigeria

*Corresponding Author

[†]oudoka@aust.edu.ng (Udoka Benedict Odionyenma); nometaikenna@gmail.com (Nometa Ikenna); bolarinwa.s.bolaji@gmail.com (Bolarinwa Bolaji)

Abstract

This paper investigates a fractional derivative model of Chlamydia-Gonorrhea co-infection using Caputo derivative definition. The positivity boundedness of the model is established using Laplace transform. Additionally, we investigated the existence and uniqueness of the model using methods established by some fixed point theorems. We concluded that the model is Ulam-Hyers-Rassias stable. Furthermore, we obtained plots of the model at different fractional derivative orders, which show the significant role played by the fractional order on various classes of the model as it varies. We observe distinct results for each class in different orders, highlighting the importance of considering the fractional order in modeling Chlamydia-Gonorrhea co-infection. Moreover, the fractional model presented in this paper can be used to study the dynamics of Chlamydia-Gonorrhea co-infection in a more accurate and realistic way compared to traditional integer-order models.

Keywords: Chlamydia; Gonorrhea; fractional derivative; co-infection; control

AMS 2020 Classification: 26A33; 34A08; 34D20; 34D23; 92B05

1 Introduction

Sexually Transmitted Diseases (STD), such as chlamydia, are a major public health concern in the United States. Despite being asymptomatic in most cases, chlamydia is one of the most frequently reported bacterial infections [1]. The number of reported cases of chlamydia remains high, with up

to four million new infections estimated to have occurred in 2018, and youth between the ages of 15 and 24 accounting for two-thirds of these cases. In fact, it is believed that one in twenty sexually active young women between the ages of 14 and 24 have chlamydia [1]. Untreated chlamydia infections can lead to serious health consequences, such as Pelvic Inflammatory Disease (PID), which can cause complications such as blocked Fallopian tubes, ectopic pregnancy, and longer pelvic and abdominal pain. Although the number of reported cases of chlamydia may have decreased in 2020 due to COVID-19 restrictions, such as clinic closures and reduced testing, it is important to continue researching this disease to gain further insights on how to reduce its burden on public health.

According to reports, gonorrhoea is the second most common sexually transmitted disease in the United States, with young people being the majority of those infected [2]. This STD causes infections in the genitals, throat, and rectum, similar to chlamydia, and is particularly prevalent among people aged 15-24 years. Gonorrhoea commonly affects the cervix, uterus, and Fallopian tubes in women, and the urethra in both genders. It can also spread from mother to child during pregnancy. The Centers for Disease Control and Prevention (CDC) recommend a single intramuscular dose of 500mg of ceftriaxone for treatment of gonorrhoea, but there have been cases of resistance to some antibiotics. This highlights the importance of continued research and vigilance in addressing the growing concern of antibiotic-resistant gonorrhoea.

Co-infection of both gonorrhoea and chlamydia trachomatis is not uncommon, and understanding the implications of this co-infection is necessary to manage such situations effectively. According to some reports [3], individuals with this co-infection are more likely to develop pelvic inflammatory disease (PID), which is a severe complication that can result from untreated STDs. Therefore, it is important to study the dynamics of this co-infection and gain insights into how to manage it. Furthermore, with increased drug resistance from some of these STDs, vaccination of individuals may be a more effective solution. This will be investigated in this work to enable an informed decision on how to tackle these diseases in the future.

The use of mathematical models in infectious disease research has proven to be valuable, but it is crucial to use models that capture the memory effect. Fractional calculus has shown promise in developing such models, and more research is needed to improve the accuracy of disease predictions and control measures, hence this is our motivation in carrying out this research. Some integer models have also been developed to understand the dynamics of specific infections, such as Chlamydia trachomatis, Gonorrhoea, or their co-infections and other diseases can be seen in [4–17]. The work by Odionyenma et al. [4] presented an SVEIRT epidemiological model, which centered on investigating the role of a vaccination class in the general dynamics of the model. Optimal control analysis of the model was also carried out, showing that the most cost-effective strategy in dealing with the transmission dynamics of the model. A study in [17] looked at a co-infection model of Chlamydia and Gonorrhoea, with target interest on the effect of treatment for each disease on the co-infection on the population. It showed that implementing female Chlamydia treatment and male Chlamydia treatment resulted in a significant decrease in the total number of females and males co-infected with Chlamydia and Gonorrhoea.

The use of non-integer order derivatives in modeling contagious illnesses has gained increasing attention from scholars and analysts. Traditional epidemiological models can only be designated via a fixed order, which is not applicable to fractional order derivatives. One study by Omame et al. [18] investigated a new mathematical model for co-infection of COVID-19 and Hepatitis B virus using the Atangana-Baleanu fractional derivative. The authors solved the model analytically using the Laplace-Adomian decomposition method and discussed the stability of the iterative scheme to approximate the solution. The numerical analysis showed that prevention and control measures for either COVID-19 or Hepatitis B could significantly reduce the burden of co-infection.

The dynamics of tuberculosis model using the Caputo-Fabrizio fractional derivative was studied by Ullah in [19]. The study utilized data from reported cases of TB in the national TB program Khyber Pakhtunkhwa, Pakistan from 2002 to 2017. The model was used to derive the reproduction number R_0 , and other relevant variables. The Adams-Bashforth method was used to compute the solution of the model iteratively. The study concluded that the fractional model provided helpful information on TB and a better way to view the spread of the disease. There have been so many studies on the use of fractional derivatives in modeling infectious diseases as can be seen in [20–36].

Models that have utilized fractional derivatives in non-disease modeling can be seen in [37–40]. A fractional-order derivative chaotic system described by Caputo derivative was studied in the work by [37]. The effect of the fractional-order derivative was carried out, the stability analysis was utilized to determine the chaotic region where the order of the Caputo derivative presented in the system, and the nature of the chaos was established using the Lyapunov's exponents in the fractional context. Also, the work by [38] analyzes a model describing the production of mobile phone worms. This study explores the behaviors of the forced Korteweg–De Vries (KdV) equation, which describes flowing over a hole. By utilizing the q-homotopy analysis transform technique (q-HATT), the study finds solutions using a combination of the q-homotopy analysis scheme and the Laplace transform. The study employs fractional operators to generalize models associated with various characteristics. It establishes the existence, uniqueness, and convergence of the models using a fixed-point theorem. The results demonstrate the reliability and systematic nature of the solution procedure for investigating both integer and fractional-order nonlinear models.

The paper is organized as follows: Section 1 presents the introduction and model formulation. Section 2 covers the basic theory of Caputo fractional derivative, including the existence and uniqueness of solutions, the basic reproduction number, stability analysis of fractional order systems, and global stability of the disease-free equilibrium.

Sections 3 and 4 provide details on the numerical simulations and their interpretations, with plots displayed. Section 5 concludes the work with some recommendations for future research. The model considered in this paper is a modified version of an existing integer order model considered in [17]. We have modified it and also applied fractional calculus to analyze the model. This has not been considered before.

Model description

At the time t , the population is represented by $N_H(t)$ and is divided into seven compartments. These compartments are susceptible individuals who are unvaccinated (S_H), those who are vaccinated (V_{CL}), those infected with Chlamydia (I_{CL}), those treated for Chlamydia (T_{CL}), those infected with Gonorrhoea (I_G), those treated for Gonorrhoea (T_G), and those infected with both Chlamydia and Gonorrhoea (I_{GCL}). The unvaccinated susceptible group, S_H , is increased by the recruitment rate Λ_H . Individuals within this group can contract Chlamydia and/or Gonorrhoea from infected individuals at rates β_{CL} and β_G , respectively, with acquisition rates of λ_{CL} and λ_G . Furthermore, the parameter η_L and η_G account for the increased infectiousness of individuals who are infected with both Chlamydia and Gonorrhoea, where other parameters are defined in Table 1. Additionally, individuals who receive treatment move to the T_{CL} or T_G compartments, depending on their infection status. Vaccinated individuals move from the V_{CL} compartment to the S_H compartment at a rate proportional to their vaccine efficacy. The total population at time t can be expressed as $N_H = S_H + V_{CL} + I_{CL} + T_{CL} + I_G + T_G + I_{GCL}$.

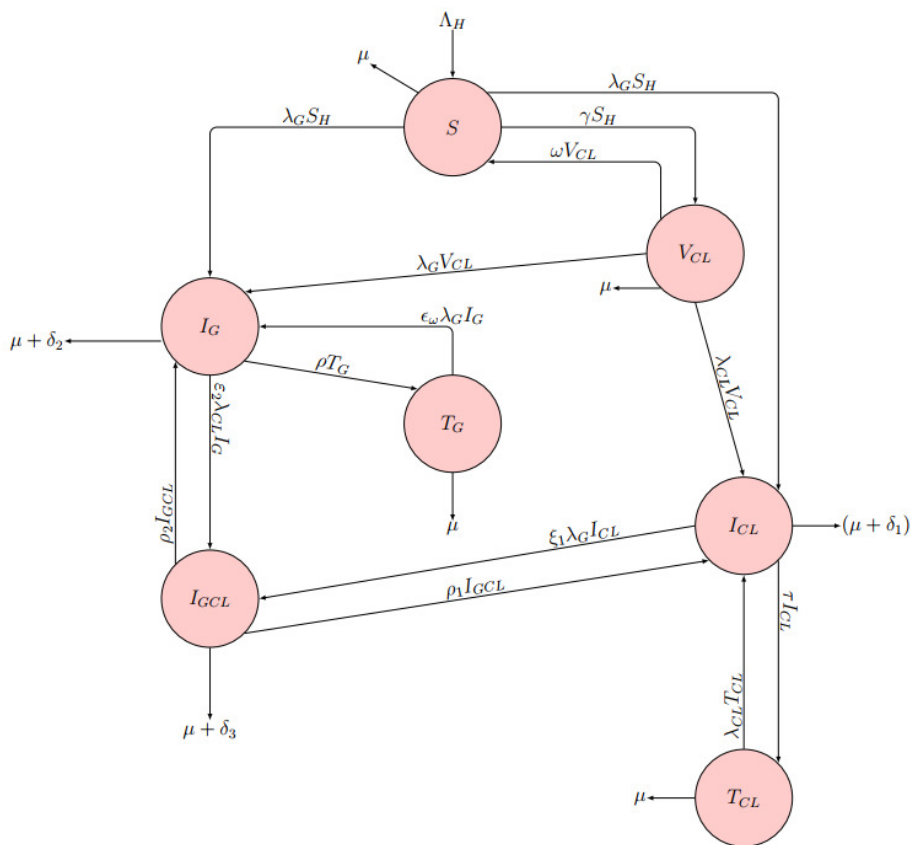


Figure 1. Schematic diagram of model (1).

Table 1. Parameters and description

Parameter	Description
ϵ_w, ϵ_L	Reinfection rates for Chlamydia and Gonorrhoea
μ	Natural death rate
$\rho_1 (\rho_2)$	Rate at which dually infected gets treated of Gonorrhoea (Chlamydia)
ρ	Treatment rate for gonorrhoea
ω	Waning of vaccine rate
γ	Vaccination rate
τ	Treatment rate for chlamydia
δ_1	Disease-induced death rate for chlamydia infected individuals
δ_2	Disease-induced death rate for gonorrhoea infected individuals
δ_3	Disease-induced death rate for co-infected individuals
Λ_H	Recruitment rate
β_{CL}, β_G	Contact rate for Chlamydia and Gonorrhoea infected individuals
ξ_1, ξ_2	Rate at which singly infected individuals becomes dually infected with Chlamydia and Gonorrhoea
η_L, η_g	Modification parameter accounting for increased infectiousness of individuals dually infected with chlamydia and gonorrhoea

The Chlamydia-Gonorrhoea co-infection model is given by the following system of fractional order differential equations based on the aforementioned formulations and assumptions:

$$\begin{aligned}
 D_t^\zeta S_H(t) &= \Lambda_H - (\lambda_G + \lambda_{CL})S_H + \omega V_{CL} - (\mu + \gamma)S_H, \\
 D_t^\zeta V_{CL}(t) &= \gamma S_H - (\mu + \omega)V_{CL} - V_{CL}(\lambda_G + \lambda_{CL}), \\
 D_t^\zeta I_{CL}(t) &= \lambda_{CL}S_H + \epsilon_L \lambda_{CL}T_{CL} - (\mu + \tau + \delta_1)I_{CL} - \xi_1 \lambda_G I_{CL} + \rho_1 I_{GCL} + V_{CL}\lambda_{CL}, \\
 D_t^\zeta T_{CL}(t) &= \tau I_{CL} - (\mu + \epsilon_L \lambda_{CL})T_{CL}, \\
 D_t^\zeta I_G(t) &= \lambda_G S_H - (\mu + \delta_2 + \rho)I_G + \rho_2 I_{GCL} + \epsilon_W \lambda_G T_G - \xi_2 \lambda_{CL} I_G + V_{CL}\lambda_G, \\
 D_t^\zeta T_G(t) &= \rho I_G - (\mu + \epsilon_W \lambda_G)T_G, \\
 D_t^\zeta I_{GCL}(t) &= \xi_1 \lambda_G I_{CL} + \xi_2 \lambda_{CL} I_G - (\mu + \delta_3 + \rho_1 + \rho_2)I_{GCL},
 \end{aligned}
 \tag{1}$$

$$\begin{aligned}
 \lambda_{CL} &= \frac{\beta_{CL}(I_{CL} + \eta_L I_{GCL})}{N_H}, \\
 \lambda_G &= \frac{\beta_G(I_G + \eta_g I_{GCL})}{N_H},
 \end{aligned}
 \tag{2}$$

with the corresponding initial conditions

$$S_H(0) \geq 0, V_{CL}(0) \geq 0, I_{CL}(0) \geq 0, T_{CL}(0) \geq 0, T_G(0) \geq 0, I_G(0) \geq 0, I_{GCL}(0) \geq 0.
 \tag{3}$$

2 Preliminaries and basic properties of the model

Caputo fractional derivative has been widely used in modeling disease dynamics due to its ability to capture the memory effect and long-range dependence in the system. This section provides some basic definitions related to fractional calculus, with a focus on Caputo fractional derivative. Specifically, we introduce the Riemann-Liouville fractional integral of order $\zeta > 0$, which can be obtained by replacing n with ζ in the integral formula. We also discuss the Ulam-Hyers-Rassias stability of fractional order systems and derive the basic reproduction number for the co-infection model. Furthermore, we establish the existence and uniqueness of the model’s solution, which is essential for numerical simulation and analysis.

Definition 1 [41] *The Caputo fractional derivative of order $\zeta > 0$ of a function $f(t)$ of order $\zeta \in \mathbb{R}^+$ is defined by*

$$D_t^\zeta f(t) = J_t^{n-\zeta} D^n f(t) = \frac{1}{\Gamma(n-\zeta)} \int_0^t (t-\tau)^{n-\zeta-1} f^{(n)}(\tau) d\tau,$$

where n is an integer whose definition is $n - 1 < \zeta \leq n$. Actually, where $0 < \zeta \leq 1$, from the derivative above, where $\zeta > 0$ gives

$$D_t^\zeta f(t) = \frac{1}{\Gamma(1-\zeta)} \int_0^t (t-\tau)^{-\zeta} f'(\tau) d\tau.
 \tag{4}$$

Definition 2 [34] *The fractional integral of order $\zeta > 0$ of a function $f \in C^1(0, T)$ is given by*

$$J_t^\zeta f(t) = \frac{1}{\Gamma(\zeta)} \int_0^t (t - \tau)^{\zeta-1} f(\tau) d\tau, \quad t > 0,$$

if the integral exists in \mathbb{R}^+ . For convenience, suppose $f(t) = K$, where K is a constant then;

$$J_t^\zeta(K) = \frac{1}{\Gamma(\zeta)} \int_0^t (t - \tau)^{\zeta-1} (K) d\tau = K \frac{t^\zeta}{\Gamma(\zeta + 1)}.$$

Definition 3 [41] *The Laplace transform of Caputo fractional derivative is given by*

$$\mathcal{L} \left\{ D_t^\zeta f(t) \right\} = s^\zeta \tilde{f}(s) - s^{\zeta-1} f(0), \quad 0 < \zeta \leq 1, \tag{5}$$

where \mathcal{L} is the operator of the Laplace transform..

Lemma 1 [42] *Let $\zeta \in \mathbb{R}^+$, $\phi_1(t)$ and $\phi_2(t)$ represent positive functions and $\phi_3(t)$ represent an increasing and positive function for $0 \leq t \leq T$, $T > 0$, $\phi_3(t) \leq M$, where M is a constant. Suppose*

$$\phi_1 \leq \phi_2 + \phi_3(t) \int_0^T (t - \tau)^{\zeta-1} \phi_1(t) d\tau,$$

then

$$\phi_1 \leq \phi_2 E_\zeta \left(\phi_3(t) \frac{\pi}{\Gamma(1 - \zeta) \sin(\pi\zeta)} T^\zeta \right).$$

Theorem 1 *Suppose $S_H(t)$, $V_{CL}(t)$, $I_{CL}(t)$, $T_{CL}(t)$, $T_G(t)$, $I_G(t)$, $I_{GCL}(t)$ are any solution of the system (1)- (3), then the set*

$$\begin{aligned} \Delta = & \left\{ (S_H(t), V_{CL}(t), I_{CL}(t), T_{CL}(t), T_G(t), I_G(t), I_{GCL}(t)) \in \mathbb{R}_+^7 : S_H \right. \\ & \left. + V_{CL} + I_{CL} + T_{CL} + T_G + I_G + I_{GCL} \leq \frac{\Lambda_H}{\mu} \right\}, \end{aligned} \tag{6}$$

is positively invariant.

Proof. When all of the equations in (1) are added, we have

$$\begin{aligned} D_t^\zeta N_H(t) &= D_t^\zeta S_H(t) + D_t^\zeta V_{CL}(t) + D_t^\zeta I_{CL}(t) + D_t^\zeta T_{CL}(t) + D_t^\zeta T_G(t) + D_t^\zeta I_G + D_t^\zeta I_{GCL} \\ &= \Lambda_H - \mu (S_H + V_{CL} + I_{CL} + T_{CL} + T_G + I_G + I_{GCL}) \\ &\quad - (\gamma S_H + \omega V_{CL} + \delta_1 I_{CL} + \delta_2 I_G + \delta_3 I_{GCL}) \\ &\leq \Lambda_H - \mu N_H. \end{aligned}$$

If we apply the Laplace Transform to the above equation, we have

$$s^\zeta \tilde{N}_H(s) - s^{\zeta-1} N_H(0) \leq \frac{\Lambda_H}{s} - \mu \tilde{N}_H(s),$$

from which

$$\tilde{N}_H(s) \leq \frac{\Lambda_H}{s(s^\zeta + \mu)} + N_H(0) \frac{s^{\zeta-1}}{s^\zeta + \mu}.$$

The expression above gives the following result after partial fraction decomposition

$$\tilde{N}_H(s) \leq \frac{\Lambda_H}{\mu} \left(\frac{1}{s} \right) - \left(\frac{\Lambda_H}{\mu} - N_H(0) \right) \sum_{k=0}^{\infty} \frac{(-\mu)^k}{s^{\zeta k+1}}.$$

The inverse Laplace transform gives

$$N_H(t) \leq \frac{\Lambda_H}{\mu} - \left(\frac{\Lambda_H}{\mu} - N_H(0) \right) E_\zeta(-\mu t^\zeta),$$

as $t \rightarrow \infty$, we have

$$N_H \leq \frac{\Lambda_H}{\mu}, \tag{7}$$

giving the condition for Eqs. (1)-(3) to be bounded and mathematically posed within the region.

Positivity of solution of the model

Using the approach by [34], and assuming that I_{CL} class is not positively invariant. Let $t_1 = \min\{t : S_H(t), V_{CL}(t), I_{CL}(t), T_{CL}(t), I_G(t), T_G(t), I_{GCL}\}$. Suppose $I_{CL}(t_1) = 0$, it gives that $S_H(t) > 0$, $V_{CL}(t) > 0$, $T_{CL}(t) > 0$, $I_G(t) > 0$, $I_{GCL}(t) > 0$ for all $[0, t_1]$. If the following expression exists,

$$\theta_1 = \min_{0 \leq t \leq t_1} \left\{ \frac{(\lambda_{CL} S_H + \epsilon_L \lambda_{CL} T_{CL} + \rho_1 I_{GCL} + V_{CL} \lambda_{CL})}{I_{CL}} - (\mu + \tau + \delta_1 + \xi_1 \lambda_G) \right\}.$$

It will result in that

$$D_t^\zeta I_{CL}(t) - \theta_1 I_{CL}(t) > 0. \tag{8}$$

With Ω_1 , a continuous function, we can say that the following equation is ascertained

$$D_t^\zeta I_{CL}(t) - \theta_1 I_{CL}(t) = -\Omega_1(t).$$

with Laplace transform applied to the inequality, it gives

$$s^\zeta \tilde{I}_{CL}(s) - s^{\zeta-1} I_{CL}(0) - \theta_1 \tilde{I}_{CL}(s) = -\tilde{\Omega}_1(s),$$

from which

$$\begin{aligned} \tilde{I}_{CL}(s) &= I_{CL}(0) \frac{s^{\zeta-1}}{s^{\zeta} - \theta_1} - \frac{\Omega_1(s)}{s^{\zeta} - \theta_1} = \frac{I_{CL}(0)}{s} \left(1 - \frac{\theta_1}{s^{\zeta}}\right)^{-1} - \frac{\Omega_1(s)}{s^{\zeta}} \left(1 - \frac{\theta_1}{s^{\zeta}}\right)^{-1} \\ &= I_{CL}(0) \sum_{k=0}^{\infty} \frac{\theta_1^k}{s^{\zeta k+1}} - \Omega_1(s) \sum_{k=0}^{\infty} \frac{\theta_1^k}{s^{\zeta k+\zeta}}. \end{aligned}$$

The Mittag-Leffler function and the inverse Laplace transform yield the solution to Eq. (8) satisfying the following expression;

$$I_{CL}(t) > I_{CL}(0) \sum_{k=0}^{\infty} \frac{(\theta_1 t^{\zeta})^k}{\Gamma(\zeta k + 1)} = I_{CL}(0) E_{\zeta}(\theta_1 t^{\zeta}).$$

Then the positivity of I_{CL} is given by

$$I_{CL}(t) > I_{CL}(0) E_{\zeta}(\theta_1 t^{\zeta}) > 0,$$

which contradicts $I_{CL}(t_1) = 0$. Similarly, suppose $T_{CL}(t_1) = 0$ which implies that $S_H(t) > 0$, $I_{CL}(t) > 0$, $V_{CL}(t) > 0$, $I_G(t) > 0$, $T_G(t) > 0$, $I_{GCL}(t) > 0$, $\forall 0 \leq t \leq t_1$. Making the following assumption

$$\theta_2 = \min_{0 \leq t \leq t_1} \left\{ \frac{\tau I_{CL}}{T_{CL}} - (\mu + \epsilon_L \lambda_{CL}) \right\},$$

then

$$D_t^{\zeta} T_{CL}(t) > \theta_2 T_{CL}(t). \tag{9}$$

With Ω_2 , a continuous function, the following equation is ascertained

$$D_t^{\zeta} T_{CL}(t) - \theta_2 T_{CL}(t) = -\Omega_2(t).$$

Applying Laplace transform to the above inequality we get

$$s^{\zeta} \tilde{T}_{CL}(s) - s^{\zeta-1} T_{CL}(0) - \theta_2 \tilde{T}_{CL}(s) = -\tilde{\Omega}_2(s),$$

from which

$$\tilde{T}_{CL}(s) = T_{CL}(0) \frac{s^{\zeta-1}}{s^{\zeta} - \theta_2} - \frac{\Omega_2(s)}{s^{\zeta} - \theta_2} = T_{CL}(0) \sum_{k=0}^{\infty} \frac{\theta_2^k}{s^{\zeta k+1}} - \Omega_2(s) \sum_{k=0}^{\infty} \frac{\theta_2^k}{s^{\zeta k+\zeta}}.$$

The solution of Eq. (9) is provided by utilizing the Mittag-Leffler function and the inverse Laplace transform, satisfying the following expression

$$T_{CL}(t) > T_{CL}(0) \sum_{k=0}^{\infty} \frac{(\theta_2 t^\zeta)^k}{\Gamma(\zeta k + 1)} = T_{CL}(0) E_\zeta (\theta_2 t^\zeta).$$

which gives the positivity of solution of T_{CL} as

$$T_{CL}(t) > T_{CL}(0) E_\zeta (\theta_2 t^\zeta) > 0,$$

which contradicts $T_{CL}(t_1) = 0$. If we follow the same method above, and assume $T_G(t_1) = 0$ which implies that $S_H(t) > 0, V_{CL}(t) > 0, I_{CL}(t) > 0, T_{CL}, I_G(t) > 0, I_{GCL}(t) > 0$, for all $0 \leq t \leq t_1$. Assuming that the following expression exist

$$\theta_3 = \min_{0 \leq t \leq t_1} \left\{ \frac{\rho I_G}{T_G} - (\mu + \epsilon_w \lambda_G) \right\},$$

so that

$$D_t^\zeta T_G(t) > \theta_3 T_G(t). \tag{10}$$

With Ω_3 , a continuous function, we can say that the following equation is ascertained

$$D_t^\zeta T_G(t) - \theta_3 T_G(t) = -\Omega_3(t).$$

With Laplace transform applied to the inequality, it gives;

$$s^\zeta \tilde{T}_G(s) - s^{\zeta-1} T_G(0) - \theta_3 \tilde{T}_G(s) = -\tilde{\Omega}_3(s),$$

which gives the following;

$$\tilde{T}_G(s) = T_G(0) \sum_{k=0}^{\infty} \frac{\theta_3^k}{s^{\zeta k + 1}} - \tilde{\Omega}_3(s) \sum_{k=0}^{\infty} \frac{\theta_3^k}{s^{\zeta k + \zeta}}.$$

The solution of Eq. (10) is provided by utilizing the Mittag-Leffler function and the inverse Laplace transform. satisfying the following expression

$$T_G(t) > T_G(0) \sum_{k=0}^{\infty} \frac{(\theta_3 t^\zeta)^k}{\Gamma(\zeta k + 1)} = I_c(0) E_\zeta (\theta_3 t^\zeta). \tag{11}$$

Hence the positivity of the solution T_G is shown as $T_G(t) > T_G(0) E_\zeta (\theta_3 t^\zeta) > 0$, which contradicts $T_G(t_1) = 0$. Again, we suppose $I_{GCL}(t_1) = 0$ which implies that $S_H(t) > 0, V_{CL}(t) > 0, I_{CL}(t) > 0, T_{CL} > 0, I_G(t) > 0, T_G > 0$ for all $0 \leq t \leq t_1$. Assuming the expression below exists;

$$\theta_4 = \min_{0 \leq t \leq t_1} \left\{ \frac{(\xi_1 \lambda_G I_{CL} + \xi_2 \lambda_{CL} T_G)}{I_{GCL}} - (\mu + \delta_3 + \rho_1 + \rho_2) \right\},$$

such that

$$D_t^\zeta I_{GCL}(t) > \theta_4 I_{GCL}(t). \quad (12)$$

Also, Ω_4 can be gotten, such that the expression below is ascertained

$$D_t^\zeta I_{GCL}(t) - \theta_4 I_{GCL}(t) = -\Omega_4(t).$$

If Laplace transform is applied to the above inequality, we have;

$$s^\zeta \tilde{I}_{GCL}(s) - s^{\zeta-1} I_{GCL}(0) - \theta_4 \tilde{I}_{GCL}(s) = -\tilde{\Omega}_p(s),$$

from which

$$\tilde{I}_{GCL}(s) = I_{GCL}(0) \sum_{k=0}^{\infty} \frac{\theta_4^k}{s^{\zeta k+1}} - \Omega_4(s) \sum_{k=0}^{\infty} \frac{\theta_4^k}{s^{\zeta k+\zeta}}.$$

The following expressions are satisfied by the solution of (12) when the negative term is ignored when using the Mittag-Leffler function and the inverse Laplace transform.

$$I_{GCL}(t) > I_{GCL}(0) \sum_{k=0}^{\infty} \frac{(\theta_4 t^\zeta)^k}{\Gamma(\zeta k + 1)} = I_{GCL}(0) E_\zeta(\theta_4 t^\zeta).$$

and the positivity of solution of I_{GCL} , is shown as;

$$I_{GCL}(t) > I_{GCL}(0) E_\zeta(\theta_4 t^\zeta) > 0,$$

which contradicts $I_{GCL}(t_1) = 0$. Using the same method shows that the positivity of the solutions S_H , V_{CL} , and I_G respectively are given by

$$S_H(t) > S_H(0) E_\zeta(\theta_5 t^\zeta) > 0, \quad V_{CL}(t) > V_{CL}(0) E_\zeta(\theta_6 t^\zeta) > 0,$$

$$I_G(t) > I_G(0) E_\zeta(\theta_7 t^\zeta) > 0.$$

Existence and uniqueness of the solution of the model

In this section, we will demonstrate the existence and uniqueness of the solution to the fractional model (1). To achieve this, we adopt a similar approach to the one used in [32], where the Banach fixed point theorem was used. Additionally, we will apply Schaefer's fixed point theorem to establish the existence of the solution and demonstrate its boundedness. The fractional integral will be applied to the Caputo fractional derivative model (1) of order $\zeta > 0$, along with its respective initial conditions (3). This process will yield Volterra-integral equations of the second

kind, which will serve as the solution to the fractional model. Given that $F, G, H, K, Q, U,$ and V are the right side of the various classes of (1) respectively.

$$\begin{aligned}
 S_H(t) - S_H(0) &= \frac{1}{\Gamma(\zeta)} \int_0^t (t - \tau)^{\zeta-1} F(t, S_H(t)) d\tau, \\
 V_{CL}(t) - V_{CL}(0) &= \frac{1}{\Gamma(\zeta)} \int_0^t (t - \tau)^{\zeta-1} G(t, V_{CL}(t)) d\tau, \\
 I_{CL}(t) - I_{CL}(0) &= \frac{1}{\Gamma(\zeta)} \int_0^t (t - \tau)^{\zeta-1} H(t, I_{CL}(t)) d\tau, \\
 T_{CL}(t) - T_{CL}(0) &= \frac{1}{\Gamma(\zeta)} \int_0^t (t - \tau)^{\zeta-1} K(t, T_{CL}(t)) d\tau, \\
 I_G(t) - I_G(0) &= \frac{1}{\Gamma(\zeta)} \int_0^t (t - \tau)^{\zeta-1} Q(t, I_G(t)) d\tau, \\
 T_G(t) - T_G(0) &= \frac{1}{\Gamma(\zeta)} \int_0^t (t - \tau)^{\zeta-1} U(t, T_G(t)) d\tau, \\
 I_{GCL}(t) - I_{GCL}(0) &= \frac{1}{\Gamma(\zeta)} \int_0^t (t - \tau)^{\zeta-1} V(t, I_{GCL}(t)) d\tau.
 \end{aligned} \tag{13}$$

The functions $(F, G, H, K, Q, U, V) : [0, T] \times \mathbb{D} \rightarrow \mathbb{D}$ are assumed to be continuous such that $(\mathbb{D}, \|\cdot\|)$ is the Banach space and $\mathbb{H}^1([0, T])$ is the Banach space of all the continuous function defined in $[0, T] \rightarrow \mathbb{D}$ shaped with Chebyshev norm.

The continuous functions F, G, H, K, Q, U and V satisfy the Lipschitz condition if

$$\begin{aligned}
 \sup_{0 < t \leq T} \left\| \frac{S_H}{N_H} \right\| &\leq \Theta_1, \quad \sup_{0 < t \leq T} \left\| \frac{V_{CL}}{N_H} \right\| \leq \Theta_2, \quad \sup_{0 < t \leq T} \left\| \frac{I_{CL}}{N_H} \right\| \leq \Theta_3, \quad \sup_{0 < t \leq T} \left\| \frac{T_{CL}}{N_H} \right\| \leq \Theta_4, \\
 \sup_{0 < t \leq T} \left\| \frac{I_G}{N_H} \right\| &\leq \Theta_5, \quad \sup_{0 < t \leq T} \left\| \frac{T_G}{N_H} \right\| \leq \Theta_6, \quad \sup_{0 < t \leq T} \left\| \frac{I_{GCL}}{N_H} \right\| \leq \Theta_7.
 \end{aligned}$$

Thus, firstly we have

$$\begin{aligned}
 \|F(S_{H1}) - F(S_{H2})\| &= \left\| \Lambda_H + \omega V_{CL} - \left(\frac{\beta_{CL}(I_{CL} + \eta_C I_{GCL})}{N_H} + \frac{\beta_G(I_G + \eta_g I_{GCL})}{N_H} + \mu + \gamma \right) S_{H1} \right. \\
 &\quad \left. - \left(\Lambda_H + \omega V_{CL} - \left(\frac{\beta_{CL}(I_{CL} + \eta_C I_{GCL})}{N_H} + \frac{\beta_G(I_G + \eta_g I_{GCL})}{N_H} + \mu + \gamma \right) S_{H2} \right) \right\| \\
 &= \left\| -\frac{\beta_{CL} I_{CL}}{N_H} (S_{H1} - S_{H2}) - \frac{\beta_{CL} \eta_C I_{GCL}}{N_H} (S_{H1} - S_{H2}) - \frac{\beta_G I_G}{N_H} (S_{H1} - S_{H2}) \right. \\
 &\quad \left. - \frac{\beta_G \eta_g I_{GCL}}{N_H} (S_{H1} - S_{H2}) - \gamma (S_{H1} - S_{H2}) - \mu (S_{H1} - S_{H2}) \right\| \\
 &\leq \beta_{CL} \sup_{0 \leq t \leq T} \left\| \frac{I_{CL}}{N_H} \right\| \|S_{H1} - S_{H2}\| + \beta_{CL} \eta_C \sup_{0 \leq t \leq T} \left\| \frac{I_{GCL}}{N_H} \right\| \|S_{H1} - S_{H2}\| \\
 &\quad + \gamma \|S_{H1} - S_{H2}\| + \mu \|S_{H1} - S_{H2}\| \\
 &\leq L_F \|S_{H1} - S_{H2}\|,
 \end{aligned} \tag{14}$$

where

$$L_F = (\beta_{CL}\Theta_3 + \beta_{CL}\eta_g\Theta_7 + \gamma + \mu) > 0.$$

Secondly,

$$\begin{aligned} \|G(V_{CL1}) - G(V_2)\| &= \|\gamma S_H - (\mu + \omega + \lambda_G + \lambda_{CL})V_{CL1} \\ &\quad - (\gamma S_H - (\mu + \omega + \lambda_G + \lambda_{CL})V_{CL2})\| \\ &= \|(\mu + \omega + \lambda_G + \lambda_{CL})(V_{CL1} - V_{CL2})\| \\ &\leq L_G \|V_{CL1} - V_{CL2}\|, \end{aligned}$$

where

$$L_G = (\mu + \omega + \lambda_G + \lambda_{CL}) > 0.$$

With the same method, we arrive at the following

$$\begin{aligned} \|H(I_{CL1}) - H(I_{CL2})\| &= \left\| \left(\frac{\beta_{CL}(I_{CL1} + \eta_C I_{GCL})}{N_H} \right) S_H + \rho_1 I_{GCL} + \epsilon_L T_{CL} \left(\frac{\beta_{CL}(I_{CL1} + \eta_C I_{GCL})}{N_H} \right) \right. \\ &\quad - \left(\frac{\xi_1 \beta_G (T_G + \eta_g I_{GCL})}{N_H} \right) I_{CL1} + \left(\frac{\beta_{CL}(I_{CL1} + \eta_C I_{GCL})}{N_H} \right) V_{CL} \\ &\quad - \left(\frac{\beta_{CL}(I_{CL2} + \eta_C I_{GCL})}{N_H} \right) S_H - \rho_1 I_{GL} - \epsilon_L T_{CL} \left(\frac{\beta_{CL}(I_{CL2} + \eta_C I_{GCL})}{N_H} \right) \\ &\quad + \left(\frac{\xi_1 \beta_G (T_G + \eta_g I_{GCL})}{N_H} \right) I_{CL2} - \left(\frac{\beta_{CL}(I_{CL1} + \eta_C I_{GCL})}{N_H} \right) V_{CL} \\ &\quad + (\mu + \tau + \delta_1) I_{CL2} - (\mu + \tau + \delta_1) I_{CL1} \Big\| \\ &\leq \beta_{CL} \sup_{0 \leq t \leq T} \left\| \frac{S_H}{N_H} \right\| \|I_{CL1} - I_{CL2}\| \tag{15} \\ &\quad + \beta_{CL} \epsilon_L \eta_g \sup_{0 \leq t \leq T} \left\| \frac{T_{CL}}{N_H} \right\| \|I_{CL1} - I_{CL2}\| + \beta_{CL} \sup_{0 \leq t \leq T} \left\| \frac{V_{CL}}{N_H} \right\| \|I_{CL1} - I_{CL2}\| \\ &\quad + \xi_1 \beta_G \sup_{0 \leq t \leq T} \left\| \frac{T_G}{N_H} \right\| \|I_{CL1} - I_{CL2}\| + \mu \|I_{CL1} - I_{CL2}\| \\ &\quad + \tau \|I_{CL1} - I_{CL2}\| + \delta_1 \|I_{CL1} - I_{CL2}\| \\ &\leq L_H \|I_{CL1} - I_{CL2}\|, \end{aligned}$$

where $L_H = (\beta_{CL}\Theta_1 + \beta_{CL}\Theta_3 + \beta_G \epsilon_L \Theta_4 + \xi_1 \beta_G \Theta_6 + \mu + \tau + \delta_1) > 0$.

$$\begin{aligned} \|K(T_{CL1}) - K(T_{CL2})\| &= \left\| \tau I_{CL} - \mu T_{CL1} - \frac{\epsilon_L \beta_{CL}(I_{CL} + \eta_C I_{GCL})}{N_H} T_{CL1} \right. \\ &\quad - \left. \tau I_{CL} + \mu T_{CL2} + \frac{\epsilon_L \beta_{CL}(I_{CL} + \eta_C I_{GCL})}{N_H} T_{CL2} \right\| \tag{16} \\ &\leq \epsilon_L \beta_{CL} \sup_{0 \leq t \leq T} \left\| \frac{I_{CL}}{N_H} \right\| \|T_{CL1} - T_{CL2}\| + \epsilon_L \beta_{CL} \eta_C \sup_{0 \leq t \leq T} \left\| \frac{I_{GCL}}{N_H} \right\| \|T_{CL1} - T_{CL2}\| \\ &\quad + \mu \|T_{CL1} - T_{CL2}\| \\ &\leq L_K \|T_{CL1} - T_{CL2}\|, \end{aligned}$$

where $L_K = (\epsilon_L \beta_{CL} \Theta_3 + \epsilon_L \beta_{CL} \Theta_7 + \mu) > 0$.

$$\begin{aligned} \|Q(I_{G1}) - Q(I_{G2})\| &= \left\| \frac{\beta_G (I_{G1} + \eta_g I_{GCL}) S_H}{N_H} + \frac{\epsilon_W \beta_G (I_{G1} + \eta_g I_{GCL}) T_G}{N_H} - (\rho + \mu + \delta_2) I_{G1} \right. \\ &\quad - \frac{\xi_2 \beta_{CL} (I_{CL} + \eta_C I_{GCL})}{N_H} + \rho_2 I_{GCL} + \frac{\beta_G (I_{G1} + \eta_g I_{GCL}) V_{CL}}{N_H} \\ &\quad + \frac{\beta_G (I_{G2} - \eta_g I_{GCL}) S_H}{N_H} - \frac{\epsilon_W \beta_G (I_{G2} - \eta_g I_{GCL}) T_G}{N_H} + (\rho + \mu + \delta_2) I_{G2} \\ &\quad + \frac{\xi_2 \beta_{CL} (I_{CL} - \eta_C I_{GCL})}{N_H} - \rho_2 I_{GCL} - \frac{\beta_G (I_{G1} + \eta_g I_{GCL}) V_{CL}}{N_H} \\ &\leq \beta_G \sup_{0 \leq t \leq T} \left\| \frac{S_H}{N_H} \right\| \|I_{G1} - I_{G2}\| + \epsilon_W \beta_G \sup_{0 \leq t \leq T} \left\| \frac{T_G}{N_H} \right\| \|I_{G1} - I_{G2}\| \\ &\quad + \mu \|I_{G1} - I_{G2}\| + \rho \|I_{G1} - I_{G2}\| + \delta_2 \|I_{G1} - I_{G2}\| + \beta_G \sup_{0 \leq t \leq T} \left\| \frac{V_{CL}}{N_H} \right\| \|I_{G1} - I_{G2}\| \\ &\leq L_Q \|I_{G1} - I_{G2}\|, \end{aligned}$$

where $L_Q = (\beta_G \Theta_1 + \beta_G \Theta_2 + \epsilon_W \beta_G \Theta_6 + \mu + \rho + \delta_2) > 0$.

$$\begin{aligned} \|U(T_{G1}) - U(T_{G2})\| &= \left\| \rho I_{G1} - \left(\mu + \frac{\epsilon \beta_G (I_G + \eta_g I_{GCL})}{N_H} \right) T_{G1} + \frac{V_{CL} \beta_G (I_G + \eta_g I_{GCL})}{N_H} \right. \\ &\quad - \left. \rho I_{G2} + \left(\mu + \frac{\epsilon \beta_G (I_G + \eta_g I_{GCL})}{N_H} \right) T_{G2} - \frac{V_{CL} \beta_G (I_G + \eta_g I_{GCL})}{N_H} \right\| \\ &\leq \epsilon \beta_G \sup_{0 \leq t \leq T} \left\| \frac{I_G}{N_H} \right\| \|T_{G1} - T_{G2}\| + \epsilon \beta_G \eta_g \sup_{0 \leq t \leq T} \left\| \frac{I_{GCL}}{N_H} \right\| \|T_{G1} - T_{G2}\| \\ &\quad + \mu \|T_{G1} - T_{G2}\|, \\ &\leq L_U \|T_{G1} - T_{G2}\|, \end{aligned}$$

where $L_U = (\epsilon \beta_G \Theta_4 + \epsilon \beta_G \eta_g \Theta_6 + \mu) > 0$.

$$\begin{aligned} \|V(I_{GCL1}) - V(I_{GCL2})\| &= \left\| \frac{\xi_1 \beta_{CL} (I_{CL} + \eta_C I_{GCL1}) I_{CL}}{N_H} + \frac{\xi_2 \beta_G (I_G + \eta_g I_{GCL1}) I_G}{N_H} \right. \\ &\quad - (\mu + \delta_1 + \rho_1 + \rho_2) I_{GCL1} + (\mu + \delta_1 + \rho_1 + \rho_2) I_{GCL2} \\ &\quad - \left. \frac{\xi_1 \beta_{CL} (I_{CL} + \eta_C I_{GCL2}) I_{CL}}{N_H} - \frac{\xi_2 \beta_G (I_G + \eta_g I_{GCL2}) I_G}{N_H} \right\| \\ &\leq \xi_1 \beta_{CL} \eta_C \sup_{0 \leq t \leq T} \left\| \frac{I_{CL}}{N_H} \right\| \|I_{GCL1} - I_{GCL2}\| \\ &\quad + \xi_2 \beta_G \eta_g \sup_{0 \leq t \leq T} \left\| \frac{I_G}{N_H} \right\| \|I_{GCL1} - I_{GCL2}\| \\ &\quad + \mu \|I_{GCL1} - I_{GCL2}\| + \delta_1 \|I_{GCL1} - I_{GCL2}\| \\ &\quad + \rho_1 \|I_{GCL1} - I_{GCL2}\| + \rho_2 \|I_{GCL1} - I_{GCL2}\| \\ &\leq L_V \|I_{GCL1} - I_{GCL2}\|, \end{aligned} \tag{17}$$

where $L_V = (\xi_1\beta_{CL}\eta_C\theta_3 + \xi_2\beta_G\eta_g\Theta_5 + \mu_4 + \delta_1 + \rho_1 + \rho_2) > 0$.

Theorem 2 Suppose $(L_F, L_G, L_H, L_K, L_Q, L_U, L_V) \frac{\Gamma(1-\zeta)\sin(\pi\zeta)T^\zeta}{\zeta\pi} < 1$, then the model (1)-(3) has a unique solution on $[0, T]$ assuming that $(F, G, H, K, Q, U, V) : [0, T] \times \mathbb{D} \rightarrow \mathbb{D}$ are continuous and satisfies the Lipschitz criteria.

Proof Considering the mapping $\vartheta : \mathbb{H}^1([0, T], \mathbb{D}) \rightarrow \mathbb{H}^1([0, T], \mathbb{D})$, where ϑ is defined in $(F, G, H, K, Q, U, V) : [0, T] \times \mathbb{D} \rightarrow \mathbb{D}$. Using (15)-(17) and for all $((S_{H1}, S_{H2}), (V_{CL1}, V_{CL2}), (I_{CL1}, I_{CL2}), (T_{CL1}, T_{CL2}), (I_{G1}, I_{G2}), (T_{G1}, T_{G2}), (I_{GCL1}, I_{GCL2}),) \in \mathbb{H}^1([0, T], \mathbb{D})$ and $0 \leq t \leq T$ we get

$$\begin{aligned} \|\vartheta(S_{H1}(t)) - \vartheta(S_{H2}(t))\| &= \left\| S_H(0) + \frac{1}{\Gamma(\zeta)} \int_0^t (t-\tau)^{\zeta-1} F(t, S_{H1}(\tau)) d\tau - \right. \\ &\quad \left. - \left(S_H(0) + \frac{1}{\Gamma(\zeta)} \int_0^t (t-\tau)^{\zeta-1} F(t, S_{H2}(\tau)) d\tau \right) \right\| \\ &\leq \frac{1}{\Gamma(\zeta)} \int_0^t (t-\tau)^{\zeta-1} \|F(t, S_{H1}(\tau)) - F(t, S_{H2}(\tau))\| d\tau \\ &\leq \frac{L_F}{\Gamma(\zeta)} \int_0^t (t-\tau)^{\zeta-1} \|S_{H1}(\tau) - S_{H2}(\tau)\| d\tau \\ &\leq L_F \left(\frac{T^\zeta}{\Gamma(\zeta+1)} \right) \|S_{H1} - S_{H2}\|_{\mathbb{H}^1}. \end{aligned}$$

Similar process yields

$$\begin{aligned} \|\vartheta(V_{CL1}(t)) - \vartheta(V_{CL2}(t))\| &\leq L_G \left(\frac{T^\zeta}{\Gamma(\zeta+1)} \right) \|V_{CL1} - V_{CL2}\|_{\mathbb{H}^1}, \\ \|\vartheta(I_{CL1}(t)) - \vartheta(I_{CL2}(t))\| &\leq L_H \left(\frac{T^\zeta}{\Gamma(\zeta+1)} \right) \|I_{CL1} - I_{CL2}\|_{\mathbb{H}^1}, \\ \|\vartheta(T_{CL1}(t)) - \vartheta(T_{CL2}(t))\| &\leq L_K \left(\frac{T^\zeta}{\Gamma(\zeta+1)} \right) \|T_{CL1} - T_{CL2}\|_{\mathbb{H}^1}, \\ \|\vartheta(I_{G1}(t)) - \vartheta(I_{G2}(t))\| &\leq L_Q \left(\frac{T^\zeta}{\Gamma(\zeta+1)} \right) \|I_{G1} - I_{G2}\|_{\mathbb{H}^1}, \\ \|\vartheta(T_{G1}(t)) - \vartheta(T_{G2}(t))\| &\leq L_U \left(\frac{T^\zeta}{\Gamma(\zeta+1)} \right) \|T_{G1} - T_{G2}\|_{\mathbb{H}^1}, \\ \|\vartheta(I_{GCL1}(t)) - \vartheta(I_{GCL2}(t))\| &\leq L_V \left(\frac{T^\zeta}{\Gamma(\zeta+1)} \right) \|I_{GCL1} - I_{GCL2}\|_{\mathbb{H}^1}. \end{aligned} \tag{18}$$

It is evident from the condition that $(L_F, L_G, L_H, L_K, L_Q, L_U, L_V) \frac{\Gamma(1-\zeta)\sin(\pi\zeta)T^\zeta}{\zeta\pi} < 1$. The application of the Banach contraction mapping principle reveals that the parameter ϑ has a distinct fixed point in $0 \leq t \leq T$. since it is a contraction mapping. ■

Utilizing Schaefer’s fixed point theorem, we investigate the fractional model (1)-(3) existence of solutions.

Theorem 3 Given that $(F, G, H, K, Q, U, V) : [0, T] \times \mathbb{D} \rightarrow \mathbb{D}$ are continuous and that there exist constants $(L_{F1}, L_{G1}, L_{H1}, L_{K1}, L_{Q1}, L_{U1}, L_{V1}) > 0$ such that

$$\|F(t, S_H)\| \leq L_{F1} (c + \|S_H\|), \quad \|G(t, V_{CL})\| \leq L_{G1} (c + \|V_{CL}\|),$$

$$\|H(t, I_{CL})\| \leq L_{H1} (c + \|I_{CL}\|), \quad \|K(t, T_{CL})\| \leq L_{K1} (c + \|T_{CL}\|),$$

$$\|Q(t, I_G)\| \leq L_{Q1} (c + \|I_G\|), \quad \|U(t, T_G)\| \leq L_{U1} (c + \|T_G\|), \quad \|V(t, I_{GCL})\| \leq L_{V1} (c + \|I_{GCL}\|),$$

where $0 < c \leq 1$ is an arbitrary number, then (1)-(3) has at least one solution.

Proof From (18) we have that the operator ϑ is continuous. Let $\{S_H^{m+1}\}_\infty, \{V_{CL}^{m+1}\}_\infty, \{I_{CL}^{m+1}\}_\infty, \{T_{CL}^{m+1}\}_\infty, \{I_G^{m+1}\}_\infty, \{T_G^{m+1}\}_\infty, \{I_{GCL}^{m+1}\}_\infty$, be sequences such that $S_H^{m+1} \rightarrow S_H^m, V_{CL}^{m+1} \rightarrow V_{CL}^m, I_{CL}^{m+1} \rightarrow I_{CL}^m, T_{CL}^{m+1} \rightarrow T_{CL}^m, I_G^{m+1} \rightarrow I_G^m, T_G^{m+1} \rightarrow T_G^m, I_{GCL}^{m+1} \rightarrow I_{GCL}^m$, in $\mathbb{H}^1([0, T], \mathbb{D})$. For each $0 \leq t \leq T$ we have that

$$\begin{aligned} \|\vartheta S_H^{m+1}(t) - \vartheta S_H^m(t)\| &= \frac{1}{\Gamma(\zeta)} \left\| \int_0^t (t-\tau)^{\zeta-1} F(t, S_H^{m+1}(\tau)) d\tau - \int_0^t (t-\tau)^{\zeta-1} F(t, S_H^m(\tau)) d\tau \right\| \\ &\leq \frac{1}{\Gamma(\zeta)} \int_0^t (t-\tau)^{\zeta-1} \|F(t, S_H^{m+1}(\tau)) - F(t, S_H^m(\tau))\| d\tau \\ &\leq \frac{L_{F1} T^\zeta}{\Gamma(\zeta+1)} \|S_H^{m+1} - S_H^m\|, \end{aligned} \tag{19}$$

where $\|S_H^{m+1} - S_H^m\|_{\mathbb{H}^1} \rightarrow 0$ as $m \rightarrow \infty$. Using the same methodology yields

$$\begin{aligned} \|\vartheta V_{CL}^{m+1}(t) - \vartheta V_{CL}^m(t)\| &\leq L_{G1} \left(\frac{T^\zeta}{\Gamma(\zeta+1)} \right) \|V_{CL}^{m+1} - V_{CL}^m\|_{\mathbb{H}^1}, \\ \|\vartheta I_{CL}^{m+1}(t) - \vartheta I_{CL}^m(t)\| &\leq L_{H1} \left(\frac{T^\zeta}{\Gamma(\zeta+1)} \right) \|I_{CL}^{m+1} - I_{CL}^m\|_{\mathbb{H}^1}, \\ \|\vartheta T_{CL}^{m+1}(t) - \vartheta T_{CL}^m(t)\| &\leq L_{K1} \left(\frac{T^\zeta}{\Gamma(\zeta+1)} \right) \|T_{CL}^{m+1} - T_{CL}^m\|_{\mathbb{H}^1}, \\ \|\vartheta I_G^{m+1}(t) - \vartheta I_G^m(t)\| &\leq L_{Q1} \left(\frac{T^\zeta}{\Gamma(\zeta+1)} \right) \|I_G^{m+1} - I_G^m\|_{\mathbb{H}^1}, \\ \|\vartheta T_G^{m+1}(t) - \vartheta T_G^m(t)\| &\leq L_{U1} \left(\frac{T^\zeta}{\Gamma(\zeta+1)} \right) \|T_G^{m+1} - T_G^m\|_{\mathbb{H}^1}, \\ \|\vartheta I_{GCL}^{m+1}(t) - \vartheta I_{GCL}^m(t)\| &\leq L_{F1} \left(\frac{T^\zeta}{\Gamma(\zeta+1)} \right) \|I_{GCL}^{m+1} - I_{GCL}^m\|_{\mathbb{H}^1}, \end{aligned}$$

where $\|V_{CL}^{m+1} - V_{CL}^m\|_{\mathbb{H}^1} \rightarrow 0, \|I_{CL}^{m+1} - I_{CL}^m\|_{\mathbb{H}^1} \rightarrow 0, \|T_{CL}^{m+1} - T_{CL}^m\|_{\mathbb{H}^1} \rightarrow 0, \|I_G^{m+1} - I_G^m\|_{\mathbb{H}^1} \rightarrow 0, \|T_G^{m+1} - T_G^m\|_{\mathbb{H}^1} \rightarrow 0, \|I_{GCL}^{m+1} - I_{GCL}^m\|_{\mathbb{H}^1} \rightarrow 0$, as $m \rightarrow \infty$. Thus the operator ϑ is continuous. \blacksquare

Next, we show that the operator ϑ is a one-to-one bounded function on the set of $\mathbb{H}^1([0, T], \mathbb{D})$. For each $S_H \in B_{S_H}, V_{CL} \in B_{V_{CL}}, I_{CL} \in B_{I_{CL}}, T_{CL} \in B_{T_{CL}}, I_G \in B_{I_G}, T_G \in B_{T_G}, I_{GCL} \in B_{I_{GCL}}$

and for $a > 0$, there corresponds a value $b > 0$ where $\|\vartheta S_H\| \leq b$, $\|\vartheta S_H\| \leq b$, $\|\vartheta V_{CL}\| \leq b$, $\|\vartheta I_{CL}\| \leq b$, $\|\vartheta T_{CL}\| \leq b$, $\|\vartheta I_G\| \leq b$, $\|\vartheta T_G\| \leq b$, $\|\vartheta I_{GCL}\| \leq b$, and the subset of Banach space of all continuous functions on the interval $0 \leq t \leq T$ are defined by

$$B_{S_H} = \left\{ S_H \in \mathbb{H}^1([0, T], \mathbb{D}) : \|S_H\| \leq a \right\}, \quad B_{V_{CL}} = \left\{ V_{CL} \in \mathbb{H}^1([0, T], \mathbb{D}) : \|V_{CL}\| \leq a \right\},$$

$$B_{I_{CL}} = \left\{ I_{CL} \in \mathbb{H}^1([0, T], \mathbb{D}) : \|I_{CL}\| \leq a \right\}, \quad B_{T_{CL}} = \left\{ T_{CL} \in \mathbb{H}^1([0, T], \mathbb{D}) : \|T_{CL}\| \leq a \right\},$$

$$B_{I_G} = \left\{ I_G \in \mathbb{H}^1([0, T], \mathbb{D}) : \|I_G\| \leq a \right\}, \quad B_{T_G} = \left\{ T_G \in \mathbb{H}^1([0, T], \mathbb{D}) : \|T_G\| \leq a \right\},$$

$$B_{I_{GCL}} = \left\{ I_{GCL} \in \mathbb{H}^1([0, T], \mathbb{D}) : \|I_{GCL}\| \leq a \right\}.$$

So for any $0 \leq t \leq T$,

$$\begin{aligned} \|\vartheta S_H\| &\leq \|S_H(0)\| + \frac{1}{\Gamma(\zeta)} \int_0^t (t-\tau)^{\zeta-1} \|F(t, S_H(t))\| d\tau \\ &\leq \|S_H(0)\| + \frac{\|F(t, S_H(t))\|}{\Gamma(\zeta)} \int_0^t (t-\tau)^{\zeta-1} d\tau \\ &\leq \|S_H(0)\| + L_{F1} (c + \|S_H\|) \left(\frac{T^\zeta}{\Gamma(\zeta + 1)} \right) \\ &\leq \|S_H(0)\| + L_{F1} (c + a) \left(\frac{T^\zeta}{\Gamma(\zeta + 1)} \right). \end{aligned}$$

Following a similar approach we have

$$\begin{aligned} \|\vartheta V_{CL}\| &\leq \|V_{CL}(0)\| + L_{G1} (c + a) \left(\frac{T^\zeta}{\Gamma(\zeta + 1)} \right), \\ \|\vartheta I_{CL}\| &\leq \|I_{CL}(0)\| + L_{H1} (c + a) \left(\frac{T^\zeta}{\Gamma(\zeta + 1)} \right), \\ \|\vartheta T_{CL}\| &\leq \|T_{CL}(0)\| + L_{K1} (c + a) \left(\frac{T^\zeta}{\Gamma(\zeta + 1)} \right), \\ \|\vartheta I_G\| &\leq \|I_G(0)\| + L_{Q1} (c + a) \left(\frac{T^\zeta}{\Gamma(\zeta + 1)} \right), \\ \|\vartheta T_G\| &\leq \|T_G(0)\| + L_{U1} (c + a) \left(\frac{T^\zeta}{\Gamma(\zeta + 1)} \right), \\ \|\vartheta I_{GCL}\| &\leq \|I_{GCL}(0)\| + L_{V1} (c + a) \left(\frac{T^\zeta}{\Gamma(\zeta + 1)} \right). \end{aligned}$$

On the other hand, let Ω maps bounded set into equal continuous sets in $\mathbb{H}^1([0, T], \mathbb{D})$. If $0 \leq t_1 \leq t_2 \leq T$, $S_H \in B_{S_H}$, $V_{CL} \in B_{V_{CL}}$, $I_{CL} \in B_{I_{CL}}$, $T_{CL} \in B_{T_{CL}}$, $I_G \in B_{I_G}$, $T_G \in B_{T_G}$, $I_{GCL} \in B_{I_{GCL}}$,

where $t_1, t_2 \in [0, T]$, then

$$\begin{aligned} \|\vartheta S_H(t_1) - \vartheta S_H(t_2)\| &= \frac{1}{\Gamma(\zeta)} \left\| \int_0^{t_1} (t_1 - \tau)^{\zeta-1} F(t, S_H(t)) - \int_0^{t_2} (t_2 - \tau)^{\zeta-1} F(t, S_H(t)) \right\| d\tau \\ &\leq \frac{1}{\Gamma(\zeta)} \left\| \int_0^{t_1} \left((t_1 - \tau)^{\zeta-1} - (t_2 - \tau)^{\zeta-1} \right) F(t, S_H(t)) d\tau \right\| \\ &\quad + \frac{1}{\Gamma(\zeta)} \left\| \int_{t_1}^{t_2} (t_2 - \tau)^{\zeta-1} F(t, S_h(t)) d\tau \right\| \\ &\leq \frac{L_{F1}(c+a)}{\Gamma(\zeta)} \left\| \int_0^{t_1} \left((t_1 - \tau)^{\zeta-1} - (t_2 - \tau)^{\zeta-1} \right) d\tau + \int_{t_1}^{t_2} (t_2 - \tau)^{\zeta-1} d\tau \right\| \\ &\leq \left(\frac{L_{F1}(c+a) T^\zeta}{\Gamma(\zeta+1)} \right) \left(t_1^\zeta - t_2^\zeta + 2(t_2 - t_1)^\zeta \right). \end{aligned}$$

Similar approach produces

$$\begin{aligned} \|\vartheta V_{CL}(t_1) - \vartheta V_{CL}(t_2)\| &\leq \left(\frac{L_{G1}(c+a) T^\zeta}{\Gamma(\zeta+1)} \right) \left(t_1^\zeta - t_2^\zeta + 2(t_2 - t_1)^\zeta \right), \\ \|\vartheta I_{CL}(t_1) - \vartheta I_{CL}(t_2)\| &\leq \left(\frac{L_{H1}(c+a) T^\zeta}{\Gamma(\zeta+1)} \right) \left(t_1^\zeta - t_2^\zeta + 2(t_2 - t_1)^\zeta \right), \\ \|\vartheta T_{CL}(t_1) - \vartheta T_{CL}(t_2)\| &\leq \left(\frac{L_{K1}(c+a) T^\zeta}{\Gamma(\zeta+1)} \right) \left(t_1^\zeta - t_2^\zeta + 2(t_2 - t_1)^\zeta \right), \\ \|\vartheta I_{CL}(t_1) - \vartheta I_{CL}(t_2)\| &\leq \left(\frac{L_{Q1}(c+a) T^\zeta}{\Gamma(\zeta+1)} \right) \left(t_1^\zeta - t_2^\zeta + 2(t_2 - t_1)^\zeta \right), \\ \|\vartheta T_G(t_1) - \vartheta T_G(t_2)\| &\leq \left(\frac{L_{U1}(c+a) T^\zeta}{\Gamma(\zeta+1)} \right) \left(t_1^\zeta - t_2^\zeta + 2(t_2 - t_1)^\zeta \right), \\ \|\vartheta I_{GCL}(t_1) - \vartheta I_{GCL}(t_2)\| &\leq \left(\frac{L_{V1}(c+a) T^\zeta}{\Gamma(\zeta+1)} \right) \left(t_1^\zeta - t_2^\zeta + 2(t_2 - t_1)^\zeta \right). \end{aligned}$$

As $t_1 \rightarrow t_2$ on the right side of the inequality, the expression tends to zero. ϑ is a continuous function, following the Arzela-Ascoli theorem. Now, to show that $R(\vartheta) = \{(S_H, V_{CL}, I_{CL}, T_{CL}, I_G, T_G, I_{GCL}) \in \mathbb{H}^1([0, T], \mathbb{D}) : (S_H, V_{CL}, I_{CL}, T_{CL}, I_G, T_G, I_{GCL}) = \lambda (S_H, V_{CL}, I_{CL}, T_{CL}, I_G, T_G, I_{GCL})\}$ is bounded for some $\lambda \in (0, 1)$ by (1). Suppose $(S_H, V_{CL}, I_{CL}, T_{CL}, I_G, T_G, I_{GCL}) \in R(\vartheta)$, such that $(S_H, V_{CL}, I_{CL}, T_{CL}, I_G, T_G, I_{GCL}) = \lambda \vartheta (S_H, V_{CL}, I_{CL}, T_{CL}, I_G, T_G, I_{GCL})$, for each $t \in [0, T]$ gives

$$\begin{aligned} \|S_H(t)\| &\leq S_H(0) + \frac{1}{\Gamma(\zeta)} \int_0^T (t - \tau)^{\zeta-1} \|F(t, S_H(t))\| d\tau \\ &\leq S_H(0) + \frac{L_{F1}}{\Gamma(\zeta)} \int_0^T (t - \tau)^{\zeta-1} (c + \|S_H(t)\|) d\tau \\ &\leq S_H(0) + \frac{cL_{F1}}{\Gamma(\zeta)} \int_0^T (t - \tau)^{\zeta-1} d\tau + \frac{L_{F1}}{\Gamma(\zeta)} \int_0^T (t - \tau)^{\zeta-1} \|S_H(t)\| d\tau \tag{20} \\ &\leq S_H(0) + \left(L_{F1} \frac{T^\zeta}{\Gamma(\zeta+1)} \right) + \left(\frac{L_{F1} T^\zeta}{\Gamma(\zeta+1)} \right) \int_0^T (t - \tau)^{\zeta-1} \|S_H(t)\| d\tau \\ &\leq \left(S_H(0) + \frac{L_{F1} T^\zeta}{\Gamma(\zeta+1)} E_\zeta(L_{F1} T^\zeta) \right) < \infty. \end{aligned}$$

Following a similar approach we have

$$\begin{aligned} \|V_{CL}(t)\| &\leq \left(V_{CL}(0) + \frac{L_{G1}T^\zeta}{\Gamma(\zeta + 1)} E_\zeta \left(L_{G1}T^\zeta \right) \right) < \infty, \\ \|I_{CL}(t)\| &\leq \left(I_{CL}(0) + \frac{L_{H1}T^\zeta}{\Gamma(\zeta + 1)} E_\zeta \left(L_{H1}T^\zeta \right) \right) < \infty, \\ \|T_{CL}(t)\| &\leq \left(T_{CL}(0) + \frac{L_{FK1}T^\zeta}{\Gamma(\zeta + 1)} E_\zeta \left(L_{K1}T^\zeta \right) \right) < \infty, \\ \|I_G(t)\| &\leq \left(I_G(0) + \frac{L_{FQ1}T^\zeta}{\Gamma(\zeta + 1)} E_\zeta \left(L_{Q1}T^\zeta \right) \right) < \infty, \\ \|T_G(t)\| &\leq \left(T_G(0) + \frac{L_{U1}T^\zeta}{\Gamma(\zeta + 1)} E_\zeta \left(L_{U1}T^\zeta \right) \right) < \infty, \\ \|I_{GCL}(t)\| &\leq \left(I_{GCL}(0) + \frac{L_{V1}T^\zeta}{\Gamma(\zeta + 1)} E_\zeta \left(L_{V1}T^\zeta \right) \right) < \infty. \end{aligned}$$

Since we have proved that $R(\vartheta)$ is bounded, ϑ has a fixed point given by Schaefer’s fixed point theorem and hence the solution of the model.

Basic reproduction number of the model

The Disease Free Equilibrium (DFE) of the co-infection model is given by

$$\begin{aligned} \xi_0 &= (S_h^0, V_{CL}^0, I_{CL}^0, T_{CL}^0, I_G^0, T_G^0, I_{GCL}^0) \\ &= \left(\frac{\Lambda_H + \omega V_{CL}}{\mu + \gamma}, \frac{\gamma S_H}{\mu + \omega}, 0, 0, 0, 0, 0 \right), \end{aligned} \tag{21}$$

$$V = \begin{bmatrix} (\mu + \tau + \delta_1) & 0 & -\rho_1 \\ 0 & (\mu + \rho + \delta_2) & 0 \\ 0 & 0 & (\mu + \delta_3 + \rho_1 + \rho_2) \end{bmatrix}, \quad F = \begin{pmatrix} \frac{S_H \beta_{CL}}{N_H} & 0 & \frac{S_H \eta_L \beta_{CL}}{N_H} \\ 0 & \frac{S_H \beta_G}{N_H} & \frac{S_H \beta_G}{N_H} \\ 0 & 0 & 0 \end{pmatrix},$$

$$\mathcal{R}_0 = |FV^{-1} - \lambda I|.$$

The basic reproduction number of the model obtained and stated below, using the approach illustrated in [43], is given by $\mathcal{R}_0 = \max\{\mathcal{R}_{0CL}, \mathcal{R}_{0Go}\}$ where \mathcal{R}_{0CL} and \mathcal{R}_{0Go} are, respectively, the Chlamydia and Gonorrhoea associated reproduction numbers, given by

$$\mathcal{R}_{0CL} = \frac{S_H^* \beta_{CL}}{N_H^* (\tau + \mu + \delta_1)}, \quad \text{and} \quad \mathcal{R}_{0Go} = \frac{S_H^* \beta_G}{N_H^* (\rho + \mu + \delta_2)}.$$

Generalized Ulam-Hyers-Rassias stability

We investigate the stability of the fractional model system using the Ulam-Hyers-Rassias(UHR) Stability method as given in [42] to demonstrate UHR stability of the model.

Definition 4 *The fractional model (1)-(3) is generalized Ulam-Hyers-Rassias (UHR) stable with respect to $\Omega(t) \in \mathbb{H}^1([0, T], \mathbb{D})$ if there exists a real value $\kappa_\epsilon > 0$ with $\epsilon > 0$ and for all solution*

$(S_H, V_{CL}, I_{CL}, T_{CL}, I_G, T_G, I_{GCL}) \in \mathbb{H}^1([0, T], \mathbb{D})$ of the following inequalities

$$\left| D_t^\zeta S_H(t) - F(t, S_H(t)) \right| \leq \Omega(t), \quad \left| D_t^\zeta V_{CL}(t) - G(t, V_{CL}(t)) \right| \leq \Omega(t),$$

$$\left| D_t^\zeta I_{CL}(t) - H(t, I_{CL}(t)) \right| \leq \Omega(t), \quad \left| D_t^\zeta T_{CL}(t) - K(t, T_{CL}(t)) \right| \leq \Omega(t),$$

$$\left| D_t^\zeta T_G(t) - Q(t, T_G(t)) \right| \leq \Omega(t), \quad \left| D_t^\zeta I_{GCL}(t) - V(t, I_{GCL}(t)) \right| \leq \Omega(t),$$

there exists a solution $(\bar{S}_H, \bar{V}_{CL}, \bar{I}_{CL}, \bar{T}_{CL}, \bar{I}_G, \bar{T}_G, \bar{I}_{GCL},) \in \mathbb{H}^1([0, T], \mathbb{D})$ of the model (1)-(3) with

$$|S_H(t) - \bar{S}_H(t)| \leq \kappa_\epsilon \Omega(t), \quad |V_{CL}(t) - \bar{V}_{CL}(t)| \leq \kappa_\epsilon \Omega(t), \quad |I_{CL}(t) - \bar{I}_{CL}(t)| \leq \kappa_\epsilon \Omega(t),$$

$$|T_{CL}(t) - \bar{T}_{CL}(t)| \leq \kappa_\epsilon \Omega(t),$$

$$|I_G(t) - \bar{I}_G(t)| \leq \kappa_\epsilon \Omega(t), \quad |T_G(t) - \bar{T}_G(t)| \leq \kappa_\epsilon \Omega(t), \quad |I_{GCL}(t) - \bar{I}_{GCL}(t)| \leq \kappa_\epsilon \Omega(t).$$

Theorem 4 In relation to $\Omega \in \mathbb{H}^1([0, T], \mathbb{D})$, the fractional model (1)-(3) are generalized Ulam-Hyers-Rassias stable if $(L_F, L_G, L_H, L_K, L_Q, L_V) T^\zeta < 1$.

Proof From definition (4), denoting Ω as a non-decreasing function of t , then there exists $\epsilon > 0$ such that

$$\int_0^t (t - \tau)^{\zeta-1} \Omega(t) d\tau \leq \epsilon \Omega(t),$$

for every $t \in [0, T]$. Where It has been demonstrated that the functions F, G, H, K, Q, V are continuous and $(L_F, L_G, L_H, L_K, L_Q, L_V) > 0$ satisfies the Lipschitz condition as described in the preceding section. The fractional model (1)-(3) unique solution comes from Theorem (2)

$$\bar{S}_H(t) = S_H(0) + \frac{1}{\Gamma(\zeta)} \int_0^t (t - \tau)^{\zeta-1} F(t, \bar{S}_H(t)) d\tau.$$

Integrating the inequalities in Definition (4) we get

$$\begin{aligned} \left| S_H(t) - S_H(0) - \frac{1}{\Gamma(\zeta)} \int_0^t (t - \tau)^{\zeta-1} F(t, S_H(t)) d\tau \right| &\leq \frac{1}{\Gamma(\zeta)} \int_0^t (t - \tau)^{\zeta-1} \Omega(t) d\tau, \\ &\leq \frac{\epsilon \Omega(t) T^\zeta}{\Gamma(\zeta + 1)}. \end{aligned} \tag{22}$$

Using Lemma 1 and Eq. (22), we get

$$\begin{aligned}
 |S_H(t) - \bar{S}_H(t)| &\leq \left| S_H(t) - \left(S_H(0) + \frac{1}{\Gamma(\zeta)} \int_0^t (t-\tau)^{\zeta-1} F(t, \bar{S}_H(t)) d\tau \right) \right| \\
 &\leq \left| S_H(t) - S_H(0) - \left(\frac{1}{\Gamma(\zeta)} \int_0^t (t-\tau)^{\zeta-1} F(t, \bar{S}_H(t)) d\tau \right. \right. \\
 &\quad \left. \left. + \frac{1}{\Gamma(\zeta)} \int_0^t (t-\tau)^{\zeta-1} F(t, S_H(t)) d\tau - \frac{1}{\Gamma(\zeta)} \int_0^t (t-\tau)^{\zeta-1} F(t, S_H(t)) d\tau \right) \right| \\
 &\leq \left| S_H(t) - S_H(0) - \frac{1}{\Gamma(\zeta)} \int_0^t (t-\tau)^{\zeta-1} F(t, S_H(t)) d\tau \right| \\
 &\quad + \frac{1}{\Gamma(\zeta)} \int_0^t (t-\tau)^{\zeta-1} |F(t, S_H(t)) - F(t, \bar{S}_H(t))| d\tau \\
 &\leq \frac{\epsilon \Omega(t) T^\zeta}{\Gamma(\zeta+1)} + \frac{L_F T^\zeta}{\Gamma(\zeta+1)} \int_0^t (t-\tau)^{\zeta-1} |S_H(t) - \bar{S}_H(t)| d\tau \\
 &\leq \frac{\epsilon \Omega(t) T^\zeta}{\Gamma(\zeta+1)} E_\zeta (L_F T^\zeta).
 \end{aligned}$$

By setting $\kappa_\zeta = \frac{\epsilon T^\zeta}{\Gamma(\zeta+1)} E_\zeta (L_F T^\zeta)$, we have

$$|S_H(t) - \bar{S}_H(t)| \leq \kappa_\zeta \Omega(t), \quad t \in [0, T].$$

Using a similar method, we obtain

$$|V_{CL}(t) - \bar{V}_{CL}(t)| \leq \kappa_\zeta \Omega(t), \quad |I_{CL}(t) - \bar{I}_{CL}(t)| \leq \kappa_\zeta \Omega(t), \quad |T_{CL}(t) - \bar{T}_{CL}(t)| \leq \kappa_\zeta \Omega(t),$$

$$|I_G(t) - \bar{I}_G(t)| \leq \kappa_\zeta \Omega(t), \quad |I_{GCL}(t) - \bar{I}_{GCL}(t)| \leq \kappa_\zeta \Omega(t), \quad t \in [0, T].$$

Consequently, this indicates that the model is UHR-stable in general with regard to $\Omega(t)$. ■

The disease-free equilibrium’s global asymptotic stability (GAS)

Theorem 5 Consider the model equation (1) with the DFE (21) given by \mathcal{E}_0 , the DFE \mathcal{E}_0 of the model is globally asymptotically stable in \mathcal{D} whenever $\mathcal{R}_0 \leq 1$.

We use the method presented in [44] to investigate global stability.

$$D_t^\zeta X = F(X, W) = \begin{bmatrix} \Lambda_H - (\lambda_G + \lambda_{CL})S_H + \omega V_{CL} - (\mu + \gamma)S_H \\ \gamma S_H - (\mu + \omega)V_{CL} - V_{CL}(\lambda_G + \lambda_{CL}) \\ \tau I_{CL} - (\mu + \epsilon_L \lambda_{CL})T_{CL} + V_{CL} \lambda_{CL} \\ p I_G - (\mu + \epsilon_W \lambda_G)T_G + V_{CL} \lambda_G \end{bmatrix}, \tag{23}$$

$$F(X, 0) = \begin{bmatrix} \Lambda_H + \omega V_{CL} - (\mu + \gamma)S_H \\ \gamma S_H - (\mu + \omega)V_{CL} \\ -\mu T_{CL} \\ -\mu T_G \end{bmatrix}, \tag{24}$$

$$\frac{dW}{dt} = \begin{bmatrix} \lambda_{CL}S_H + \epsilon_L\lambda_{CL}T_{CL} - (\mu + \tau + \delta_1)I_{CL} - \xi_1\lambda_G I_{CL} + \rho_1 I_{GCL} \\ \lambda_G S_H + \epsilon_W\lambda_G T_G - (\rho + \mu + \delta_2)I_G - \xi_2\lambda_{CL}I_G + \rho_2 I_{GCL} \\ \xi_1\lambda_G I_{CL} + \xi_2\lambda_{CL}I_G - (\mu + \delta_3 + \rho_1 + \rho_2)I_{GCL} \end{bmatrix}, \quad (25)$$

$$A = \begin{bmatrix} \frac{\beta_{CL}(S_H + \epsilon_L T_{CL})}{N} - (\mu + \tau + \delta_1) & 0 & \frac{\beta_{CL}\eta_c(S_H + \epsilon_L T_{CL})}{N} + \rho_1 \\ 0 & \frac{\beta_G(S_H + \epsilon_W T_G)}{N} - (\rho + \mu + \delta_2) & \frac{\beta_G\eta_g(S_H + \epsilon_W T_G)}{N} + \rho_2 \\ \xi_1\lambda_G & \xi_2\lambda_{CL} & -(\mu + \delta_3 + \rho_1 + \rho_2) \end{bmatrix}, \quad (26)$$

$$AW = \begin{bmatrix} \frac{I_{CL}\beta_{CL}(S_H + \epsilon_L T_{CL})}{N} - I_{CL}(\mu + \tau + \delta_1) + \frac{I_{GCL}\beta_{CL}\eta_c(S_H + \epsilon_L T_{CL})}{N} + I_{GCL}\rho_1 \\ \frac{I_G\beta_G(S_H + \epsilon_W T_G)}{N} - I_G(\rho + \mu + \delta_2) + \frac{I_{GCL}\beta_G\eta_g(S_H + \epsilon_W T_G)}{N} + I_{GCL}\rho_2 \\ I_{CL}\xi_1\lambda_G + I_G\xi_2\lambda_{CL} - I_{GCL}(\mu + \delta_3 + \rho_1 + \rho_2) \end{bmatrix}, \quad (27)$$

$$\tilde{G}(X, W) = AW - G(X, W) = \begin{bmatrix} \xi_1\lambda_G I_{CL} \\ \xi_2\lambda_{CL} I_G \\ 0 \end{bmatrix}.$$

Since $\hat{G}(X, W) \geq 0$, this gives that the DFE is globally asymptotically stable.

3 Numerical scheme and algorithms

If $t_k = kh, k = 0, 1, 2, \dots, m$ be the uniform grid points represented by some integer m and the grid step size represented by $(h = T/m)$. Then, using piece-wise interpolation and knots and nodes located at $t_j, j = 0, 1, 2, \dots, k + 1$, the fractional version of the one-step Adam-Moulton method is reduced to equation (13) (Corrector formula as described in [45]);

$$\begin{aligned} S_H(t_{k+1}) - S_H(0) &= \frac{h^\zeta}{\Gamma(\zeta + 2)} \left(\sum_{j=0}^k u_{j,k+1} F(t_j, S_H(t_j)) + F(t_{k+1}, S_H^p(t_{k+1})) \right), \\ V_{CL}(t_{k+1}) - V_{CL}(0) &= \frac{h^\zeta}{\Gamma(\zeta + 2)} \left(\sum_{j=0}^k u_{j,k+1} G(t_j, V_{CL}(t_j)) + G(t_{k+1}, I_{CL}^p(t_{k+1})) \right), \\ I_{CL}(t_{k+1}) - I_{CL}(0) &= \frac{h^\zeta}{\Gamma(\zeta + 2)} \left(\sum_{j=0}^k u_{j,k+1} H(t_j, I_{CL}(t_j)) + H(t_{k+1}, I_{CL}^p(t_{k+1})) \right), \\ T_{CL}(t_{k+1}) - T_{CL}(0) &= \frac{h^\zeta}{\Gamma(\zeta + 2)} \left(\sum_{j=0}^k u_{j,k+1} K(t_j, T_{CL}(t_j)) + K(t_{k+1}, T_{CL}^p(t_{k+1})) \right), \\ I_G(t_{k+1}) - I_G(0) &= \frac{h^\zeta}{\Gamma(\zeta + 2)} \left(\sum_{j=0}^k u_{j,k+1} Q(t_j, I_G(t_j)) + Q(t_{k+1}, I_G^p(t_{k+1})) \right), \\ T_G(t_{k+1}) - T_G(0) &= \frac{h^\zeta}{\Gamma(\zeta + 2)} \left(\sum_{j=0}^k u_{j,k+1} U(t_j, T_G(t_j)) + U(t_{k+1}, T_G^p(t_{k+1})) \right), \end{aligned} \quad (28)$$

$$I_{GCL}(t_{k+1}) - I_{GCL}(0) = \frac{h^\zeta}{\Gamma(\zeta + 2)} \left(\sum_{j=0}^k u_{j,k+1} V(t_j, I_{GCL}(t_j)) + V(t_{k+1}, I_{GCL}^p(t_{k+1})) \right),$$

given the weight

$$u_{j,k+1} = \begin{cases} k^{\zeta+1} - (k - \zeta)(k + 1)^\zeta, & j = 0. \\ (k - j + 2)^{\zeta+1} + (k - j)^{\zeta+1} - 2(k - j + 1)^{\zeta+1}, & 1 \leq j \leq k. \\ 1, & j = k + 1. \end{cases}$$

Based on the well-known one-step Adams-Bashforth method, the predictor formula is provided by

$$\begin{aligned} S_H^p(t_{k+1}) - S_H(0) &= \frac{1}{\Gamma(\zeta)} \sum_{j=0}^k v_{j,k+1} F(t_j, S_H(t_j)), \\ V_{CL}^p(t_{k+1}) - V_{CL}(0) &= \frac{1}{\Gamma(\zeta)} \sum_{j=0}^k v_{j,k+1} G(t_j, V_{CL}(t_j)), \\ I_{CL}^p(t_{k+1}) - I_{CL}(0) &= \frac{1}{\Gamma(\zeta)} \sum_{j=0}^k v_{j,k+1} H(t_j, I_{CL}(t_j)), \\ T_{CL}^p(t_{k+1}) - T_{CL}(0) &= \frac{1}{\Gamma(\zeta)} \sum_{j=0}^k v_{j,k+1} K(t_j, T_{CL}(t_j)), \\ I_G^p(t_{k+1}) - I_G(0) &= \frac{1}{\Gamma(\zeta)} \sum_{j=0}^k v_{j,k+1} Q(t_j, I_G(t_j)), \\ T_G^p(t_{k+1}) - T_G(0) &= \frac{1}{\Gamma(\zeta)} \sum_{j=0}^k v_{j,k+1} U(t_j, T_G(t_j)), \\ I_{GCL}^p(t_{k+1}) - I_{GCL}(0) &= \frac{1}{\Gamma(\zeta)} \sum_{j=0}^k v_{j,k+1} V(t_j, I_{GCL}(t_j)), \end{aligned} \tag{29}$$

given the weight

$$v_{j,k+1} = \zeta^{-1} h^\zeta \left((k - j + 1)^\zeta - (k - j)^\zeta \right).$$

4 Numerical simulations

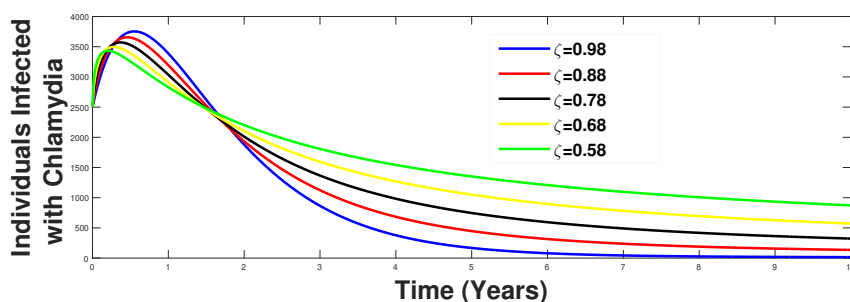
In this numerical simulation, we employ a Caputo-based predictor-corrector method derived from the Adams-Bashforth linear multistep method to solve the model described in model (1). The parameter values used in the simulation are listed in Table 2, unless otherwise specified.

We set the initial conditions for the variables as follows: $S_H(0) = 35,000,000$, $V_{CL}(0) = 3000$, $I_{CL}(0) = 3500$, $T_{CL}(0) = 3000$, $I_G(0) = 3000$, $T_G(0) = 3000$, and $I_{GCL}(0) = 3500$. These initial conditions are chosen arbitrarily based on the non-availability of data on the co-infection of Chlamydia and Gonorrhea study.

Table 2. Parameter values and corresponding references

Parameter	Values	Reference
ϵ_W	1.1	[9, 17]
ϵ_L	1.1	[9, 17]
μ	0.0122	[17]
β_C, β_G	1.1	[9, 17]
ω	0.5	[9]
γ	0.895	Assumed
τ	0.9	Assumed
δ_1	0.5	[15]
δ_2	0.05	Assumed
δ_3	0.05	Assumed
η_c	1.2	[17]
η_g	1.2	[17]
ξ_1, ξ_2	1.2	Assumed
ρ_1, ρ_2	0.9	Assumed
ρ	0.9	Assumed
Λ_H	596620.9	Assumed

We present the results of a numerical simulation of model (1) over a period of 10 years, using different fractional order values $\zeta = 0.98, 0.88, 0.78, 0.68, 0.58$. The simulation results for the different classes $I_{CL}(t)$, $I_G(t)$, and $I_{GCL}(t)$ are shown in Figs. (2), (3), and (8), respectively. The fractional order of the model is of high significance in modeling, as demonstrated by the simulation results. Fig. (2) shows that the population of people infected with Chlamydia initially decreases as the order increases, but after one and a half years, the trend reverses and remains uniform for the rest of the period. The same trend is observed for the population of infectious Gonorrhoea class as the order of the model is varied. Fig. (4) demonstrates the importance of vaccination in reducing the burden of Chlamydia. At a fractional order of $\zeta = 0.98$, an effective reduction of individuals in the class is achieved for the first four years, leading to the total eradication of people infected with Chlamydia when the vaccination is sustained afterwards. Fig. (5) shows that effective treatment of people infected with Chlamydia can also reduce the burden of the disease. At a fractional order of $\zeta = 0.78$, the desired result of reducing the burden of the disease is achieved in a shorter period than that required for vaccination. When individuals with dual infection are treated for Gonorrhoea, there is a corresponding reduction in the population of individuals in the Chlamydia class, as seen in Fig. (6). This is likely due to the use of similar antibiotics in treating some common STDs. Similarly, Fig. (7) shows that effective treatment of one STD can lead to the collapse of other similar diseases, whether detected at that point or not. Finally, Fig. (9) shows that increasing the treatment rate leads to a corresponding decrease in the population of infected Gonorrhoea patients, as expected.

**Figure 2.** Varying the fractional order and its effects on the dynamics of the infectious Chlamydia class

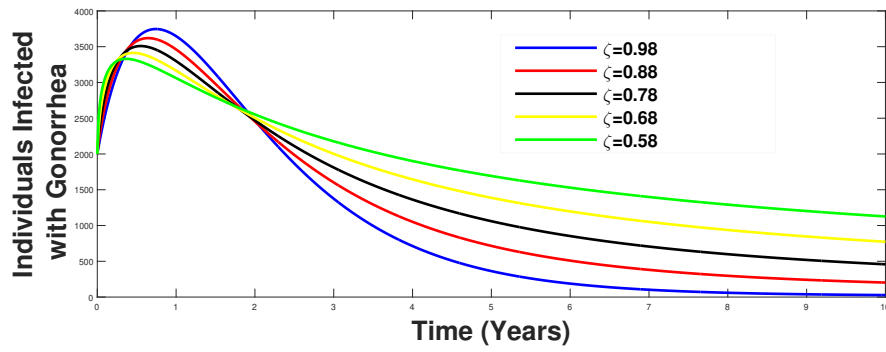


Figure 3. Varying the fractional order and its effects on the dynamics of the infectious Gonorrhoea class

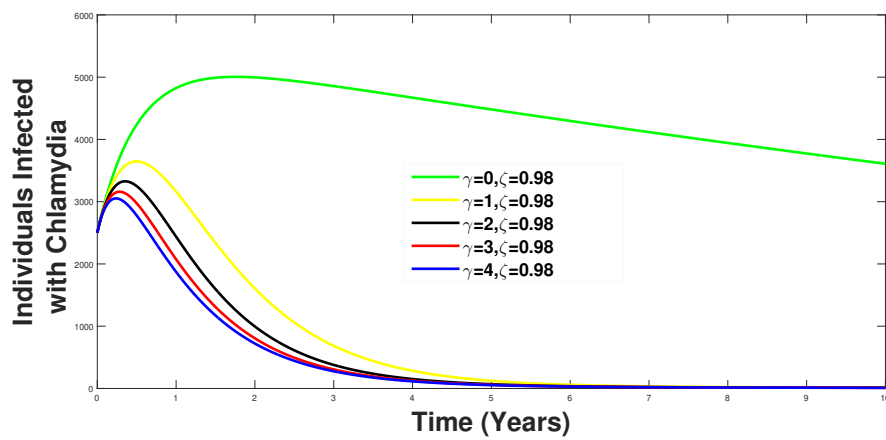


Figure 4. Effect of rate of vaccination on individuals infected with Chlamydia at $\zeta = 0.98$

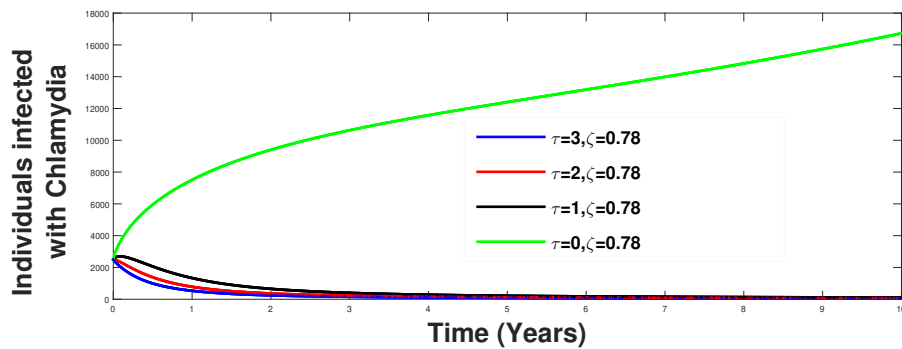


Figure 5. The effect of treatment rate on the infectious Chlamydia class $\zeta = 0.78$

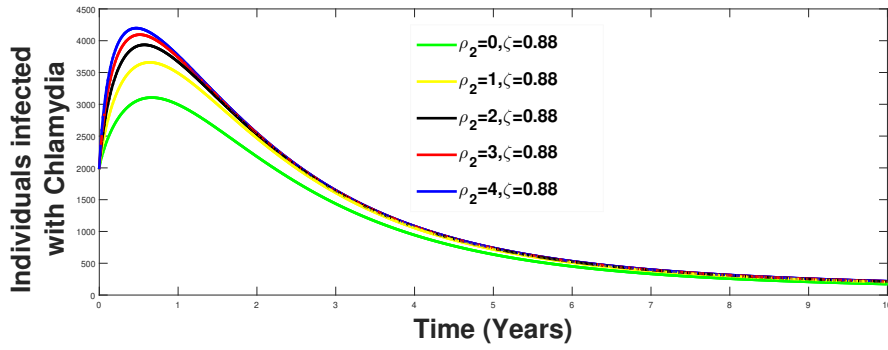


Figure 6. The effect of varying the rate at which dually infected individuals gets treated of Gonorrhea at $\zeta = 0.88$

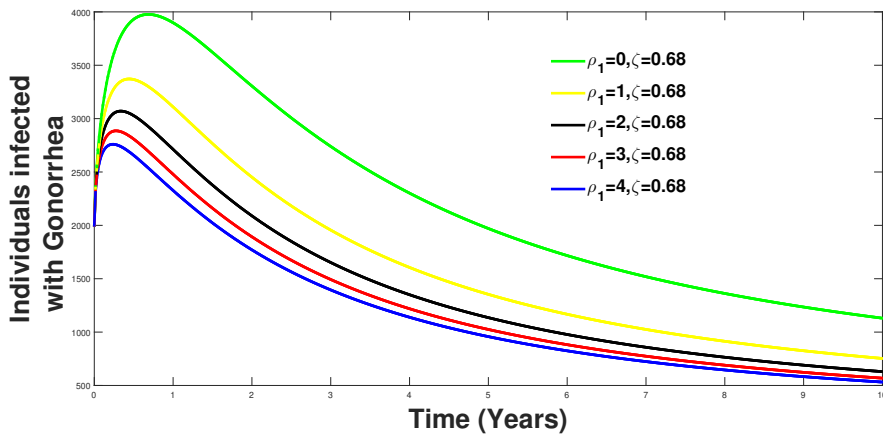


Figure 7. Varying the rate which dually infected individuals gets treated of Chlamydia

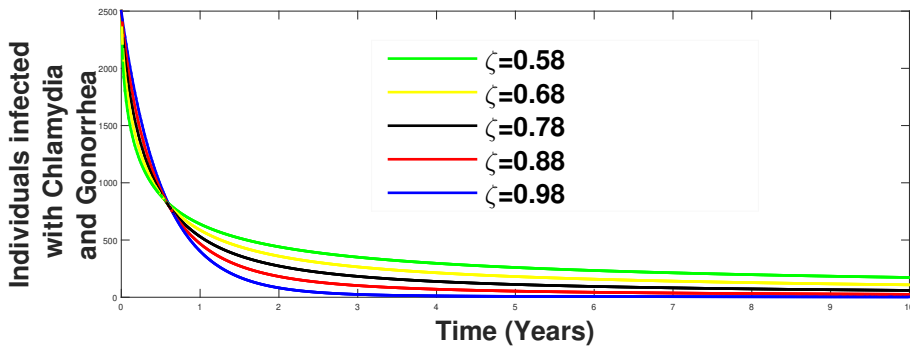


Figure 8. The effect of varying the fractional order of the dually infected individuals and its effects on the disease dynamics

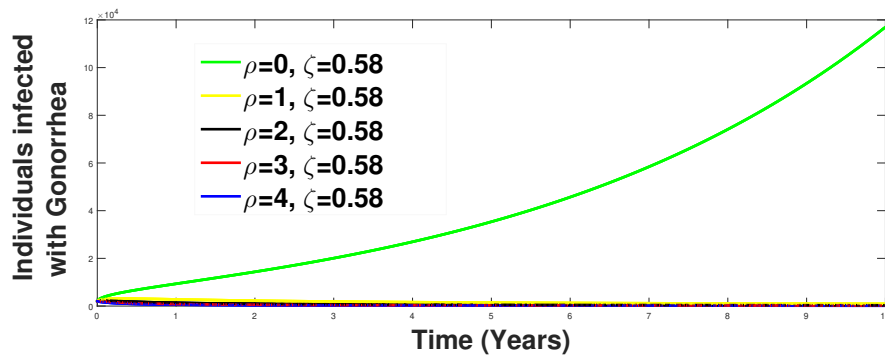


Figure 9. Varying the treatment rate of Gonorrhea and its effects on the Gonorrhea class

5 Conclusions

The results of the numerical simulation for model (1) are presented in Figs. (2)–(9), which show the dynamics of the different classes of infections over a 10-year period for varying fractional order values ζ . One important observation from Figs. (2) and (3) is that the populations of individuals infected with chlamydia and gonorrhea, respectively, decrease as the fractional order increases for the first year and a half, but then increase as the fractional order further increases. In contrast, the population of individuals who are co-infected with both chlamydia and gonorrhea decreases initially as the fractional order decreases, but increases thereafter.

Another key finding from the simulation is that increasing the vaccination rate leads to a decrease in the population of individuals infected with chlamydia, as shown in Fig. (4). On the other hand, varying the treatment rate for gonorrhea (Fig. (6)) and chlamydia (Fig. (7)) yields different outcomes depending on the fractional order. Furthermore, the results in Fig. (9) indicate that increasing the treatment rate for individuals infected with gonorrhea can reduce the burden of gonorrhea infection in the population of individuals with gonorrhea.

It is worth noting that the Caputo-based predictor-corrector method was used for the numerical simulation, and the Laplace transform was used to show that the model is bounded and positively invariant. The existence and uniqueness of the model were established using methods based on Banach and Schaefer's fixed point theorem. Additionally, the model was found to be Ulam-Hyers-Rassias stable.

Based on the results obtained from this study, we can conclude the following:

- * Effective treatment of individuals infected with both Chlamydia and Gonorrhea is crucial in achieving the desired outcome of reducing the burden of the diseases in a general sense.
- * Vaccination has been shown to play a significant role in the fight against the investigated diseases, and more efforts should be made in developing and administering vaccines if the long-term goal of eradicating the diseases is desired

These conclusions are based on the simulation results of the proposed fractional model of Chlamydia-Gonorrhea co-infection.

In summary, the results suggest that the effective treatment of individuals infected with both Chlamydia and Gonorrhea, coupled with vaccination programs, can significantly reduce the burden of the diseases. The findings of this study provide insights that can guide policymakers and health-care providers in developing and implementing effective strategies for controlling and managing Chlamydia-Gonorrhea co-infection. The results obtained from this study can aid in the development of more effective treatment strategies for this type of co-infection. Additionally, the methods used in this study can be applied to investigate the dynamics of other infectious

diseases modeled using fractional calculus. Overall, this paper contributes to the growing body of research on the application of fractional calculus in modeling infectious diseases, highlighting the importance of considering the fractional order in the modeling process.

Declarations

Ethical approval

The authors state that this research complies with ethical standards. This research does not involve either human participants or animals.

Consent for publication

Not applicable.

Conflicts of interest

The authors declare that they have no conflict of interest.

Data availability statement

Data availability is not applicable to this article as no new data were created or analysed in this study.

Author's contributions

U.B.O.: Conceptualization, Supervision, Project Administration, Formal Analysis, Resources, Visualization, Acquisition. N.I.: Formal Analysis, Investigation, Data Curation, Software, Validation, Writing-Original Draft, Writing-Review & Editing. B.B.: Methodology, Writing-Original Draft, Validation, Project Administration. All authors discussed the results and contributed to the final manuscript.

Acknowledgements

Not applicable.

References

- [1] Centers for Disease Control and Prevention (CDC). (2021). Chlamydia - CDC Fact Sheet (Detailed Version). Retrieved from <https://www.cdc.gov/std/chlamydia/stdfact-chlamydia-detailed.htm> (Accessed Date: 20.04.2023).
- [2] Centers for Disease Control and Prevention (CDC). (2021). Gonorrhea - CDC Fact Sheet (Detailed Version). Retrieved from <https://www.cdc.gov/std/gonorrhea/stdfact-gonorrhea-detailed.htm> (Accessed Date: 20.04.2023).
- [3] Centers for Disease Control and Prevention (CDC). (2016). STDs and HIV – CDC Fact Sheet. Retrieved from <https://www.cdc.gov/std/hiv/stdfact-std-hiv-detailed.htm> (Accessed Date: 20.04.2023).
- [4] Odionyenma, U.B., Omame, A., Ukanwoke, N.O. and Nometa, I. Optimal control of Chlamydia model with vaccination. *International Journal of Dynamics and Control*, 10, 332-348, (2022). [[CrossRef](#)]
- [5] Omame, A., Okuonghae, D., Umana, R.A. and Inyama, S.C. Analysis of a co-infection model for HPV-TB. *Applied Mathematical Modelling*, 77, 881-901, (2020). [[CrossRef](#)]
- [6] Omame, A., Okuonghae, D. and Inyama, S.C. A mathematical study of a model for HPV

- with two high-risk strains. In *Mathematical Modelling in Health, Social and Applied Sciences* (pp. 107-149). Springer, Singapore, Forum for Interdisciplinary Mathematics, (2020). [[CrossRef](#)]
- [7] Samanta, G.P. Mathematical analysis of a Chlamydia epidemic model with pulse vaccination strategy. *Acta Biotheoretica*, 63, 1-21, (2015). [[CrossRef](#)]
- [8] Sharomi, O. and Gumel, A.B. Mathematical study of a risk-structured two-group model for Chlamydia transmission dynamics. *Applied Mathematical Modelling*, 35(8), 3653-3673, (2011). [[CrossRef](#)]
- [9] Sharomi, O. and Gumel, A.B. Re-infection-induced backward bifurcation in the transmission dynamics of Chlamydia trachomatis. *Journal of Mathematical Analysis and Applications*, 356(1), 96-118, (2009). [[CrossRef](#)]
- [10] Hussien, S., Wachamo, D., Yohannes, Z. and Tadesse, E. Prevalence of Chlamydia trachomatis infection among reproductive age women in sub Saharan Africa: a systematic review and meta-analysis. *BMC Infectious Diseases*, 18, 596, (2018). [[CrossRef](#)]
- [11] Zhu, H., Shen, Z., Luo, H., Zhang, W. and Zhu, X. Chlamydia trachomatis infection-associated risk of cervical cancer: a meta-analysis. *Medicine*, 95(13), 1-10, (2016). [[CrossRef](#)]
- [12] Paba, P., Bonifacio, D., Bonito, L.D., Ombres, D., Favalli, C., Syrjänen, K. and Ciotti, M. Co-expression of HSV2 and Chlamydia trachomatis in HPV-positive cervical cancer and cervical intraepithelial neoplasia lesions is associated with aberrations in key intracellular pathways. *Intervirology*, 51(4), 230-234, (2008). [[CrossRef](#)]
- [13] Omede, B.I., Odionyenma, U.B., Ibrahim, A.A. and Bolaji B. Third wave of COVID-19: mathematical model with optimal control strategy for reducing the disease burden in Nigeria. *International Journal of Dynamics and Control*, 11, 411–427, (2023). [[CrossRef](#)]
- [14] Gopalkrishna, V., Aggarwal, N., Malhotra, V.L., Koranne, R.V., Mohan, V.P., Mittal, A. and Das, B.C. Chlamydia trachomatis and human papillomavirus infection in Indian women with sexually transmitted diseases and cervical precancerous and cancerous lesions. *Clinical Microbiology and Infection*, 6(2), 88-93, (2000). [[CrossRef](#)]
- [15] Omame, A., Nnanna, C.U. and Inyama, S.C. Optimal control and cost-effectiveness analysis of an HPV–Chlamydia trachomatis co-infection model. *Acta Biotheoretica*, 69, 185-223, (2021). [[CrossRef](#)]
- [16] Omame, A., Okuonghae, D., Nwafor, U.E. and Odionyenma, B.U. A co-infection model for HPV and syphilis with optimal control and cost-effectiveness analysis. *International Journal of Biomathematics*, 14(07), 2150050, (2021). [[CrossRef](#)]
- [17] Chukukere, E.C, Omame, A., Onyenegecha, C.P. and Inyama, S.C. Mathematical analysis of a model for Chlamydia and Gonorrhoea co-dynamics with optimal control. *Results in Physics*, 27, 104566, (2021). [[CrossRef](#)]
- [18] Omame, A., Abbas, M. and Onyenegecha, C.P. A fractional order model for the co-interaction of COVID-19 and Hepatitis B virus. *Results in Physics*, 37, 105498, (2022). [[CrossRef](#)]
- [19] Ullah, S., Khan, M.A., Farooq, M., Hammouch, Z. and Baleanu, D. A fractional model for the dynamics of tuberculosis infection using Caputo-Fabrizio derivative. *Discrete and Continuous Dynamical Systems Series S*, 13(3), 975-993, (2020). [[CrossRef](#)]
- [20] Thabet, S.T.M., Abdo, M.S. and Shah, K. Theoretical and numerical analysis for transmission dynamics of COVID-19 mathematical model involving Caputo–Fabrizio derivative. *Advances in Difference Equations*, 2021, 184, (2021). [[CrossRef](#)]
- [21] Joshi, H., Yavuz, M. and Stamova, I. Analysis of the disturbance effect in intracellular calcium

- dynamic on fibroblast cells with an exponential kernel law. *Bulletin of Biomathematics*, 1(1), 24-39, (2023). [[CrossRef](#)]
- [22] Yildiz, T.A., Jajarmi, A., Yildiz, B. and Baleanu, D. New aspects of time fractional optimal control problems within operators with nonsingular kernel. *Discrete and Continuous Dynamical Systems Series S*, 13(3), 407-428, (2020). [[CrossRef](#)]
- [23] Shah, K., Jarad, F. and Abdeljawad, T. On a nonlinear fractional order model of dengue fever disease under Caputo-Fabrizio derivative. *Alexandria Engineering Journal*, 59(4), 2305-2313, (2020). [[CrossRef](#)]
- [24] Dokuyucu, M.A., Celik, E., Bulut, H. and Baskonus, H.M. Cancer treatment model with the Caputo-Fabrizio fractional derivative. *The European Physical Journal Plus*, 133, 92, (2018). [[CrossRef](#)]
- [25] Atede, A.O., Omame, A. and Inyama, S.C. A fractional order vaccination model for COVID-19 incorporating environmental transmission: a case study using Nigerian data. *Bulletin of Biomathematics*, 1(1), 78-110, (2023). [[CrossRef](#)]
- [26] Omame, A., Nwajeri, U.K., Abbas, M. and Onyenegecha, C.P. AA fractional order control model for Diabetes and COVID-19 co-dynamics with Mittag-Leffler function. *Alexandria Engineering Journal*, 61(10), 7619-7635, (2022). [[CrossRef](#)]
- [27] Omame, A., Isah, M.E., Abbas, M., Abdel-Aty, A. and Onyenegecha, C.P. A fractional order model for Dual Variants of COVID-19 and HIV co-infection via Atangana-Baleanu derivative. *Alexandria Engineering Journal*, 61(12), 9715-9731, (2022). [[CrossRef](#)]
- [28] Evirgen, F., Uçar, E., Uçar, S. and Özdemir, N. Modelling influenza a disease dynamics under Caputo-Fabrizio fractional derivative with distinct contact rates. *Mathematical Modelling and Numerical Simulation with Applications*, 3(1), 58-72, (2023). [[CrossRef](#)]
- [29] Ogunrinde, R.B., Nwajeri, U.K., Fadugba, S.E., Ogunrinde, R.R. and Oshinubi, K.I. Dynamic model of COVID-19 and citizens reaction using fractional derivative. *Alexandria Engineering Journal*, 60(2), 2001-2012, (2021). [[CrossRef](#)]
- [30] Khan, M.A, Hammouch, Z. and Baleanu, D. Modeling the dynamics of hepatitis E via the Caputo-Fabrizio derivative. *Mathematical Modelling of Natural Phenomena*, 14(3), 311, (2019). [[CrossRef](#)]
- [31] Ucar, E., Ozdemir, N. and Altun, E. Fractional order model of immune cells influenced by cancer cells. *Mathematical Modelling of Natural Phenomena*, 14(3), 308, (2019). [[CrossRef](#)]
- [32] Sene, N. SIR epidemic model with Mittag-Leffler fractional derivative. *Chaos, Solitons & Fractals*, 137, 109833, (2020). [[CrossRef](#)]
- [33] Omame, A., Abbas, M. and Abdel-Aty, A.H. Assessing the impact of SARS-CoV-2 infection on the dynamics of dengue and HIV via fractional derivatives. *Chaos, Solitons & Fractals*, 162, 112427, (2022). [[CrossRef](#)]
- [34] Nwajeri, U.K., Omame, A. and Onyenegecha, C.P. Analysis of a fractional order model for HPV and CT co-infection. *Results in Physics*, 28, 104643, (2021). [[CrossRef](#)]
- [35] Nwajeri, U.K., Panle, A.B., Omame, A., Obi, M.C. and Onyenegecha, C.P. On the fractional order model for HPV and Syphilis using non-singular kernel. *Results in Physics*, 37, 10546, (2022). [[CrossRef](#)]
- [36] Omame, A., Abbas, M. and Onyenegecha, C.P. A fractional-order model for COVID-19 and tuberculosis co-infection using Atangana-Baleanu derivative. *Chaos, Solitons & Fractals*, 153, 111486, (2021). [[CrossRef](#)]

- [37] Sene, N. Theory and applications of new fractional-order chaotic system under Caputo operator. *An International Journal of Optimization and Control: Theories & Applications (IJOCTA)*, 12(1), 20–38, (2022). [[CrossRef](#)]
- [38] Veerasha, P., Yavuz, M. and Baishya, C. A computational approach for shallow water forced Korteweg–De Vries equation on critical flow over a hole with three fractional operators. *An International Journal of Optimization and Control: Theories & Applications (IJOCTA)*, 11(3), 52–67, (2021). [[CrossRef](#)]
- [39] Uçar, E., Uçar, S., Evirgen, F. and Özdemir, N. A fractional SAIDR model in the frame of Atangana–Baleanu derivative. *Fractal and Fractional*, 5(2), 32, (2021). [[CrossRef](#)]
- [40] Diouf, M. and Sene, N. Analysis of the financial chaotic model with the fractional derivative operator. *Complexity*, 2020, 9845031, (2020). [[CrossRef](#)]
- [41] Carpinteri, A. and Mainardi, F. *Fractals and Fractional Calculus in Continuum Mechanics*, (Vol. 378). Springer-Verlag Wien GmbH: New York, (1997). [[CrossRef](#)]
- [42] Liu, K., Feckan, M. and Wang, J. Hyers–Ulam stability and existence of solutions to the generalized Liouville–Caputo fractional differential equations. *Symmetry*, 12(6), 955, (2020). [[CrossRef](#)]
- [43] Van den Driessche, P. and Watmough, J. Reproduction numbers and sub-threshold endemic equilibria for compartmental models of disease transmission. *Mathematical Biosciences*, 180(1-2), 29-48, (2002). [[CrossRef](#)]
- [44] Castillo-Chavez, C., Feng, Z. and Huang, W. On the computation of R_0 and its role on global stability. In *Mathematical Approaches for Emerging and Reemerging Infectious Diseases: An Introduction*, (vol. 125), pp. 229–250. (Minneapolis, MN, 1999), Springer: New York, (2002). [[CrossRef](#)]
- [45] Diethelm, K. and Freed, A.D. The FracPECE subroutine for the numerical solution of differential equations of fractional order. *Forschung und Wissenschaftliches Rechnen*, 1999, 57-71, (1998).

Mathematical Modelling and Numerical Simulation with Applications (MMNSA)
(<https://dergipark.org.tr/en/pub/mmnsa>)



Copyright: © 2023 by the authors. This work is licensed under a Creative Commons Attribution 4.0 (CC BY) International License. The authors retain ownership of the copyright for their article, but they allow anyone to download, reuse, reprint, modify, distribute, and/or copy articles in MMNSA, so long as the original authors and source are credited. To see the complete license contents, please visit (<http://creativecommons.org/licenses/by/4.0/>).

How to cite this article: Odionyenma, U.B., Ikenna, N. & Bolaji, B. (2023). Analysis of a model to control the co-dynamics of Chlamydia and Gonorrhoea using Caputo fractional derivative. *Mathematical Modelling and Numerical Simulation with Applications*, 3(2), 111-140. <https://doi.org/10.53391/mmnsa.1320175>



RESEARCH PAPER

Generative adversarial network for load data generation: Türkiye energy market case

Bilgi Yilmaz  ^{1,2,*} ‡

¹Department of Mathematics, Kaiserslautern Technical University, Kaiserslautern, Germany,

²Department of Mathematics, Faculty of Science, Kahramanmaraş Sutcu Imam University, Türkiye

*Corresponding Author

‡yilmazb@rhrk.uni-kl.de (Bilgi Yilmaz)

Abstract

Load modeling is crucial in improving energy efficiency and saving energy sources. In the last decade, machine learning has become favored and has demonstrated exceptional performance in load modeling. However, their implementation heavily relies on the quality and quantity of available data. Gathering sufficient high-quality data is time-consuming and extremely expensive. Therefore, generative adversarial networks (GANs) have shown their prospect of generating synthetic data, which can solve the data shortage problem. This study proposes GAN-based models (RCGAN, TimeGAN, CWGAN, and RCWGAN) to generate synthetic load data. It focuses on Türkiye's electricity load and generates realistic synthetic load data. The educated synthetic load data can reduce prediction errors in load when combined with recorded data and enhance risk management calculations.

Keywords: Load in Türkiye energy market; generative adversarial networks; synthetic data generation; unsupervised learning; RCGAN; TimeGAN; CWGAN; RCWGAN

AMS 2020 Classification: 68T07; 82C32; 68T05

1 Introduction

A *smart grid* is an electricity distribution network incorporating information and communication technologies to improve energy efficiency. It allows for the real-time exchange of data between electricity suppliers and consumers, which enables suppliers to forecast electricity demand based on current energy consumption and user profiles. This feature enables energy suppliers to optimize electricity efficiency by providing accurate load modeling, resulting in a more efficient power grid [1].

In the context of smart grids, accurate electricity demand forecasting is crucial for energy suppliers to avoid financial losses and system troubles, e.g., drops in frequency and blackouts. However,

obtaining an extensive and high-quality electricity dataset is challenging and expensive. Although electricity grid models are known, data is short as a consequence of privacy concerns, which restricts the researchers' access to datasets and limits the development and application of further load prediction models.

Generating synthetic data that accurately represents real data's statistical behavior and characteristics can help address subjects connected to sensitive data's quantity, quality, and privacy. By generating synthetic data that mimics the patterns and trends of real data, it is possible to provide researchers and companies with a valuable resource for understanding the distribution of the original data while also enabling efficient data storage, data augmentation, system testing, and data disclosure. Synthetic data generation can also help mitigate concerns around data privacy, as it can provide a substitute for sensitive or confidential data that is not accessible to third parties. This study focuses explicitly on Generative Adversarial Networks (GANs) for generating synthetic data regarding their implementation performance and flexibility in mirroring historical data. GANs have successfully generated and manipulated images and natural languages, as demonstrated by various studies [2, 3, 4, 5]. As a result, GANs have become a prominent method for synthetic data generation.

GANs are powerful generative models that can assemble new samples having similar distributional properties to the real data, making them useful for data augmentation [6]. While initially developed for image processing and computer vision, GANs have garnered significant interest and advanced in various research fields [7]. GANs also demonstrated favorable outcomes in generating sequential data (e.g., music, medical data, and finance). Therefore, this study focuses on applying GANs to sequential data, specifically generating synthetic load data for Türkiye energy market.

There are two primary strategies for applying GANs to electricity consumption data forecasting. The first strategy uses a typical GAN architecture in generating synthetic load data. The performance is evaluated concerning the divergence or convergence of synthetic data to real data. The second strategy involves using more complex GAN architectures to generate synthetic electricity consumption data and combining it with real data to expand and improve real load data. The first approach is limited to scenario generation. It produces load profiles lacking precision, while the second approach is data augmentation, which is highly influential but must fully illustrate the capabilities of GANs. Therefore, this study focuses on the first strategy of synthetic data generation using GANs to produce hourly electricity consumption records.

Although usually, studies suggest using Long Short-Term Memory (LSTM) in GANs, this study avoids utilizing it to decrease the computational cost of training and overfitting problems. Instead, the study uses Recurrent Neural Network (RNN). More specifically, it uses the GANs called Recurrent Conditional GAN (RCGAN) [8], Time-Series GAN (TimeGAN) [9], Conditional Wasserstein GAN (CWGAN) [2], and Recurrent Conditional Wasserstein GAN (RCWGAN) as in [10].

The remaining part of the study is systematized as follows: Section 2 briefly reviews the literature on GANs. Section 3 presents an overview of the GANs used in this study without delving into technical facts. Section 4 introduces Türkiye's load data and includes exploratory data analysis and synthetic data generation using the selected GANs. Section 5 concludes the study.

2 Literature review

The concept of GANs was submitted in the paper by [11] and quickly gained traction in many research fields, such as 3D object generation [12], electronic health record generation [8], image processing [13] and generation [11, 14], face detection [15], audio synthesis [16, 17] natural language processing [18], traffic controlling [19], energy market modeling [10], and stock market modeling [20]. However, training GANs are challenging since they generally suffer from missing

modes problem or model collapse, where the generated samples lack variety and only cover some regions of the space. Another common issue is vanishing gradients that can stop GANs training from converging to an optimal state. Dealing with these problems has gained significant attention in GAN research, and various approaches have been proposed to mitigate them.

Consequently, many alternative GANs are developed from empirical and mathematical perspectives to solve such problems. For instance, the study of [2] is the first study that extends the GANs by comparing various distance measures and suggests using the Wasserstein-1-metric, which leads to the development of WGAN. Later, [21] proposed the Least Squares GANs (LSGANs) that adopt a least-squares loss function for the discriminator to overcome the vanishing gradients problem. [22] also proposed a conditional model that extends the original GAN framework by incorporating additional information such as labels, tags, or attributes. This information is provided to the GAN framework through an additional input layer. However, it is outside the content of this study to provide a complete review of such approaches. Therefore, the study covers only the studies focusing on time series data since it is interested in generating time series data, and it can draw some inspiration from applying GANs in financial and electricity markets.

Various GANs have been proposed to generate financial and energy time series data. Financial time series are more challenging to model than other time series because of their high volatility and unexpected market behavior. Therefore, alternative GAN models have been proposed to overcome these challenges. For instance, one of the earliest works presented by [20] offers QuantGANs for financial time series data generation. The QuantGANs utilizes temporal convolutional networks to capture long-range dependencies and can generate realistic stock price simulations employing a data-driven neural network. The QuantGANs can capture the temporal dependence of financial time series, including volatility clustering. [23] proposed a variant of Conditional GANs (cGANs), called Stock-GAN, to generate order flow in the limit order book. The authors showed that cGANs could generate a realistic and high-fidelity stock market. Similarly, [24] and [25] generated transaction prices in a stock market by using cGAN and illustrated the accuracy of GANs in stock markets.

Recently, the use of GANs in electricity markets has gained significant attention. [10] utilized RCGAN, TimeGAN, CWGAN, and RCWGAN for univariate electricity consumption time series data generation. In their empirical analysis, the authors showed that all four GANs could generate realistic electricity consumption for an individual. Furthermore, they showed the GANs' stability and no vanishing gradient. [26] employed Deep Convolutional GANs (DCGANs) to generate power profile scenarios for wind and solar power plants and energy consumption data. They show that GANs captured the patterns of renewable energy production in both temporal and spatial dimensions under the assumption of a large number of correlated resources. [27] utilized cWGAN to generate synthetic energy consumption data and generated realistic energy consumption data by given labels as a condition imitating real data distribution. [28] used deep learning GANs in generating electricity consumption and fault diagnosis to develop smart management tools for heating, ventilation, and air conditioning (HVAC). The authors showed that deep learning GAN can help to increase the fault diagnosis accuracy in electricity consumption.

[29] proposed GANs as a novel method to generate realistic electrical load profiles of buildings. They showed that the load profiles generated by GANs could mirror the general load trend and the random variations of the actual loads in buildings. Furthermore, they suggested that GANs detect changes in load profiles, anonymize smart meter data, and support grid management applications. [30] utilized GANs to quantify the uncertainties related to the climate and human-system-driven in the energy market. They revealed that climate-driven uncertainties in human systems cause higher fluctuations in load profiles. [31] also aimed to build scenarios by embedding GANs and understanding the stochastic and dynamic characteristics of renewable energy re-

sources. They demonstrated that GANs achieved the controllable generation of renewable energy generation scenarios covering various statistical characteristics and revealed new patterns. [32] benefited GANs to generate scalable and realistic energy demand. The authors claimed that GANs are promising for generating realistic energy demand data. [33] offer GANs a potential approach for predicting large-scale building energy consumption to manage grid operations. To this end, [33] used various GANs (the original GAN, cGAN, SGAN, InfoGAN, and ACGAN) to predict large-scale building energy consumption. The authors claimed that the success of the GANs highly depends on the data size. Further, they claim that SGAN and InfoGAN are unsuitable for large-scale building electricity consumption prediction since these two GANs do not control the number of generated building samples for different building types.

Machine learning applications in Türkiye's energy market are not a new concept, and there are remarkable works in the literature. For instance, [34] used artificial neural networks (ANN) to predict and forecast energy consumption and make correct investments in Türkiye by considering economic indicators (gross national product—GNP and gross domestic product—GDP) and population increase as independent variables. [35] used ANN to forecast electricity consumption in various sectors. Similarly, [36] model Türkiye's energy consumption using ANN and regression analyses to forecast projections by considering explanatory variables, such as socio-economic and demographic factors (gross domestic product (GDP), import and export, population, and employment). [37] and [38] developed acceptable methods based on the ANN model that uses GDP, population, imports, exports, building area, and number of vehicles for estimating Türkiye's future energy demand while [39] developed forecasting models relying on ANN to predict the energy consumption in Türkiye's transportation sector. However, there is no study utilizing GANs for Türkiye's energy market.

3 Generative adversarial networks

Training GANs are challenging since they generally suffer from missing modes problem or model collapse, where the generated samples lack variety and only cover some regions of the space. Another common issue is vanishing gradients that can stop GANs training from converging to an optimal state. Dealing with these problems has gained significant attention in GAN research, and various approaches have been proposed to mitigate them. However, it is outside the content of this study to provide a complete review of such approaches.

As [11] introduced, GANs belong to the family of unsupervised learning algorithms. They can learn dense representations of input datasets and are utilized as generative models. The superiority of GANs is the ability to generate new samples having (nearly) the same distribution as the training dataset. They contain two competing neural networks, Generator (G) and Discriminator (D). Therefore, the training of GANs relies on a zero-sum game. G directly produces samples from a well-known distribution (e.g., normal and uniform distributions) as input (latent vector z), and D attempts to distinguish between samples drawn from training and generated data. The discriminator output ($D(x)$) corresponds to the probability that a sample belongs to the distribution underlying the training data. On the other hand, the generator output ($G(z)$) is a sample from the learned distribution. The competition between G and D is formulated as

$$\min_G \max_D V(D, G) = \min_G \max_D \left(\mathbb{E}_{x \sim \mu} \left[\log \left(D(x) \right) \right] + \mathbb{E}_{z \sim \gamma} \left[\log \left(1 - D(G(z)) \right) \right] \right),$$

where $D(x) : \mathbb{R}^n \mapsto [0, 1]$ and $G(z) : \mathbb{R}^d \mapsto \mathbb{R}^n$, where G is the generator function that takes random samples $z \in \mathbb{R}^d$ from a predefined distribution γ (usually a Gaussian distribution) and generates samples $G(z)$ [40, 41]. This linear function illustrates the adversarial competition

between the generator and discriminator. Here, the discriminator outputs a binary variable, where $D(x) = 1$ for real samples and $D(x) = 0$ for generated samples, while the generator outputs a synthetic sample vector.

It is important to note that when it comes to generating or predicting time series data, it is more significant to determine the correct conditional distribution rather than learning the joint distribution. This is because, in predictive modeling, we are concerned with identifying the conditional distributions of the future time series $x_{future} = x_{t+1:t+q}$, which refers to the following q values given the past p observations of the time series $x_{past} = x_{t-p+1:t}$ at time t (for more information, see [42].)

The GANs considered in this study are characterized by the selection of their respective loss functions for the discriminator and generator.

Recurrent Conditional GAN (RCGAN)

The RCGAN shares a similar architecture with the traditional GAN but with a modification where both the generator and discriminator are replaced with recurrent neural networks (RNNs). This change enables the RCGAN to generate sequence data dependent on specific conditional inputs and can produce realistic outputs.

Let $RNN(X)$ be the vector consisting of T outputs from an RNN that receives a sequence of T vectors $\{x_t\}_{t=1}^T$ ($x_t \in \mathbb{R}^d$), and let $CE(\mathbf{a}, \mathbf{b})$ denote the average cross-entropy between the sequences \mathbf{a} and \mathbf{b} . Then, according to [8], the discriminator and generator loss of $\mathbf{X}_n, \mathbf{y}_n$, where $\mathbf{X}_n \in \mathbb{R}^{T \times d}$ and $\mathbf{y}_n \in \{0, 1\}^T$, can be expressed as

$$\begin{aligned} D_{loss}(\mathbf{X}_n, \mathbf{y}_n) &= -CE(RNN_D(\mathbf{X}_n), \mathbf{y}_n), \\ G_{loss}(Z_n) &= D_{loss}(RNN_G(Z_n), \mathbf{1}) = -CE(RNN_D(RNN_G(Z_n)), \mathbf{1}), \end{aligned}$$

where \mathbf{y}_n is a vector consisting of ones if the sequence is real and zeros if it is fake. Z_n is a sequence of T points drawn from the latent space \mathbf{Z} , which is typically a m -dimensional Gaussian distribution. Therefore, Z_n is a matrix with dimensions $T \times m$. The vector $\mathbf{1}$ represents the decision of the discriminator accepting a given sequence as real data. During each training step, the discriminator uses both real and fake sequences.

Time-series GAN (TimeGAN)

TimeGAN was initially introduced in the work by [9]. This approach focuses on datasets that contain both static and temporal features. Static features remain constant and unchanging over time (such as gender), while temporal features change and are updated over time.

The static and temporal features can be represented using the vectors \mathcal{S} and \mathcal{X} , respectively. We can also assign specific values to random vectors $\mathbf{S} \in \mathcal{S}$ and $\mathbf{X} \in \mathcal{X}$, represented by s and x , respectively. Let us consider tuples $\mathbf{S}, \mathbf{X}_{1:T}$, where the joint distribution is denoted as p , and the length T of each sequence is also a random variable. In the training data, we can index individual samples using $n \in 1, \dots, N$, and denote the training dataset as $\mathcal{D} = (s_n, x\{n, 1 : T_n\})_{n=1}^N$.

The objective is to find the density $\hat{p}(\mathbf{S}, X_{1:T})$ that satisfactorily approximates the real data density $p(\mathbf{S}, X_{1:T})$ using the training dataset \mathcal{D} . However, achieving this task may require more work in the traditional GAN framework. To address this issue, [9] suggests using an autoregressive decomposition of $p((\mathbf{S}), \mathbf{X}_{1:T}) = p(\mathbf{S})\prod p(\mathbf{X}_t | \mathbf{S}, \mathbf{X}_{1:t-1})$ to concentrate on the additional information given as conditionals.

TimeGAN is distinct from traditional GANs in that it comprises four neural network components: two autoencoding components, namely the embedding and recovery functions, and two adversar-

ial components, namely the generator and discriminator. The main concept behind TimeGAN is that the autoencoding and adversarial components are trained jointly. Consequently, TimeGAN can simultaneously learn how to encode features, generate replicas, and iterate across time. The embedding network creates the latent space, while the adversarial network operates within this space. By means of a supervised loss, the latent dynamics of both empirical and generated data are synchronized.

Conditional Wasserstein GAN (CWGAN) and Recurrent Condition Wasserstein GAN (RCWGAN)

The WGAN was first presented in [2] as a solution to address the issues of mode collapse and vanishing gradient in traditional GANs. Instead of optimizing the traditional GAN loss, which is known to be prone to these issues, the WGAN optimizes the Wasserstein-1 distance. However, calculating the exact Wasserstein-1 distance is often impractical, so instead, the objective function is altered to approximate the Wasserstein-1 distance as

$$\min_G \max_D \mathbb{E}_{x \sim p_{data}} [D(x)] - \mathbb{E}_{z \sim p_z} [D(G(z))].$$

If D satisfies a Lipschitz constraint with a constant k , then it can be shown that the Wasserstein-1 distance is equivalent to the supremum of the output difference of D on pairs of inputs. The WGAN uses weight clipping to enforce the Lipschitz constraint, which restricts the weights of D to a compact interval such as $[-c, c]$ where c is a small positive value (e.g., 0.01). However, this technique can limit the capacity of the discriminator. It may cause the weights to converge to the endpoints of the interval, leading to gradient issues like vanishing or exploding gradients.

The WGAN-GP method is an improvement over the WGAN, and it addresses the drawbacks of weight-clipping by using a gradient penalty technique. Weight-clipping is replaced with soft enforcement of the Lipschitz constraint through a penalty on the discriminator. This penalty is based on a differentiable function being 1-Lipschitz if its gradients have a norm of at most 1 everywhere. Therefore, the new objective of the GAN is expressed as

$$\min_G \max_D \mathbb{E}_{x \sim p_{data}} [D(x)] - \mathbb{E}_{z \sim p_z} [D(G(z))] - \lambda \mathbb{E}_{\hat{x} \sim p_{\hat{x}}} [\|\nabla_{(\hat{x})} D(\hat{x})\|_2 - 1]^2,$$

where λ is the penalty coefficient.

The CWGAN is an extension of WGAN-GP that incorporates extra information into the model. This leads to a modified optimization problem that is given by

$$\min_G \max_D \mathbb{E}_{x \sim p_{data}} [D(x | y)] - \mathbb{E}_{z \sim p_z} [D(G(z | y))] - \lambda \mathbb{E}_{\hat{x} \sim p_{\hat{x}}} [(\|\nabla_{\hat{x}} D(\hat{x} | y)\|_2 - 1)^2],$$

where y is the vector of additional information.

The RCWGAN architecture is similar to that of the CWGAN, but instead of using conventional neural networks as the generator and discriminator, Recurrent Neural Networks (RNNs) are employed.

4 Empirical analysis

Data and its stylized facts

The study uses the load data from Türkiye gathered from Epias¹ in its empirical analysis. The data consists of seven years of hourly load in Türkiye's energy market. The hourly load profile data over the period 01.01.2016-31.12.2022 is visualized in Figure 1. The figure shows that the load data contains inherent patterns that can be effectively leveraged through machine-learning techniques for modeling purposes. The load has a strong seasonality and a slightly increasing trend. The figure reveals a significant decrease in electricity consumption in Türkiye in the first and second quarters compared to other years. The decline in electricity demand can be attributed to several factors, such as the interruption of production in plants, reduced work hours resulting from restrictions, and the implementation of lockdown measures in cities. While climatic conditions and industrial activities commonly influence fluctuations in total electricity demand, these regular variations cannot account for the significant decrease observed. [43] explains the sharp decline in electricity demand as a direct consequence of the crisis caused by COVID-19 pandemic, clearly highlighting the impact of the prevailing pandemic conditions. Table 1 summarizes the descriptive

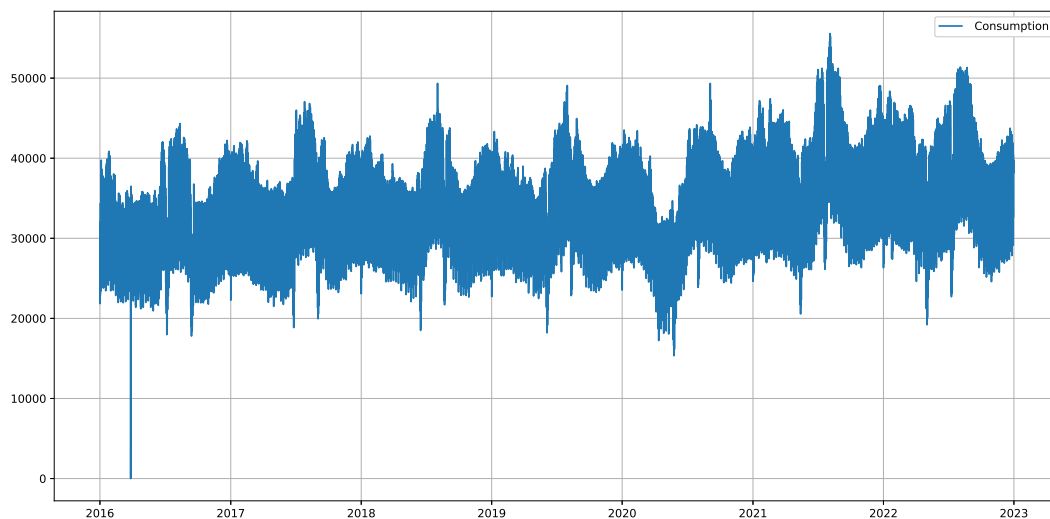


Figure 1. Visualization of load in Türkiye energy market (2016-01-01-2022-12-31)

statistics of hourly load in Türkiye for the considered period. The number of observations is 61345. The average load and Standard Deviation (SD) of load are approximately 34053.14 MWh and 5581.85 MWh in Türkiye's energy market. The SD indicates significant variability in load levels across the considered period. The minimum load is 0 units, which could be an error in the data. The 25% quantile of the observations has a load level below 29875.22 MWh representing the first quartile of the load distribution. 50% of the observations have a load level below 33878.73 MWh. It represents the median of the load data distribution. 75% of the observations have a load level below 38059.42 MWh, which represents the third quartile of the load data distribution.

1 <https://www.epias.com.tr/>

The maximum load is 55575.02 MWh could also be an outlier or a peak value in the investigated period.

Table 1. Descriptive statistics of load in Türkiye energy market

	Consumption
count	61345.000000
mean	34053.142402
std	5581.846170
min	0.000000
25%	29875.220000
50%	33878.730000
75%	38059.420000
max	55575.020000

Figure 2 presents the average daily load profile over seven years, 01.01.2016-31.12.2022. The figure shows the variation in electricity consumption over daily, weekly, monthly, and yearly. The figures are arranged sequentially starting from 2016 such that each row represents a specific year; the top figure corresponds to daily electricity consumption in 2016, the second figure from the top illustrates daily electricity consumption in 2017, and finally, the bottom figure presents daily electricity consumption in 2022. The seven rows in each year are days of the week, Monday through Sunday, and lines separate months.

In Figure 2, each cell corresponds to a calendar year day. The color intensity of the cells in the heatmap represents the varying electricity consumption levels across days. The lighter shades indicate higher electricity consumption, while darker shades represent lower electricity consumption. By analyzing this heatmap, we can observe patterns and trends in electricity usage throughout the years. The heatmap helps us to identify peak periods of electricity consumption, such as during weekdays when industrial and commercial activities are at their highest and lower periods during weekends or holidays when there is reduced demand. Such a visualization assists in understanding energy consumption patterns, identifying potential areas for energy conservation, and optimizing electricity distribution and resource planning strategies. For instance, we can detect certain days of the week or times of the year when the load tends to be higher or lower than average. Figure 2 also reveals a significant change in the load patterns over time, such as an increase in demand in August due to changes in the climate. It also reveals a significant decrease in the electricity demand during the weekends and public holidays.

Figure 3 contains distributions of yearly, daily, and monthly electricity consumption data. It provides a visual representation of the distribution of electricity consumption across different periods. The first row illustrates the yearly electricity consumption distributions. It shows the distribution of electricity consumption across each year independently. The box in the middle of the plot represents the interquartile range (IQR) of electricity consumption data, with the median value marked as a line in the box. The whiskers extending from the box represent the range of the data, excluding any outliers. The second row illustrates the distributional properties of electricity consumption in days of the week. It shows the distribution of electricity consumption across each weekday, with the x-axis representing the day of the week and the y-axis representing the electricity consumption level. It reveals any significant change in the electricity consumption on the business days and a slight decrease during the weekends. The third row shows the distributions of electricity consumption for months of the year. It shows that there is an increase in electricity consumption during summers, as in Figure 2, which is most probably due to the cooling needs in the summer. All three figures show that there are outliers in the data indicating

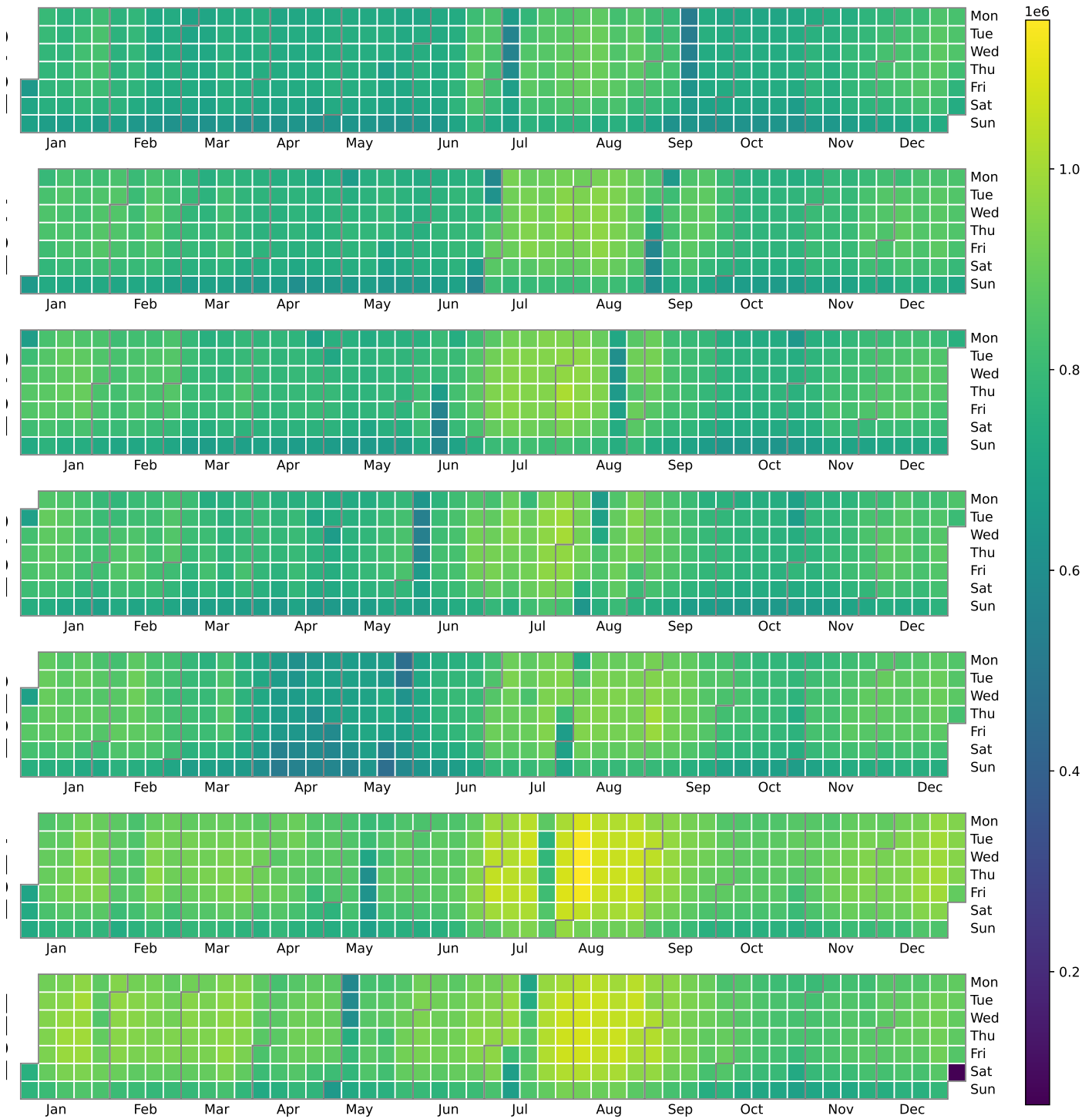


Figure 2. Daily electricity consumption behavior in Türkiye energy market (2016.01.01-2022.12.31)

unusual electricity consumption levels that should be investigated further. In contrast, patterns in the data could reveal important insights into energy usage.

Data preprocessing

In standard modeling and machine learning applications, deseasonalizing the data may be necessary to remove the effects of seasonality. However, deseasonalizing can make it difficult for the GAN to learn the underlying patterns and generate realistic samples since seasonality is an

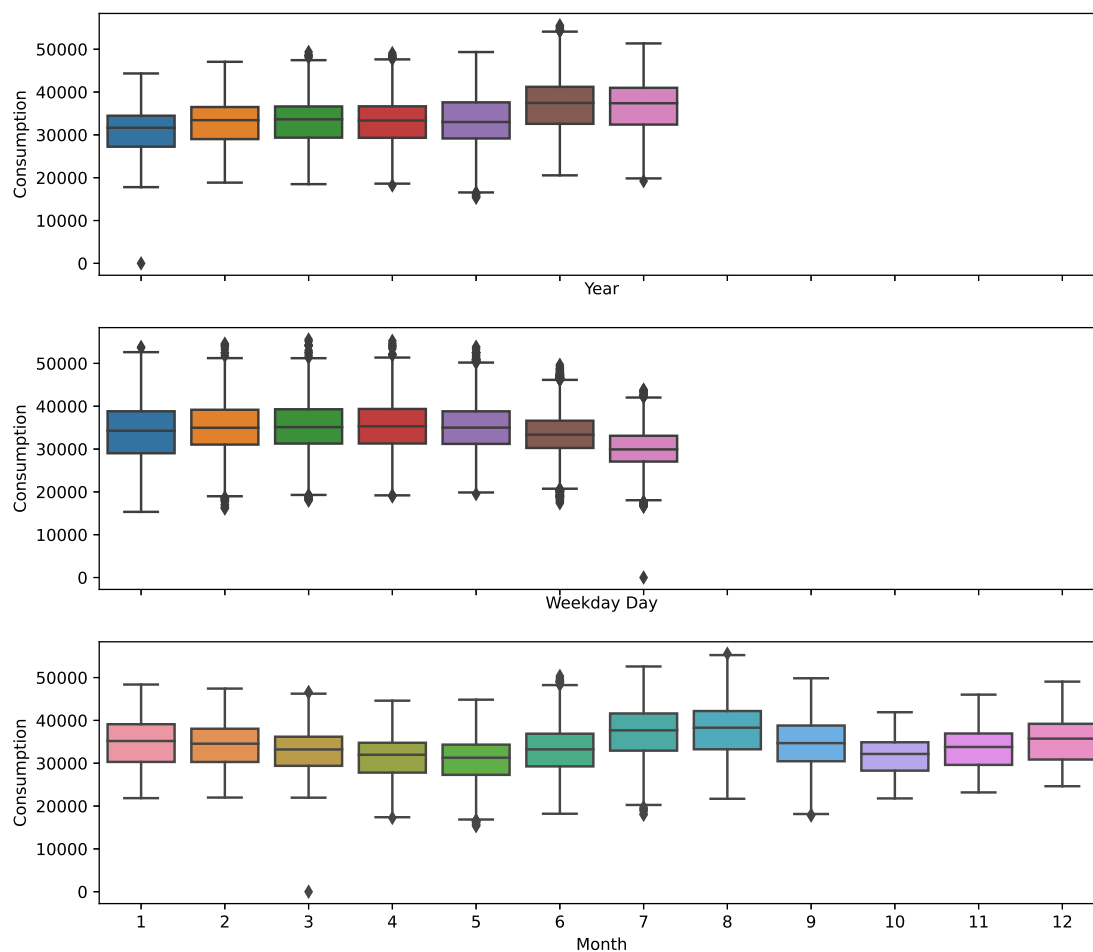


Figure 3. Statistical distribution of load in Türkiye energy market (2016.01.01-2022.12.31)

essential feature of the data we want to preserve. Hence, the data is preprocessed using robust scaling. This scaling method uses the interquartile range. Therefore, it is a robust scaling method for outliers. It has a formula given as

$$y_i = \frac{x_i - Q_{median}(x)}{Q_3(x) - Q_1(x)},$$

where Q_1 and Q_3 correspond to the 1st quartile and 3rd quartile, i.e., in between 25th quantile and 75th quantile range, respectively. Consequently, it removes the median and scales the data between Q_1 and Q_3 .

Table 2 provides descriptive load statistics after the preprocessing. The length of the training data decreased to 8017. As it is clear, the number of data points is decreased significantly. Here, the study uses only load data in 2017 for the training since the load is quite regular and identical in a classical calendar year (see Figures 2 and 3). After scaling the data, the mean value of -0.045 suggests that the variable has a slightly negative skew, although the value is close to zero. The

standard deviation of 0.677 indicates that the variable has moderate variability. The minimum value of -1.983 and maximum value of 1.864 show the range of load values, with values falling between these two extremes. The quartile values indicate the distribution across the dataset, with the median (50^{th} percentile) value of 0.000 falling at the center of the distribution.

Table 2. The descriptive statistics after preprocessing load

	Preprocessed load
count	8017.000
mean	-0.045
std	0.677
min	-1.983
25%	-0.595
50%	0.000
75%	0.405
max	1.864

Experimental studies

The study fixed time series parameters p and q as 4 for the CWGAN and 3 for the remaining GANs to learn the conditional distribution. The discriminators utilize the conditioning time series $x_{t-p+1:t}$ as inputs to generate the part of time series $x_{t+1:t+q}$, i.e., it uses a rolling window size $p + q = 8$ for the CWGAN and $p + q = 6$ for the others. It optimizes GANs algorithms for a total of 1000 generator weight updates. It utilizes the Adam optimizer [44] with parameters $\beta_1 = 0$ and $\beta_2 = 0.9$ to optimize neural network weights in the generator and discriminator and sets the learning rates to 0.001. In the RCGAN and TimeGAN cases, it applies two time-scale updates (TTUR) [45] and sets the learning rate to 0.003. Further, it updates discriminator weights twice per generator weight update to improve stability. The number of epochs operated is 1.000, with a batch size of 200 for all GANs. In the empirical performances, the study uses the Pytorch library [46] to build the GANs. It supplies high-level building blocks for designing deep learning models. Pytorch is a symbolic tensor manipulation framework alternative to TensorFlow.

Figure 4 shows the empirical distributional properties of the GANs and the real data to compare the distributions. The figure reveals a close match between real and synthetic load data distributions. All GANs have relatively close means, skewness, and kurtosis values. The histograms of real and synthetic datasets and their skewness and kurtosis statistics are presented in the figure to measure symmetry, tail behaviors, and changes in their auto-correlation. The histograms in the first column illustrate that the distribution of hourly load from synthetic load data (orange) is nearly equivalent to the real load data (blue). Only the RCGAN has positive skewness statistics, while the remaining GANs have negative skewness statistics, which is also positive for the real data.

In contrast, the kurtosis statistics are all positive for the GANs and real data. The RCGAN has the closes kurtosis statistics (-0.52) to the real data kurtosis statistics (-0.53) while the TimeGAN kurtosis statistics (-0.16) has a more considerable distance. Consequently, the TimeGAN is more peak than the real data. Furthermore, histograms of the log values presented in Figure 4 reveal some discrepancies in the tails of TimeGAN. The CWGAN and RCWGAN are better than the other two GANs in generating low loads, while the TimeGAN is the worst at generating low and high loads. The RCGAN, on the other hand, is the best at generating high load. The auto-correlations of all the GANs and real data are relatively close. While there are some differences in the skewness and kurtosis statistics, the synthetic datasets' distributional behaviors are nearly identical to the real data distribution.

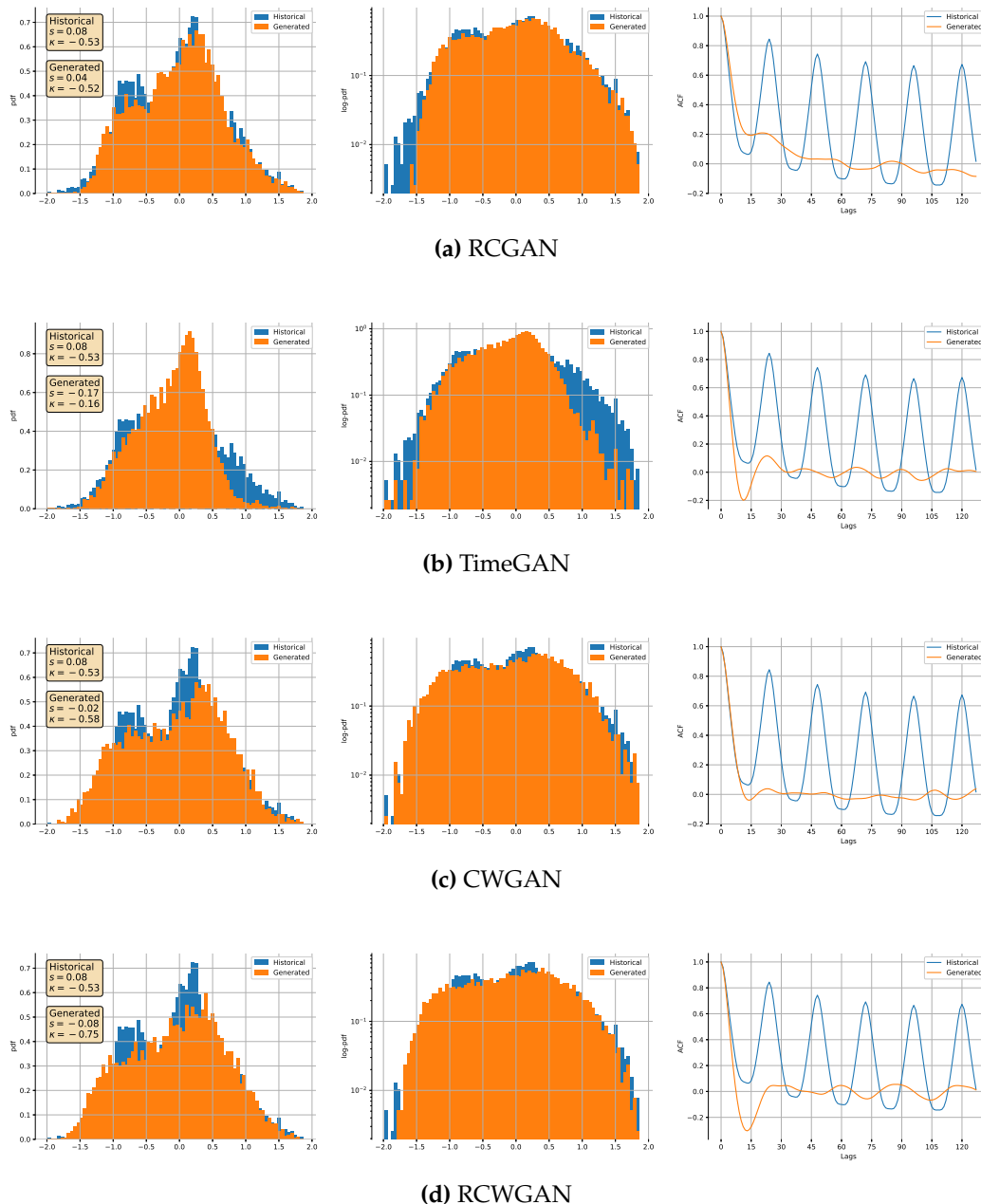


Figure 4. The generated and original load are compared in terms of their marginal distributions using a linear scale (1st column), log-plot (2nd column), and the auto-correlation fit with real load data

Figure 5 presents scenarios generated by the GANs models, namely RCGAN, TimeGAN, CWGAN, and RCWGAN. The figure presents 500 synthetic data generated by these models with gray curves. Also, it includes a randomly selected synthetic data realization for each GAN (orange line) to compare with the real data (blue line) to observe the similarity in behavior between the two. The results show that the synthetic data generated by the GANs are bounded above and below, and none of the generated data is exploding. However, the figure reveals that some GAN-generated data points may have larger maximum and minimum values than the real data. This feature is particularly interesting for risk management analysis, such as controlling whether the electricity provider can handle extreme electricity demand. Additionally, the maximum and minimum electricity consumption values generated by TimeGAN are closer to the real data than the other GANs. Finally, the highlighted path's behavior closely mimics the empirical dataset's behavior.

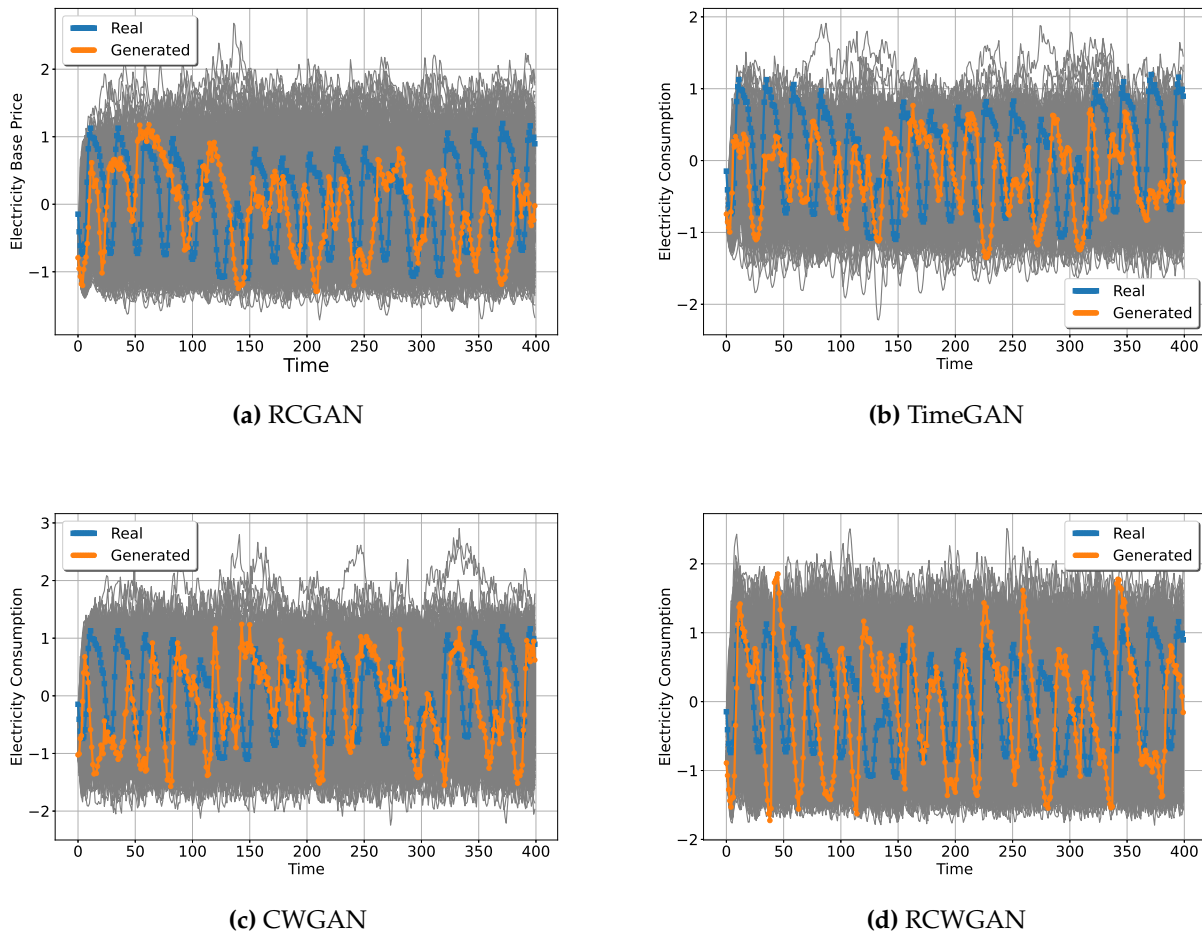


Figure 5. Synthetic load trajectories (orange and gray) generated by GANs and observed load (blue)

Table 3 provides key statistics for real and synthetic electricity consumption data generated by RCGAN, TimeGAN, CWGAN, and RCWGAN. The first column lists the statistical measure of interest: the mean, standard deviation, maximum, and minimum. The subsequent columns show the corresponding values for each real and GANs. The mean of the real historical electricity consumption data is -0.0453 , while the mean of the synthetic data generated by RCWGAN is -0.04467 . This suggests that RCWGAN can generate synthetic data that closely resembles the statistical properties of real data.

Similarly, the standard deviation of the synthetic load data generated by TimeGAN is lower than generated load data by other GANs, implying that TimeGAN produced synthetic load data that is less variable than the others. Although the table presents variations in the statistical properties, these variations are relatively small. Overall, the table provides a helpful summary of the statistical properties of the real and synthetic load data generated by the GANs. However, the table needs to provide more information to compare the success of the GANs. Furthermore, the table presents key statistics for a single synthetic load data. Hence, the comparison can change for other synthetic load data (see Figure 5).

5 Conclusion

In the realm of power grid regulations, precise simulation and prediction of load have become increasingly essential. Therefore, load modeling has been extensively researched using various methods, including regression-based and artificial intelligence (AI) modeling techniques. Over

Table 3. Key statistics of real and synthetic electricity consumption data

	Historical	RCGAN	TimeGAN	CWGAN	RCWGAN
Mean	-0.0453	-0.0043	-0.1320	-0.0436	-0.0467
Std	0.6773	0.6492	0.5111	0.7394	0.7225
Max	1.8637	2.0236	1.7280	2.4780	2.0411
Min	-1.9829	-1.5733	-1.9408	-1.9993	-1.7571

the last decade, AI models have gained significant attention due to their ability to model load without requiring detailed building and environmental parameters. Two primary approaches to AI modeling exist, deep learning and traditional machine learning, which rely heavily on real-time recorded load data. It is undeniable that time-dependent recorded load data serves as a critical source of information for energy market participants.

Having representative and diverse training load data is crucial to achieving good performance from AI models. However, obtaining such data can be challenging, costly, and time-consuming. In cases where there is insufficient load data or the sampling of load data deviates from the observed data distribution, the accuracy of model predictions can be significantly affected. As a result, energy suppliers may experience substantial trading losses, and energy sources may be overused, leading to more significant problems in the long run. Therefore, this paper proposes using GANs for synthetic load data generation. Specifically, it utilizes the RCGAN, TimeGAN, CWGAN, and RCWGAN models in real-world applications, achieving state-of-the-art results for synthetic load data generation. The findings suggest that GANs can be utilized to address data privacy concerns and enhance load modeling efficiency for grid modeling. As shown in Figure 4, the CWGAN and RCWGAN models perform relatively better than the other GANs, with the ability to capture values in the tails. In contrast, the TimeGAN model is unsuccessful in capturing tail values, resulting in a more peaked distribution than the real data distribution.

Future work can explore enhancing GAN efficiency by providing additional information during the training process. The study shows that GANs effectively generate synthetic data for load modeling, enabling risk management and analysis of various scenarios. The significance of this study lies in demonstrating the effectiveness of GANs for modeling electricity consumption patterns, allowing non-academic researchers and institutions to make informed decisions and develop strategies for energy-related challenges.

The results of our study demonstrate that the GANs proposed in this paper can effectively generate synthetic data for load modeling. Therefore, the generated data can be combined with existing empirical demand data to address risk management issues such as extreme demand tests, optimal timing of maintenance for wind turbines, energy efficiency assessments for buildings, and profitability analysis for demand- or time-dependent pricing strategies.

In essence, GANs offer a valuable solution for generating synthetic electricity consumption data, enabling non-academic researchers and institutions to gain insights, conduct simulations, and develop innovative approaches. This study opens up new possibilities for leveraging advanced AI techniques to improve energy management and contribute to a more sustainable and efficient energy future.

Declarations

List of abbreviations

Not applicable.

Ethical approval

The authors state that this research complies with ethical standards. This research does not involve either human participants or animals.

Consent for publication

Not applicable.

Conflicts of interest

The author confirms that there is no competing interest in this study.

Data availability statement

Data availability is not applicable to this article as no new data were created or analysed in this study.

Funding

Not applicable.

Author's contributions

The author has made substantial contributions to the conception, design of the work, the acquisition, analysis, interpretation of data, and the creation of new software used in the work.

Authors' information

Dr. Yilmaz holds an M.Sc. and Ph.D. degree in financial mathematics from the Institute of Applied Mathematics at Middle East Technical University. Currently, Dr. Yilmaz is a Post Doctoral researcher at RPTU Kaiserslautern, Germany.

References

- [1] Moon, J., Jung, S., Park, S. and Hwang, E. Conditional tabular GAN-based two-stage data generation scheme for short-term load forecasting. *IEEE Access*, 8, 205327-205339, (2020). [[CrossRef](#)]
- [2] Arjovsky, M., Chintala, S. and Bottou, L. Wasserstein generative adversarial networks. In *Proceedings, 34th International Conference On Machine Learning (PMLR)*, (Vol. 70), pp. 214-223, (2017, July).
- [3] Gulrajani, I., Ahmed, F., Arjovsky, M., Dumoulin, V. and Courville, A. Improved training of wasserstein gans. In *NeurIPS Proceedings, Advances in Neural Information Processing Systems 30*, (2017).
- [4] Yu, L., Zhang, W., Wang, J. and Yu, Y. SeqGAN: Sequence generative adversarial nets with policy gradient. In *Proceedings, Thirty-First AAAI Conference On Artificial Intelligence*, (Vol. 31, No. 1), pp. 2852-2858, (2017, February). [[CrossRef](#)]
- [5] Zhu, J.Y., Park, T., Isola, P. and Efros, A.A. Unpaired image-to-image translation using cycle-consistent adversarial networks. In *Proceedings, IEEE International Conference on Computer Vision (ICCV)*, pp. 2223-2232, (2017, October). [[CrossRef](#)]
- [6] Bendaoud, N., Farah, N. and Ben Ahmed, S. Comparing generative adversarial networks architectures for electricity demand forecasting. *Energy and Buildings*, 247, 111152, (2021). [[CrossRef](#)]

-
- [7] Silva, V.L., Heaney, C.E., Li, Y. and Pain, C.C. Data assimilation predictive GAN (DA-PredGAN) applied to a spatio-temporal compartmental model in epidemiology. *Journal of Scientific Computing*, 94(1), 25, (2023). [[CrossRef](#)]
- [8] Esteban, C., Hyland, S. and Rättsch, G. Real-valued (medical) time series generation with recurrent conditional gans. *ArXiv Preprint, ArXiv:1706.02633*, (2017). [[CrossRef](#)]
- [9] Yoon, J., Jarrett, D. and Van der Schaar, M. Time-series generative adversarial networks. *Advances In Neural Information Processing Systems*, 32, (2019).
- [10] Yilmaz, B. and Korn, R. Synthetic demand data generation for individual electricity consumers: generative adversarial networks (GANs). *Energy and AI*, 9, 100161, (2022). [[CrossRef](#)]
- [11] Goodfellow, I., Pouget-Abadie, J., Mirza, M., Xu, B., Warde-Farley, D., Ozair, S. et al. Generative adversarial nets. In *NeurIPS Proceedings, Advances in Neural Information Processing Systems 27*, (2014).
- [12] Ramasinghe, S., Khan, S., Barnes, N. and Gould, S. Spectral-GANs for high-resolution 3D point-cloud generation. In *2020 IEEE/RSJ International Conference on Intelligent Robots and Systems (IROS)*, pp. 8169-8176, Las Vegas, NV, USA, (2020, October). [[CrossRef](#)]
- [13] Wang, C., Wang, C., Xu, C. and Tao, D. Tag disentangled generative adversarial networks for object image re-rendering. In *International Joint Conference On Artificial Intelligence (IJCAI)*, Melbourne, Australia, (2017, August). [[CrossRef](#)]
- [14] Tan, W.R., Chan, C.S., Aguirre, H.E. and Tanaka, K. ArtGAN: Artwork synthesis with conditional categorical GANs. In *2017 IEEE International Conference on Image Processing (ICIP)*, pp. 3760-3764, Beijing, China, (2017, September). [[CrossRef](#)]
- [15] Merrigan, A. and Smeaton, A.F. Using a GAN to generate adversarial examples to facial image recognition. *ArXiv Preprint, ArXiv: 2111.15213*, (2021). [[CrossRef](#)]
- [16] Engel, J., Agrawal, K., Chen, S., Gulrajani, I., Donahue, C. and Roberts, A. Gansynth: Adversarial neural audio synthesis. *ArXiv Preprint, ArXiv: 1902.08710*, (2019). [[CrossRef](#)]
- [17] Donahue, C., McAuley, J. and Puckette, M. Adversarial audio synthesis. *ArXiv Preprint, ArXiv: 1802.04208*, (2018). [[CrossRef](#)]
- [18] Young, T., Hazarika, D., Poria, S. and Cambria, E. Recent trends in deep learning based natural language processing. *IEEE Computational Intelligence Magazine*, 13(3), 55-75, (2018). [[CrossRef](#)]
- [19] Englund, C., Aksoy, E.E., Alonso-Fernandez, F., Cooney, M.D., Pashami, S. and Astrand, B. AI perspectives in Smart Cities and Communities to enable road vehicle automation and smart traffic control. *Smart Cities*, 4(2), 783-802, (2021). [[CrossRef](#)]
- [20] Wiese, M., Knobloch, R., Korn, R. and Kretschmer, P. Quant GANs: deep generation of financial time series. *Quantitative Finance*, 20(9), 1419-1440, (2020). [[CrossRef](#)]
- [21] Mao, X., Li, Q., Xie, H., Lau, R.Y., Wang, Z. and Smolley, S.P. Least squares generative adversarial networks. In *Proceedings, IEEE International Conference on Computer Vision (ICCV)*, pp. 2794-2802, (2017, April).
- [22] Mirza, M. and Osindero, S. Conditional generative adversarial nets. *ArXiv Preprint, ArXiv: 1411.1784*, (2014). [[CrossRef](#)]
- [23] Li, J., Wang, X., Lin, Y., Sinha, A. and Wellman, M. Generating realistic stock market order streams. In *Proceedings, Conference on Artificial Intelligence (AAAI)*, (Vol. 34, No. 01), pp. 727-734, (2020, April). [[CrossRef](#)]

- [24] Zhang, K., Zhong, G., Dong, J., Wang, S. and Wang, Y. Stock market prediction based on generative adversarial network. *Procedia Computer Science*, 147, 400-406, (2019). [[CrossRef](#)]
- [25] Koshiyama, A., Firoozye, N. and Treleaven, P. Generative adversarial networks for financial trading strategies fine-tuning and combination. *Quantitative Finance*, 21(5), 797-813, (2021). [[CrossRef](#)]
- [26] Chen, Y., Wang, Y., Kirschen, D. and Zhang, B. Model-free renewable scenario generation using generative adversarial networks. *IEEE Transactions on Power Systems*, 33(3), 3265-3275, (2018). [[CrossRef](#)]
- [27] Li, J., Chen, Z., Cheng, L. and Liu, X. Energy data generation with wasserstein deep convolutional generative adversarial networks. *Energy*, 257, 124694, (2022). [[CrossRef](#)]
- [28] Du, Z., Chen, K., Chen, S., He, J., Zhu, X. and Jin, X. Deep learning GAN-based data generation and fault diagnosis in the data center HVAC system. *Energy and Buildings*, 289, 113072, (2023). [[CrossRef](#)]
- [29] Wang, Z. and Hong, T. Generating realistic building electrical load profiles through the generative adversarial network (GAN). *Energy and Buildings*, 224, 110299, (2020). [[CrossRef](#)]
- [30] Perera, A.T.D., Khayatian, F., Eggimann, S., Orehoung, K. and Halgamuge, S. Quantifying the climate and human-system-driven uncertainties in energy planning by using GANs. *Applied Energy*, 328, 120169, (2022). [[CrossRef](#)]
- [31] Dong, W., Chen, X. and Yang, Q. Data-driven scenario generation of renewable energy production based on controllable generative adversarial networks with interpretability. *Applied Energy*, 308, 118387, (2022). [[CrossRef](#)]
- [32] Chen, Z., Li, J., Cheng, L. and Liu, X. Federated-WDCGAN: A federated smart meter data sharing framework for privacy preservation. *Applied Energy*, 334, 120711, (2023). [[CrossRef](#)]
- [33] Ye, Y., Strong, M., Lou, Y., Faulkner, C.A., Zuo, W. and Upadhyaya, S. Evaluating performance of different generative adversarial networks for large-scale building power demand prediction. *Energy And Buildings*, 269, 112247, (2022). [[CrossRef](#)]
- [34] Sözen, A. and Arcaklioglu, E. Prediction of net energy consumption based on economic indicators (GNP and GDP) in Turkey. *Energy Policy*, 35(10), 4981-4992, (2007). [[CrossRef](#)]
- [35] Hamzaçebi, C. Forecasting of Turkey's net electricity energy consumption on sectoral bases. *Energy Policy*, 35(3), 2009-2016, (2007). [[CrossRef](#)]
- [36] Kankal, M., Akpınar, A., Kömürcü, M.İ. and Özşahin, T.Ş. Modeling and forecasting of Turkey's energy consumption using socio-economic and demographic variables. *Applied Energy*, 88(5), 1927-1939, (2011). [[CrossRef](#)]
- [37] Es, H.A., Kalender Öksüz, F.Y. and Hamzacebi, C. Forecasting the net energy demand of Turkey by artificial neural networks. *Journal of The Faculty of Engineering and Architecture of Gazi University*, 29(3), (2014).
- [38] Ağbulut, Ü. Forecasting of transportation-related energy demand and CO₂ emissions in Turkey with different machine learning algorithms. *Sustainable Production and Consumption*, 29, 141-157, (2022). [[CrossRef](#)]
- [39] Yasin Çodur, M. and Ünal, A. An estimation of transport energy demand in Turkey via artificial neural networks. *Promet-Traffic & Transportation*, 31(2), 151-161, (2019). [[CrossRef](#)]
- [40] Yilmaz, B. Understanding the mathematical background of generative adversarial neural networks (GANs). *Available At SSRN 3981773*, (2021). [[CrossRef](#)]

- [41] Wang, Y. A mathematical introduction to generative adversarial nets (GAN). *ArXiv Preprint, ArXiv: 2009.00169*, (2020). [[CrossRef](#)]
- [42] Ni, H., Szpruch, L., Wiese, M., Liao, S. and Xiao, B. Conditional sig-wasserstein GANs for time series generation. *ArXiv Preprint, ArXiv: 2006.05421*, (2020). [[CrossRef](#)]
- [43] Yukseltan, E., Kok, A., Yucekaya, A., Bilge, A., Aktunc, E.A. and Hekimoglu, M. The impact of the COVID-19 pandemic and behavioral restrictions on electricity consumption and the daily demand curve in Turkey. *Utilities Policy*, 76, 101359, (2022). [[CrossRef](#)]
- [44] Kingma, D.P. and Ba, J. Adam: A method for stochastic optimization. *ArXiv Preprint, ArXiv: 1412.6980*, (2017). [[CrossRef](#)]
- [45] Heusel, M., Ramsauer, H., Unterthiner, T., Nessler, B. and Hochreiter, S. GANs trained by a two time-scale update rule converge to a local nash equilibrium. In *NeurIPS Proceedings, Advances in Neural Information Processing Systems 30*, (2017).
- [46] Paszke, A., Gross, S., Massa, F., Lerer, A., Bradbury, J., Chanan, G. et al. Pytorch: An imperative style, high-performance deep learning library. In *NeurIPS Proceedings, Advances in Neural Information Processing Systems 32*, (2019).

Mathematical Modelling and Numerical Simulation with Applications (MMNSA)
(<https://dergipark.org.tr/en/pub/mmnsa>)



Copyright: © 2023 by the authors. This work is licensed under a Creative Commons Attribution 4.0 (CC BY) International License. The authors retain ownership of the copyright for their article, but they allow anyone to download, reuse, reprint, modify, distribute, and/or copy articles in MMNSA, so long as the original authors and source are credited. To see the complete license contents, please visit (<http://creativecommons.org/licenses/by/4.0/>).

How to cite this article: Yilmaz, B. (2023). Generative adversarial network for load data generation: Türkiye energy market case. *Mathematical Modelling and Numerical Simulation with Applications*, 3(2), 141-158. <https://doi.org/10.53391/mmnsa.1320914>



RESEARCH PAPER

Artificial intelligence-assisted detection model for melanoma diagnosis using deep learning techniques

Hediye Orhan ^{1, ‡} and Emrehan Yavşan ^{2, *, ‡}

¹Department of Computer Engineering, Necmettin Erbakan University, 42140 Konya, Türkiye,

²Department of Electronics and Automation, Tekirdağ Namık Kemal University, Tekirdağ, Türkiye

*Corresponding Author

‡hediyeorhan2015@gmail.com (Hediye Orhan); eyavsan@nku.edu.tr (Emrehan Yavşan)

Abstract

The progressive depletion of the ozone layer poses a significant threat to both human health and the environment. Prolonged exposure to ultraviolet radiation increases the risk of developing skin cancer, particularly melanoma. Early diagnosis and vigilant monitoring play a crucial role in the successful treatment of melanoma. Effective diagnostic strategies need to be implemented to curb the rising incidence of this disease worldwide. In this work, we propose an artificial intelligence-based detection model that employs deep learning techniques to accurately monitor nevi with characteristics that may indicate the presence of melanoma. A comprehensive dataset comprising 8598 images was utilized for the model development. The dataset underwent training, validation, and testing processes, employing the algorithms such as AlexNet, MobileNet, ResNet, VGG16, and VGG19, as documented in current literature. Among these algorithms, the MobileNet model demonstrated superior performance, achieving an accuracy of 84.94% after completing the training and testing phases. Future plans involve integrating this model with a desktop program compatible with various operating systems, thereby establishing a practical detection system. The proposed model has the potential to aid qualified healthcare professionals in the diagnosis of melanoma. Furthermore, we envision the development of a mobile application to facilitate melanoma detection in home environments, providing added convenience and accessibility.

Keywords: Artificial intelligence; deep learning; machine learning; melanoma detection; skin cancer

AMS 2020 Classification: 68T01; 68T07; 68T40; 92B20

1 Introduction

Skin cancer is a disease that can have serious consequences if left untreated. Especially an aggressive type of skin cancer, such as melanoma, can spread quickly and metastasize to other organs. Skin cancer can be fatal if not diagnosed in time and treated appropriately. Because

melanoma is more aggressive than other types of skin cancer and tends to metastasize, treatment becomes more difficult when diagnosed in advanced stages. Even in cases of melanoma treated with early diagnosis, in some cases, the disease can progress and become life-threatening. Because skin cancer can have serious consequences, it is important to take preventive measures by reducing risk factors such as regular skin examinations and sun exposure. Early detection can make treatment more effective and prevent serious consequences. For the early diagnosis of this disease, image processing [1, 2] and deep learning methods can be applied. Many studies have reported the application of artificial intelligence (AI) algorithms in the detection of various types of cancer [3–5], including skin cancer [6, 7].

Yildiz [8], proposes an automatic detection system for melanoma using deep learning methods, specifically model C4Net. Sultana and Puhan [9] review the use of deep learning techniques to detect melanoma from other skin lesions in clinical and dermoscopy images. They emphasized that deep learning techniques outperform traditional methods in skin cancer detection, but data labeling for deep learning techniques is challenging. A similar study to Sultana and Puhan was conducted by Poorna et al. Poorna et al. [10] discuss the development of a computer vision-aided system for the early diagnosis of melanoma, a type of skin cancer. The study compares the accuracy and precision of conventional supervised learning techniques with deep learning-based methods for melanoma detection. Their learning techniques used for the classification were Total Dermoscopic Score, K Nearest Neighbor (KNN) [11–13] and, Support Vector Machine (SVM) [14]. Kwiatkowska et al. [15] detected melanoma from dermoscopic images using ResNet and its different versions. However, higher accuracy rates can be achieved with different models. Shchetinin et al. [16] developed a computer-aided detection system for Melanoma detection with Deep Neural Networks on HAM10000 dataset. By combining multiple dataset instead of a single dataset, a system more suitable for real scenarios can be presented.

In this study, we developed a system for the early detection of melanoma using various deep-learning techniques. The system is tested on a vast dataset. This dataset is a combination of 2 different datasets to increase the reality of the system and its feasibility for clinical applications. Training and testing were performed on a relatively rich dataset in terms of the variety and number of datasets. The presented system will play an active role in the early detection of skin cancer, which is likely to threaten our lives even more in the future, and will contribute to the development of future research on the diagnosis of this disease.

2 General properties of method

Preparing the dataset

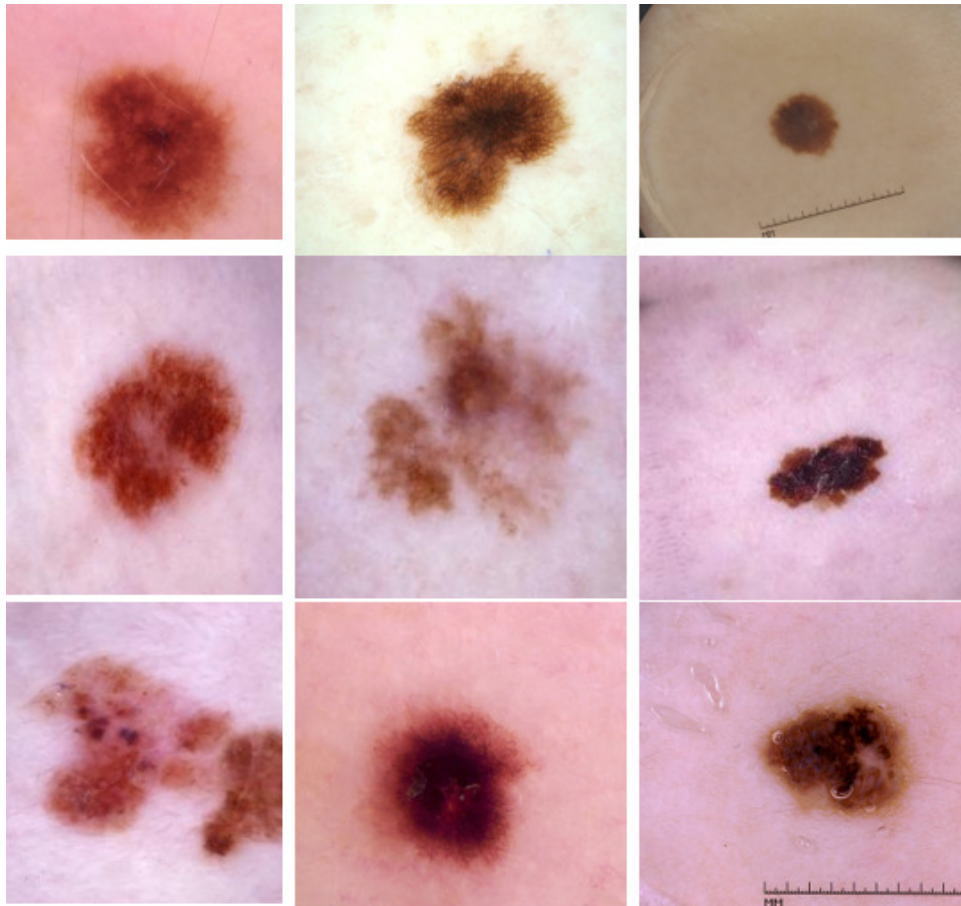
In this study, two different datasets were blended. In this way, a rich dataset was obtained in terms of data diversity. The nevus category data from the first dataset called nevus classifier [17] was added to the new dataset for healthy nevus images. In the second dataset, called skin lesions [18], the data in the melanoma category were added to the same new dataset as melanoma images for cancerous nevus. Thus, a dataset containing healthy, labeled as nevus, and cancerous, labeled as melanoma, nevus images were obtained.

The dataset consists of two classes: nevus and melanoma. The melanoma class represents cancerous mole images and the nevus class represents healthy mole images. There are a total of 8598 data in the dataset. The distribution of the dataset is shown in Table 1. Each class in the dataset is divided into 60% train, 20% test, and 20% validation.

Figure 1 illustrates some of the images in the dataset. In this work, since the dataset is rich and diverse enough, there was no need to augment the data.

Table 1. The data distribution in the dataset

TRAIN	
Melanoma	Nevus
2328	3174
VALIDATION	
Melanoma	Nevus
582	794
TEST	
Melanoma	Nevus
728	992

**Figure 1.** Some of the dataset images

Proposed artificial intelligence models

The proposed AI model for the presented problem is based on a Convolutional Neural Network (CNN). CNNs [19–21] are a deep learning discipline that has proven its success in computer vision and has models designed for various problems. They can be used in vision systems of robots and autonomous vehicles for face [22, 23], object [24] and, traffic sign [25, 26] recognition. A CNN generally consists of Convolution, Pooling, and Fully Connected Layer structures. In a CNN, the image is directly input into the network, followed by several convolution and pooling processes. The outputs of the convolution and pooling processes feed one or more fully connected layers. Eventually, the class label is extracted as an output. Figure 2 depicts a general CNN structure for the detection problem in this paper. The convolutional layers shown in the CNN diagram in Figure 2 serve as feature extractors. Thus, the features of the input images are extracted. Neurons

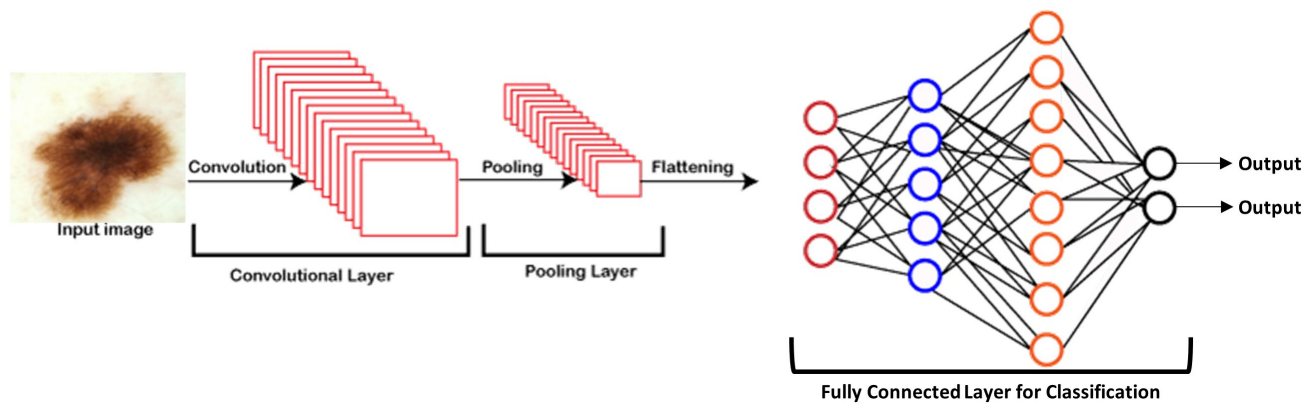


Figure 2. Customized CNN schematic for the classification problem

in the convolutional layers are organized into feature maps. The aim of the pooling layer is to reduce the size (width x height) of the input image. This simplifies the computation for the next layer and also prevents overfitting. Filters similar to those used in the previous layer, convolution, are also used in the pooling layer. In these filters, the image matrix is shifted and the highest value of the pixels (maximum pooling) or the average (average pooling) is calculated. Maximum pooling is often used because it produces higher performance due to the simplicity and rapidity of the process.

The fully connected layer is the last layer of the CNN structure. In the CNN structure, the fully connected layer follows the convolution and pooling layers in succession. A fully connected layer is a standard layer used in classification problems [27]. Convolution and pooling layers can be used many times before reaching the fully connected layer. However, the matrices at the output of the convolution and pooling layers need to be flattened in order to be used in the fully connected layer. Therefore, a flattening layer must be used before the fully connected layer. In the flattening layer, the matrices from the convolution and pooling layers are converted into a vector. This process is called flattening.

For the classification problem in this study; AlexNet, MobileNet, ResNet, VGG16 [28, 29] and VGG19 models were used. These models were adapted to the presented problem by making the revisions indicated in Figure 3. The nevus images obtained from Kaggle were sized 224 x 224 and were input to the models. For each model, sigmoid was chosen as the activation function because it is more suitable for two-class problems. Figure 3 symbolizes the revisions made to the models proposed. In future studies, the softmax activation function may be preferred for classification problems with a larger number of outputs, as in the 1000-class model in Figure 3.

3 Training and performance evaluation of models

The training of the CNN-based models using the sigmoid activation function was performed for various values of the epoch, batch size, and learning rate parameters. For each model, the weights that provided the highest accuracy value on the validation data at the end of the training were determined. The testing process was carried out with these weights. Thus, test performance was improved and over-fitting was prevented. The algorithm memorizes the data in the training set, which is over-fitting. The algorithm that memorizes the training data cannot perform well enough on the test data. Therefore, the determination of the training parameters is crucial. Table 2 lists the models proposed for this work and the parameters used in the training of these models. The learning rate parameters are kept low to prevent over-fitting. Epoch values are set between 10-30. Also, an early stop was included in the algorithm during the training of some of the models. When the training is terminated early (early stop), the training accuracy must be more than 95%.

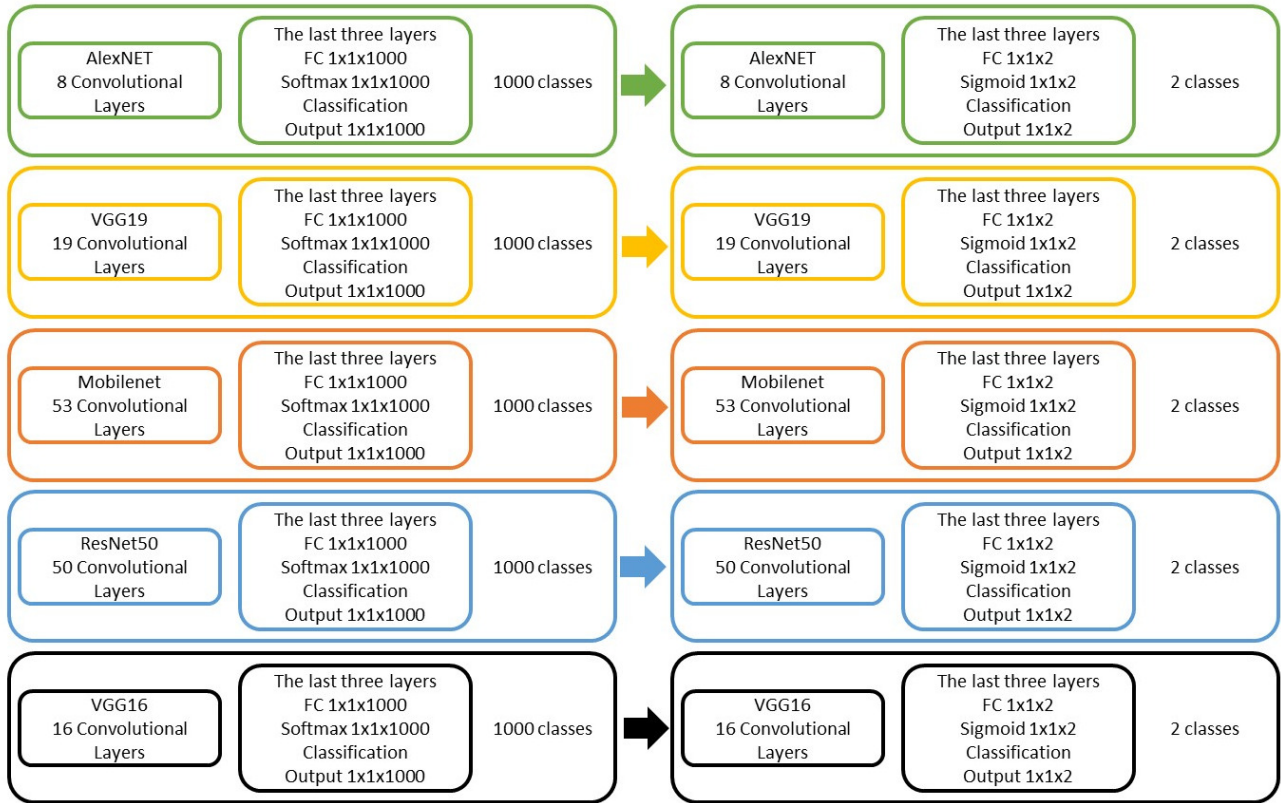


Figure 3. Revised CNN models

The parameters that produce the maximum accuracy on the validation data are assigned after the termination of the training. This is one strategy used to avoid over-fitting.

$$precision = \frac{TP}{TP + FP'} \quad (1)$$

$$recall = \frac{TP}{TP + FN'} \quad (2)$$

$$accuracy = \frac{TP + TN}{TP + FN + TN + FP'} \quad (3)$$

$$specificity = \frac{TN}{TN + FP'} \quad (4)$$

$$F1_{score} = 2 \cdot \frac{precision \cdot recall}{precision + recall} \quad (5)$$

The performance of the proposed models was evaluated through the metrics in Eqs (1) - (5). The

symbols in the metrics can be expressed as 1 and 0 as follows. True Positive (TP) means that the true value is 1 and the predicted value is 1, True Negative (TN) means that the true value is 0 and the predicted value is 0, False Positive (FP) means that the true value is 0 but the predicted value is 1 and False Negative (FN) means that the true value is 1 but the predicted value is 0. The performances of the models are reported in the same list next to the hyper-parameters in Table 2.

Table 2. Hyper-parameters used to train the models and performance metrics presented to evaluate the test performance of the models

Proposed Models	Hyper-parameters for Training			Performance Metrics				
	Epoch	Batch Size	Learning Rate	Accuracy	Precision	Recall	Specificity	F1 Score
AlexNet	30	16	0.00015	0.6767	0.8263	0.5564	0.8406	0.665
MobileNet	10	16	0.000002	0.8494	0.7929	1	0.6442	0.8845
MobileNet	10	8	0.000002	0.8494	0.7929	1	0.6442	0.8845
ResNet	30	16	0.00015	0.8110	0.7683	0.96270	0.6043	0.8545
ResNet	60	16	0.00015	0.8203	0.7729	0.9747	0.6098	0.8622
VGG16	30	16	0.00015	0.8337	0.7936	0.9616	0.6593	0.8696
VGG19	30	16	0.00015	0.8279	0.7979	0.9395	0.6758	0.8629

In neural networks [30, 31], the training parameters are used for high performance, which can be set similarly to the hyper-parameters in Table 2. The absolute minimum value of the error needs to be found. In this process, various optimizers [32–35] are employed to reduce the computational load and minimize losses in the training process. In the present work, Adaptive Moment Estimation (Adam) Optimizer [33] is preferred. Adam algorithm is not only fast but also has low memory usage [36].

MobileNet achieved the highest performance with close to 85% accuracy as a result of the tests of the models on the GPU. Afterwards, the batch size value for the MobileNet model was increased to save time. Figure 4 shows the ROC curve of the model. The area under the curve (AUC) can be considered as an indicator of the model's performance. The higher the AUC, the better the performance of the trained model.

Besides the metrics expressed by Eqs. (1) - (5), the confusion matrix in Table 3 is utilized to evaluate the test performance of the MobileNet model. The confusion matrix is composed of TP, TN, FP and FN values calculated for the testing process.

Table 3. Test performance of the proposed model based on confusion matrix

		Model Prediction	
		Melanoma	Nevus
Actual Output	Melanoma	469 (TN)	259 (FP)
	Nevus	0 (FN)	992 (TP)

The test performance of the proposed model is evaluated on 728 cancerous and 992 healthy nevus images that are not in the training dataset. While the model detected 259 out of 728 melanoma images as healthy, was able to detect all 992 healthy mole images successfully (without failure).

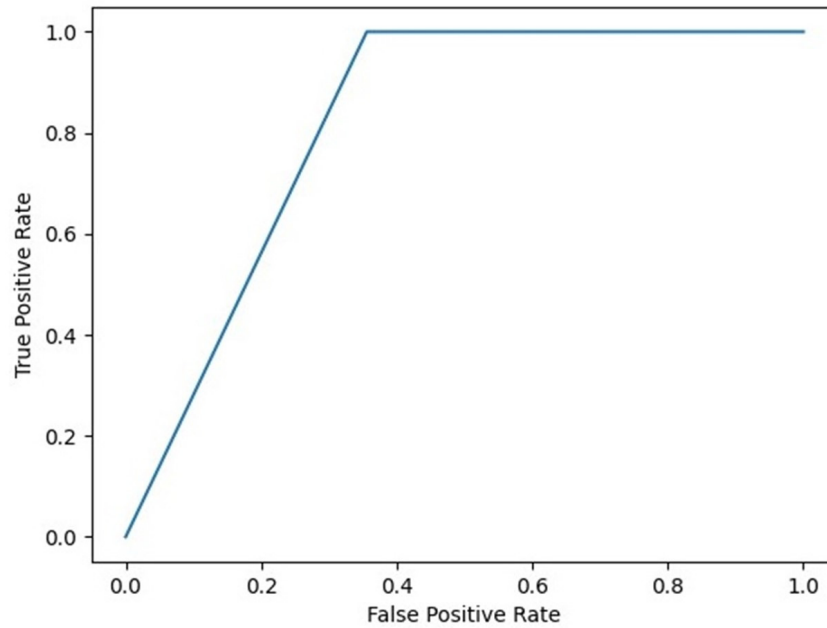


Figure 4. ROC curve of the MobileNet model

4 Results and discussion

In this work, an AI-supported detection model has been developed for skin cancer, the incidence of which is increasing worldwide. AlexNet, MobileNet, ResNet, VGG16 and VGG19 models are employed for the introduced classification problem for the early detection of skin cancer. The proposed models have been trained and tested with a rich data set. The performance of the models has been evaluated based on performance metrics frequently used in the literature. The MobileNet model has offered the highest performance out of these models. The model has achieved 84.94% accuracy after testing.

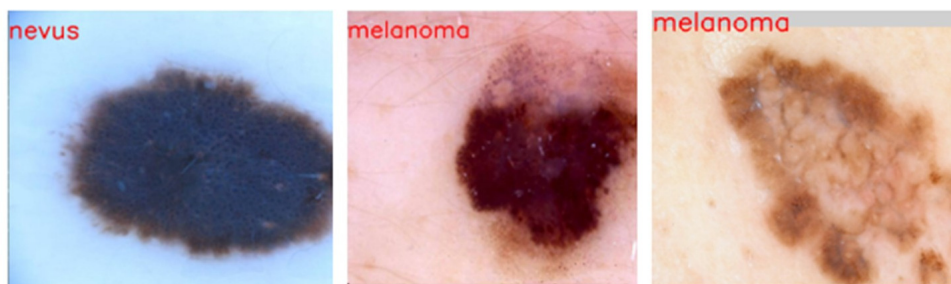


Figure 5. Classification outputs of the model

Table 4 has been prepared to compare the performance of the model with benchmark works in the literature. Successful classifications have been performed with the model file obtained at the end of the training. Also, some of the classified images have been illustrated in Figure 5.

Early diagnosis of skin cancer, aided by these and similar studies, will prevent deaths from this disease. This paper proves that deep learning algorithms can be successfully used in the detection of skin cancer. As the number and diversity of the dataset increase, the success and accuracy of the deep learning model increase. However, labeling the data becomes more difficult. Also, the proposed deep learning models should be considered as an assistant. The use of these models should not be independent of experts, especially in the field of health.

Table 4. Comparison of the model proposed in this study with competitive alternatives in the literature

Studies (Year)	Dataset (Image Counts)	Algorithm	Accuracy
Sultana and Puhan (2018)	ISIC	Deep learning+Sparse Coding +SVM	74.30%
		Deep learning ensemble	80.70%
	Dermofit Image Library	Multi-resolution-tract CNN	79.50%
		Multi-scale feature extraction using full-CNN	81.80%
	MED-NODE (170)	5 layered CNN	81.00%
	MoleMap	ResNet+ bilinear pooling	71.00%
	ISBI 2016 (900)	Fine-tuning using VGGNet	81.30%
		CNN+Fisher Encoding	83.09%
Poorna et al. (2020)	ISIC (1600)	TDS	57.30%
		KNN	66.90%
		SVM	66.35%
Kwiatkowska et al. (2021)	ISIC 2018	ResNet	72.57%
		ResNetXt	77.09%
		SE-ResNet	81.62%
		SE-ResNetXt	0.721 ±0.007
Shchetinin et al. (2021)	HAM10000	InceptionV3	72.20%
		MobileNet	78.20%
Proposed study	Kaggle Datasets (8598)	MobileNet	84.94%

Declarations

Ethical approval

The authors state that this research complies with ethical standards. This research does not involve either human participants or animals.

Consent for publication

Not applicable.

Conflicts of interest

The authors declare that they have no conflict of interest.

Data availability statement

Data availability is not applicable to this article as no new data were created or analysed in this study.

Funding

This research received no specific grant from any funding agency in the public, commercial, or not-for-profit sectors.

Author's contributions

H.O.: Methodology, Software, Conceptualization, Validation, Investigation, Writing - Original Draft, Visualization, Data Curation. E.Y.: Methodology, Conceptualization, Validation, Investigation, Writing - Original Draft, Writing - Review & Editing, Visualization, Supervision, Project Administration. All authors discussed the results and contributed to the final manuscript.

Acknowledgements

Not applicable.

References

- [1] Jain, S. and Pise, N. Computer aided melanoma skin cancer detection using image processing, *Procedia Computer Science*, 48, 735-740, (2015). [[CrossRef](#)]
- [2] Kaymak, R., Kaymak, C. and Ucar, A. Skin lesion segmentation using fully convolutional networks: A comparative experimental study. *Expert Systems with Applications*, 161, 113742, (2020). [[CrossRef](#)]
- [3] Tabrizchi, H., Parvizpour, S. and Razmara, J. An improved VGG model for skin cancer detection. *Neural Processing Letters*, 1-18, (2022). [[CrossRef](#)]
- [4] Kılıç, A.E. and Karakoyun, M. Breast cancer detection using machine learning algorithms. *International Journal of Advanced Natural Sciences and Engineering Researches*, 7(3), 91-95, (2023). [[CrossRef](#)]
- [5] Dildar, M., Akram, S., Irfan, M., Khan, H.U., Ramzan, M., Mahmood, A.R. et al. Skin cancer detection: a review using deep learning techniques. *International Journal of Environmental Research and Public Health*, 18(10), 5479, (2021). [[CrossRef](#)]
- [6] Skin Cancer Foundation. Melanoma. <https://www.skincancer.org/skin-cancer-information/melanoma/>, 2021, Access Date: 13th April 2023.
- [7] American Cancer Society. What Causes Melanoma Skin Cancer? <https://www.cancer.org/cancer/melanoma-skin-cancer/causes-risks-prevention/what-causes.html>, 2022, Access Date: 25th April 2023.
- [8] Yildiz, O. Melanoma detection from dermoscopy images with deep learning methods: A comprehensive study. *Journal of the Faculty of Engineering and Architecture of Gazi University*, 34(4), 1-42, (2019). [[CrossRef](#)]
- [9] Sultana, N.N., Puhan, N.B. Recent deep learning methods for melanoma detection: a review. In *Communications in Computer and Information Science (Mathematics and Computing)* (vol. 834) pp. 118-132, Singapore: Springer, (2018). [[CrossRef](#)]
- [10] Poorna, S.S., Reddy, M.R.K., Akhil, N., Kamath, S., Mohan, L., Anuraj, K. and Pradeep, H.S. Computer vision aided study for melanoma detection: a deep learning versus conventional supervised learning approach. In *Proceedings, Advanced Computing and Intelligent Engineering: Proceedings of ICACIE 2018* (Vol. 1) pp. 75-83, Singapore: Springer, (2020). [[CrossRef](#)]
- [11] Yavşan, E. and Ucar, A. Teaching human gestures to humanoid robots by using Kinect sensor. In *Proceedings, 2015 23rd Signal Processing and Communications Applications Conference (SIU)*, pp. 1208-1211, Malatya, Türkiye, (2015, May). [[CrossRef](#)]
- [12] Yavşan, E. and Ucar, A. Gesture imitation and recognition using Kinect sensor and extreme learning machines. *Measurement*, 94, 852-861, (2016). [[CrossRef](#)]
- [13] Baitu, G.P., Gadalla, O.A.A. and Öztekin, Y.B. Traditional machine learning-based classification of cashew kernels using colour features. *Journal of Tekirdag Agricultural Faculty*, 20(1), 115-124, (2023). [[CrossRef](#)]
- [14] Ucar, A. and Özalp, R. Efficient android electronic nose design for recognition and perception of fruit odors using Kernel Extreme Learning Machines. *Chemometrics and Intelligent Laboratory Systems*, 166, 69-80, (2017). [[CrossRef](#)]
- [15] Kwiatkowska, D., Kluska, P. and Reich, A. Convolutional neural networks for the detection of

- malignant melanoma in dermoscopy images. *Advances in Dermatology and Allergology/Postepy Dermatol Alergol*, 38(3), 412, (2021). [[CrossRef](#)]
- [16] Shchetinin, E.Y., Sevastianov, L.A., Kulyabov, D.S., Ayryan, E.A. and Demidova, A.V. Melanoma detection computer system development with deep neural networks. In *Distributed Computer and Communication Networks: Control, Computation, Communications (Mathematics and Computing)* (vol. 1337) pp. 422-434, Singapore: Springer, (2020). [[CrossRef](#)]
- [17] <https://www.kaggle.com/datasets/mathewmarcum/nevusclassifier>, 2020, Access Date: 22th February 2023.
- [18] <https://www.kaggle.com/datasets/twanderdust/skin-lesion-analysis-toward-melanoma-detection>, 2020, Access Date: 20th February 2023.
- [19] Altekin, F. and Demir, H. Emotion detection from facial expression using different feature descriptor methods with Convolutional Neural Networks. *European Journal of Engineering and Applied Sciences*, 4(1), 14-17, (2021). [[CrossRef](#)]
- [20] Efe, E. and Ozsen, S. CoSleepNet: Automated sleep staging using a hybrid CNN-LSTM network on imbalanced EEG-EOG datasets. *Biomedical Signal Processing and Control*, 80, 104299, (2023). [[CrossRef](#)]
- [21] Tajbakhsh, N., Roth, H., Terzopoulos, D. and Liang, J. Guest editorial annotation-efficient deep learning: the holy grail of medical imaging. *IEEE transactions on medical imaging*, 40(10), 2526-2533, (2021). [[CrossRef](#)]
- [22] Tatar, A.B. Biometric identification system using EEG signals. *Neural Computing and Applications*, 35(1), 1009-1023, (2023). [[CrossRef](#)]
- [23] Ucar, A. Deep Convolutional neural networks for facial expression recognition. In *Proceedings, 2017 IEEE International Conference on Innovations in Intelligent Systems and Applications (INISTA)*, pp. 371-375, Gdynia, Poland, (2017, July). [[CrossRef](#)]
- [24] Aslan, S.N., Özalp, R., Uçar, A. and Güzeliş, C. New CNN and hybrid CNN-LSTM models for learning object manipulation of humanoid robots from demonstration. *Cluster Computing*, 25(3), 1575-1590, (2022). [[CrossRef](#)]
- [25] Küçük, Ö., Gökçe, B. and Yavşan, E. Otonom tabanlı işaret ve şerit tanımak amacı ile bir öğrenme sisteminin geliştirilmesi. *International Journal of Engineering Research and Development*, 13(3), 19-25, (2021). [[CrossRef](#)]
- [26] Uçar, A., Demir, Y. and Güzeliş, C. Object recognition and detection with deep learning for autonomous driving applications. *Simulation*, 93(9), 759-769, (2017). [[CrossRef](#)]
- [27] Basha, S.H.S., Dubey, S.R., Pulabaigari, V. and Mukherjee, S. Impact of fully connected layers on performance of convolutional neural networks for image classification. *Neurocomputing*, 378, 112-119, (2020). [[CrossRef](#)]
- [28] Polat, D.S. and Yavşan, E. Geri dönüşümdeki verimliliği artırmak için yapay zeka destekli atık tespit sistemi. In *Proceedings, 1st International Conference on Engineering, Natural and Social Sciences (ICENSOS 2022)*, pp. 757-761, Konya, Türkiye, (2022, December).
- [29] Orhan, H. and Yavşan, E. A machine learning assisted monitoring system for early detection of melanoma. In *Proceedings, 7th International Conference on Computational Mathematics and Engineering Sciences*, pp. 110, Elazığ, Türkiye, (2023, May).
- [30] Öztürk, P., Alisoy, H. and Mutlu, R. Prediction of CAT 6A U/FTP cable parameters produced by double twist and triple twist machines using artificial neural networks, and comparison of the predicted results. *European Journal of Engineering and Applied Sciences*, 2(2), 41-51, (2019).

- [31] Kara, M.R. and Yavşan, E. Kapasitif bir algılayıcı üzerinden demodülasyon hatalarının yapay sinir ağları kullanılarak düşürülmesi. In Proceedings, *1st International Conference on Engineering and Applied Natural Sciences (ICEANS'22)*, pp. 1705-1708, Konya, Türkiye, (2022, May).
- [32] Reddy, R.V.K., Rao, B.S. and Raju, K.P. Handwritten Hindi digits recognition using convolutional neural network with RMSprop optimization. In Proceedings, *2018 Second International Conference on Intelligent Computing and Control Systems (ICICCS)*, pp. 45-51, Madurai, India, (2018, June). [[CrossRef](#)]
- [33] Bock, S. and Weiß, M. A proof of local convergence for the Adam optimizer. In Proceedings, *2019 International Joint Conference on Neural Networks (IJCNN)*, pp. 1-8, Budapest, Hungary, (2019, July). [[CrossRef](#)]
- [34] Lydia, A. and Francis, S. Adagrad—an optimizer for stochastic gradient descent. *International Journal of Information and Computing Science*, 6(5), 566-568, (2018). [[CrossRef](#)]
- [35] Wang, Y., Liu, J., Mišić, J., Mišić, V.B., Shaohua, L. and Chang, X. Assessing optimizer impact on DNN model sensitivity to adversarial examples. *IEEE Access*, 7, 152766-152776, (2019). [[CrossRef](#)]
- [36] Tato, A., Nkambou, R. Improving Adam optimizer. In Proceedings, *ICLR 2018 Workshop*, (2018). [[CrossRef](#)]

Mathematical Modelling and Numerical Simulation with Applications (MMNSA)

(<https://dergipark.org.tr/en/pub/mmnsa>)



Copyright: © 2023 by the authors. This work is licensed under a Creative Commons Attribution 4.0 (CC BY) International License. The authors retain ownership of the copyright for their article, but they allow anyone to download, reuse, reprint, modify, distribute, and/or copy articles in MMNSA, so long as the original authors and source are credited. To see the complete license contents, please visit (<http://creativecommons.org/licenses/by/4.0/>).

How to cite this article: Orhan, H. & Yavşan, E. (2023). Artificial intelligence-assisted detection model for melanoma diagnosis using deep learning techniques. *Mathematical Modelling and Numerical Simulation with Applications*, 3(2), 159-169. <https://doi.org/10.53391/mmnsa.1311943>



RESEARCH PAPER

A Caputo-Fabrizio fractional-order cholera model and its sensitivity analysis

Idris Ahmed ^{1,*}, Ali Akgül ^{2,3}, Fahd Jarad ⁴, Poom Kumam ⁵ and Kamsing Nonlaopon ⁶

¹Department of Mathematics, Sule Lamido University, Kafin Hausa, Jigawa State, Nigeria,

²Department of Mathematics, Art and Science Faculty, Siirt University, 56100 Siirt, Türkiye,

³Department of Electronics and Communication Engineering, Saveetha School of Engineering,

SIMATS, Chennai, Tamilnadu, India, ⁴Department of Mathematics, Cankaya University, 06790

Etimesgut, Ankara, Türkiye, ⁵KMUTT Fixed Point Research Laboratory, KMUTT-Fixed Point Theory

and Applications Research Group, Department of Mathematics, Faculty of Science, King Mongkut's

University of Technology Thonburi (KMUTT), 126 Pracha-Uthit Road, Thrung Khru, Bangkok 10140,

Thailand, ⁶Department of Mathematics, Khon Kaen University, Khon Kaen 40002, Thailand

*Corresponding Author

†idris.ahmed@slu.edu.ng (Idris Ahmed); aliakgul@siirt.edu.tr (Ali Akgül); fahd@cankaya.edu.tr (Fahd Jarad);
poom.kumam@mail.kmutt.ac.th (Poom Kumam); nkamsi@kku.ac.th (Kamsing Nonlaopon)

Abstract

In recent years, the availability of advanced computational techniques has led to a growing emphasis on fractional-order derivatives. This development has enabled researchers to explore the intricate dynamics of various biological models by employing fractional-order derivatives instead of traditional integer-order derivatives. This paper proposes a Caputo-Fabrizio fractional-order cholera epidemic model. Fixed-point theorems are utilized to investigate the existence and uniqueness of solutions. A recent and effective numerical scheme is employed to demonstrate the model's complex behaviors and highlight the advantages of fractional-order derivatives. Additionally, a sensitivity analysis is conducted to identify the most influential parameters.

Keywords: Cholera; mathematical model; fixed-point theorems; sensitivity analysis; numerical simulations

AMS 2020 Classification: 26A33; 65L03; 39A60

1 Introduction

Cholera is recognized as one of the most dangerous and infectious communicable diseases, which spreads globally and poses a threat to the survival of the human population, rivaling war and

poverty. Infectious diseases exhibit immense diversity, and their outbreaks render millions of people vulnerable to infection, resulting in a significant economic burden on the healthcare system. Cholera is an illness transmitted through water and is characterized by a sudden onset of symptoms, including the presence of large amounts of watery diarrhea. The causative agent of the disease is known as *Vibrio cholerae*, a species of Gram-negative, facultative anaerobic, comma-shaped bacteria belonging to the family Vibrionaceae, with serotypes O1 or O139.

Infection with *V. cholera* can occur through the consumption of unhygienic water or contaminated food. People who are infected with cholera may either display symptoms or remain asymptomatic. Those who show symptoms may experience severe watery stool, vomiting, leg cramps, decreased blood pressure, kidney failure, and loss of body fluids or electrolytes (dehydration). If immediate treatment is not administered to halt these symptoms, they can potentially lead to death [1–4].

The incidence of cholera cases in Africa has been reported by the World Health Organization (WHO, 2021). The epidemic has occurred in two neighboring countries, Niger and Nigeria. In Niger Republic, the regions of Maradi and Zinder have been the most affected by cholera cases. Due to the cross-border movement of populations between these two states and Nigerian communities, many patients have been identified in Nigeria. The WHO announced that the Nigeria Centre for Disease Control (NCDC) has reported a total of 31,425 suspected cases of cholera in Nigeria since the beginning of the year 2021. Out of these cases, 311 have been confirmed, and 816 deaths have been recorded across 22 states and the Federal Capital Territory Abuja (FCT).

In modern times, mathematical modeling plays a vital role in investigating and analyzing the transmission dynamics of diseases, as well as predicting the potential impacts of intervention strategies aimed at controlling their spread. By using mathematical models, researchers can simulate various scenarios, test different interventions, and gain insights into the effectiveness of strategies for disease containment. These models help in making informed decisions and formulating policies to mitigate the dissemination of diseases, [5–11]. In recent years, there has been significant research conducted by numerous authors on the complex dynamics of the Cholera model. Theoretical analyses of such systems have resulted in a multitude of interesting findings, which have been published in various studies [12–15], along with the references cited within those publications. These authors have focused on mathematical models that describe the interactions between populations, contaminated water, and poor sanitation. By exploring these models, valuable insights into the dynamics of Cholera can be gained, contributing to a better understanding of the disease and the development of effective control strategies.

Tilahun et al. [16] developed a stochastic mathematical model to investigate the behavior of cholera disease, with a specific focus on the direct contact transmission pathway. They extensively studied the qualitative and quantitative behavior of the model. Adewole and Faniran [17] developed a human host and environment model to examine the complex dynamics of cholera infection. In their model, they considered the fraction of infectious individuals who do not adhere to treatment as part of the overall human population. Their findings suggest that while compliance with treatment is necessary, it alone is not sufficient to eradicate cholera. These studies contribute to the understanding of cholera dynamics by incorporating various factors and transmission pathways into mathematical models. The results emphasize the importance of considering both direct contact transmission and the impact of treatment adherence in devising effective strategies for cholera control.

Fractional operators, which extend the concept of differentiation and integration to non-integer orders, find extensive applications in various fields of knowledge, including physics, biology, finance, and control theory [18–25]. Their popularity has been on the rise due to their ability to model systems with complex, non-linear, and non-local behavior. One of the main advantages of

fractional operators is their capability to describe systems with memory effects, which are prevalent in physical and biological systems. Additionally, they can effectively capture the behavior of systems with long-range interactions, making them a valuable tool for modeling complex systems [26–36]. In [37], a stochastic computational model of cholera infection was proposed in the context of a direct contact transmission pathway using fractional calculus theory. The research results suggest that policymakers should consider measures such as reducing interactions, improving treatment rates, and enhancing hygiene facilities to eradicate cholera. Baleanu et al. [38] introduced a novel Caputo-Fabrizio fractional model for humans. They utilized the Picard-Lindelöf approach and fixed-point theory to explore the existence of a unique solution. Additionally, the authors demonstrated the superiority of the model over the existing model when compared to real clinical data.

2 Several fundamental concepts

In this section, we will examine some basic concepts of Caputo-Fabrizio fractional operators that are relevant to the theoretical analysis of the proposed model.

Suppose $\mathcal{H}(x_1, x_2) = \{\psi : \psi \in L^2(x_1, x_2), \text{ and } \psi' \in (x_1, x_2)\}$, where $L^2(x_1, x_2)$ is the space of square integrable functions on (x_1, x_2) .

Definition 1 [39] Suppose $\psi \in \mathcal{H}^1(x_1, x_2)$ and $\alpha \in (0, 1)$. Then

$${}^{CF}D_{\kappa}^{\alpha}\psi(\kappa) = \frac{\mathcal{M}(\alpha)}{1-\alpha} \int_{x_1}^{\kappa} \psi'(y) \exp\left[-\alpha \frac{\kappa-y}{1-\alpha}\right] dy, \quad (1)$$

is defined as the Caputo-Fabrizio fractional derivative, where $\mathcal{M}(\alpha)$ is a normalization function with $\mathcal{M}(0) = \mathcal{M}(1) = 1$. In addition, if $\psi \notin \mathcal{H}^1(x_1, x_2)$ then (1) gives

$${}^{CF}D_{\kappa}^{\alpha}\psi(\kappa) = \frac{\alpha\mathcal{M}(\alpha)}{1-\alpha} \int_{x_1}^{\kappa} (\psi(\kappa) - \psi(y)) \exp\left[-\alpha \frac{\kappa-y}{1-\alpha}\right] dy. \quad (2)$$

Remark 1 Setting $p = \frac{1-\alpha}{\alpha} \in (0, \infty)$, then $\alpha = \frac{1}{1+p} \in (0, 1)$. In view of (2), we have

$${}^{CF}D_{\kappa}^{\alpha}\psi(\kappa) = \frac{\mathcal{N}(p)}{p} \int_{x_1}^{\kappa} \psi'(y) \exp\left[\frac{\kappa-y}{p}\right] dy, \quad (3)$$

where $\mathcal{N}(p)$ is a normalization term similar to $\mathcal{M}(\alpha)$ and $\mathcal{N}(0) = \mathcal{N}(\infty) = 1$.

Remark 2 The relation:

$$\lim_{p \rightarrow 0} \frac{1}{p} \exp\left[\frac{\kappa-y}{p}\right] = \delta(y-\kappa), \quad (4)$$

is true, where $\delta(y-\kappa)$ is the Dirac delta function.

Losada and Nioto [39] modified Definition 1, as

$${}^{CF}D_{\kappa}^{\alpha}\psi(\kappa) = \frac{(2-\alpha)}{2(1-\alpha)} \int_{x_1}^{\kappa} \psi'(y) \exp\left[-\alpha \frac{\kappa-y}{1-\alpha}\right] dy, \quad (5)$$

while its corresponding fractional integral is as follows:

Definition 2 Suppose $0 < \alpha < 1$, where α is order of the integral. Then

$${}^{CF}I_{\kappa}^{\alpha}\psi(\kappa) = \frac{2(1-\alpha)}{(2-\alpha)\mathcal{M}(\alpha)}\psi(\kappa) + \frac{2\alpha}{(2-\alpha)\mathcal{M}(\alpha)}\int_0^{\kappa}\psi(y)dy, \quad \kappa \geq x_1, \quad (6)$$

is referred as Caputo-Fabrizio fractional integral of a function ψ .

Remark 3 From (6), the Caputo-Fabrizio fractional integral of a function ψ of order $0 < \alpha < 1$ is a mean between the function ψ and its integral of order one, i.e.,

$$\frac{2(1-\alpha)}{(2-\alpha)\mathcal{M}(\alpha)} + \frac{2\alpha}{(2-\alpha)\mathcal{M}(\alpha)} = 1,$$

thus, $\mathcal{M}(\alpha) = \frac{2}{2-\alpha}$, $0 < \alpha < 1$.

If $\mathcal{M}(\alpha) = \frac{2}{2-\alpha}$, then the new Caputo derivative and its corresponding integral as follows [39]:

Definition 3 Let $0 < \alpha < 1$, then

$${}^{CF}D_{\kappa}^{\alpha}\psi(\kappa) = \frac{1}{1-\alpha}\int_{x_1}^{\kappa}\psi'(y)\exp\left[-\alpha\frac{\kappa-y}{1-\alpha}\right]dx, \quad \kappa \geq x_1, \quad (7)$$

and its fractional integral as:

$${}^{CF}I_{\kappa}^{\alpha}\psi(\kappa) = (1-\alpha)\psi(\kappa) + \alpha\int_{x_1}^{\kappa}\psi(y)dy, \quad \kappa \geq x_1, \quad (8)$$

respectively, are referred as Caputo-Fabrizio fractional derivative and fractional integral of order α of a function ψ .

3 Description of the model

We study the Cholera model as proposed in [40]. The classical Cholera model is formulated by the following system:

$$\begin{aligned} \frac{dS(\kappa)}{d\kappa} &= \Omega - (\lambda I - \mu)S + \eta V + \gamma R, \\ \frac{dI(\kappa)}{d\kappa} &= \lambda SI - (\mu + \omega + \sigma + \beta)I, \\ \frac{dR(\kappa)}{d\kappa} &= \beta I - (\mu + \gamma)R, \\ \frac{dV(\kappa)}{d\kappa} &= \sigma I - \eta V. \end{aligned} \quad (9)$$

Thus, the Caputo-Fabrizio fractional-order model is given by:

$$\begin{aligned} {}^{CF}D^{\alpha}S &= \Omega - \lambda SI - \mu S + \eta V + \gamma R, \\ {}^{CF}D^{\alpha}I &= \lambda SI - \mu I - \omega I - \sigma I - \beta I, \\ {}^{CF}D^{\alpha}R &= \beta I - \mu R - \gamma R, \\ {}^{CF}D^{\alpha}V &= \sigma I - \eta V, \end{aligned} \quad (10)$$

Table 1. States variables

Compartment	Description
S	Susceptible population
I	Symptomatic infected population with Cholera
R	Recovered population
V	Environment

Table 2. Meaning of each parameters.

Parameters	Biological Meanings
Ω	Population recruitment rate
λ	Contact rate
β	Recovery rate
ω	Death rate due infection
γ	Loose of immunity
μ	Natural death rate
σ	Rate of infection among compartment I and V
η	Rate of infection among compartment V and S

subject to

$$S(0) = S_0 \geq 0, I(0) = I_0 \geq 0, R(0) = R_0 \geq 0, \text{ and } V(0) = V_0 \geq 0. \quad (11)$$

Tables 1 and 2 display the biological meaning of each state variable and parameters used in the model, respectively.

4 Qualitative analysis of the model

This section uses fixed point theorems to explore the existence and uniqueness of solutions to the proposed model (10).

Existence and uniqueness result

By utilizing the fixed point theorems, this subsection aims to demonstrate the existence and uniqueness of model (10). To facilitate this analysis, model (10) can be expressed as follows:

$$\begin{aligned} {}^{CF}D^\alpha S &= \mathcal{K}_1(\kappa, S), \\ {}^{CF}D^\alpha I &= \mathcal{K}_2(\kappa, I), \\ {}^{CF}D^\alpha R &= \mathcal{K}_3(\kappa, R), \\ {}^{CF}D^\alpha V &= \mathcal{K}_4(\kappa, V), \end{aligned} \quad (12)$$

where

$$\begin{aligned} \mathcal{K}_1(\kappa, S) &= \Omega - \lambda SI - \mu S + \eta V + \gamma R, \\ \mathcal{K}_2(\kappa, I) &= \lambda SI - \mu I - \omega I - \sigma I - \beta I, \\ \mathcal{K}_3(\kappa, R) &= \beta I - \mu R - \gamma R, \\ \mathcal{K}_4(\kappa, V) &= \sigma I - \eta V. \end{aligned} \quad (13)$$

Applying fractional integral operator given in (6), system (12) reduces to the Volterra integral type of order $(0 < \alpha < 1)$ given by

$$\begin{aligned}
 S(\kappa) &= S(0) + 2\frac{(1-\alpha)}{(2-\alpha)\mathcal{M}(\alpha)}\mathcal{K}_1(\kappa, S) + 2\frac{\alpha}{(2-\alpha)\mathcal{M}(\alpha)}\int_0^\kappa \mathcal{K}_1(y, S)dy, \\
 I(\kappa) &= I(0) + 2\frac{(1-\alpha)}{(2-\alpha)\mathcal{M}(\alpha)}\mathcal{K}_2(\kappa, I) + 2\frac{\alpha}{(2-\alpha)\mathcal{M}(\alpha)}\int_0^\kappa \mathcal{K}_2(y, I)dy, \\
 R(\kappa) &= R(0) + 2\frac{(1-\alpha)}{(2-\alpha)\mathcal{M}(\alpha)}\mathcal{K}_3(\kappa, R) + 2\frac{\alpha}{(2-\alpha)\mathcal{M}(\alpha)}\int_0^\kappa \mathcal{K}_3(y, R)dy, \\
 V(\kappa) &= V(0) + 2\frac{(1-\alpha)}{(2-\alpha)\mathcal{M}(\alpha)}\mathcal{K}_4(\kappa, V) + 2\frac{\alpha}{(2-\alpha)\mathcal{M}(\alpha)}\int_0^\kappa \mathcal{K}_4(y, V)dy.
 \end{aligned}
 \tag{14}$$

Next, under some assumptions, we demonstrate that the kernels $\mathcal{K}_1, \mathcal{K}_2, \mathcal{K}_3$ and \mathcal{K}_4 obey the Lipschitz and contraction conditions. To do so, we state and prove the following lemma.

Lemma 1 *The autonomous system (13) is Lipschitz continuous.*

Proof For S and S^* , we have from (13), gives

$$\begin{aligned}
 \|\mathcal{K}_1(\kappa, S) - \mathcal{K}_1(\kappa, S^*)\| &= \|\lambda I(t)(S(\kappa) - S^*(\kappa)) - \mu(S(\kappa) - S^*(\kappa))\| \\
 &\leq \|\lambda I(\kappa)\| \|S(\kappa) - S^*(\kappa)\| + \mu \|S(\kappa) - S^*(\kappa)\| \\
 &\leq (\epsilon\lambda + \mu) \|S(\kappa) - S^*(\kappa)\| \\
 &\leq l_1 \|S(\kappa) - S^*(\kappa)\|,
 \end{aligned}$$

where $0 < l_1 = (\epsilon\lambda + \mu)$ and $\|I(\kappa)\| \leq \epsilon$ is bounded.

For I and I^* , we have

$$\begin{aligned}
 \|\mathcal{K}_2(\kappa, I) - \mathcal{K}_2(I^*)\| &= \|(\lambda S - \mu - \omega - \sigma - \beta)(I(\kappa) - I^*(\kappa))\| \\
 &\leq (\|\lambda S\| + (\mu + \omega + \sigma + \beta)) \|I(\kappa) - I^*(\kappa)\| \\
 &\leq l_2 \|I(\kappa) - I^*(\kappa)\|,
 \end{aligned}$$

where $0 < l_2 = (\lambda\epsilon_1 + (\mu + \omega + \sigma + \beta))$ and $\|S(\kappa)\| \leq \epsilon_1$ is bounded.

From R and R^* , we have

$$\begin{aligned}
 |\mathcal{K}_3(R) - \mathcal{K}_3(R^*)| &= \|-(\mu + \gamma)(R(\kappa) - R^*(\kappa))\| \\
 &\leq (\mu + \gamma) \|R(\kappa) - R^*(\kappa)\| \\
 &\leq l_3 \|R(\kappa) - R^*(\kappa)\|,
 \end{aligned}$$

where $0 < l_3 = (\mu + \gamma)$.

From V and V^* , we have

$$\begin{aligned}
 |\mathcal{K}_4(V) - \mathcal{K}_4(V^*)| &= \|-\eta(V(\kappa) - V^*(\kappa))\| \\
 &\leq l_4 \|V(\kappa) - V^*(\kappa)\|,
 \end{aligned}$$

where $0 < l_4 = \eta$. Hence it's Lipschitz continuous and the proof of the lemma is complete. ■
 Now, system (14) can be written in recursive form by the difference between the successive terms

as given below:

$$\begin{aligned}
 \chi_{1n} &= S_n(\kappa) - S_{n-1}(\kappa) = \frac{2(1-\alpha)}{(2-\alpha)\mathcal{M}(\alpha)}(\mathcal{K}_1(\kappa, S_{n-1}) - \mathcal{K}_1(\kappa, S_{n-2})) \\
 &\quad + 2\frac{\alpha}{(2-\alpha)\mathcal{M}(\alpha)} \int_0^\kappa (\mathcal{K}_1(\kappa, S_{n-1}) - \mathcal{K}_1(\kappa, S_{n-2}))dy, \\
 \chi_{2n} &= I_n(\kappa) - I_{n-1}(\kappa) = \frac{2(1-\alpha)}{(2-\alpha)\mathcal{M}(\alpha)}(\mathcal{K}_2(\kappa, I_{n-1}) - \mathcal{K}_2(\kappa, I_{n-2})) \\
 &\quad + 2\frac{\alpha}{(2-\alpha)\mathcal{M}(\alpha)} \int_0^\kappa (\mathcal{K}_2(\kappa, I_{n-1}) - \mathcal{K}_2(\kappa, I_{n-2}))dy, \\
 \chi_{3n} &= R_n(\kappa) - R_{n-1}(\kappa) = \frac{2(1-\alpha)}{(2-\alpha)\mathcal{M}(\alpha)}(\mathcal{K}_3(\kappa, R_{n-1}) - \mathcal{K}_3(\kappa, R_{n-2})) \\
 &\quad + 2\frac{\alpha}{(2-\alpha)\mathcal{M}(\alpha)} \int_0^\kappa (\mathcal{K}_3(\kappa, R_{n-1}) - \mathcal{K}_3(\kappa, R_{n-2}))dy, \\
 \chi_{4n} &= V_n(\kappa) - V_{n-1}(\kappa) = \frac{2(1-\alpha)}{(2-\alpha)\mathcal{M}(\alpha)}(\mathcal{K}_4(\kappa, V_{n-1}) - \mathcal{K}_4(\kappa, V_{n-2})) \\
 &\quad + 2\frac{\alpha}{(2-\alpha)\mathcal{M}(\alpha)} \int_0^\kappa (\mathcal{K}_4(\kappa, V_{n-1}) - \mathcal{K}_4(\kappa, V_{n-2}))dy,
 \end{aligned} \tag{15}$$

subject to initial conditions $S_0(\kappa) = S(0)$, $I_0(\kappa) = I(0)$, $R_0(\kappa) = R(0)$, $V_0(\kappa) = V(0)$. From the first equation in (15), taking norm and applying triangular inequality yields:

$$\begin{aligned}
 \|S_n(\kappa) - S_{n-1}(\kappa)\| &= \frac{2(1-\alpha)}{(2-\alpha)\mathcal{M}(\alpha)} \|(\mathcal{K}_1(\kappa, S_{n-1}) - \mathcal{K}_1(\kappa, S_{n-2}))\| \\
 &\quad + 2\frac{\alpha}{(2-\alpha)\mathcal{M}(\alpha)} \int_0^\kappa \|(\mathcal{K}_1(\kappa, S_{n-1}) - \mathcal{K}_1(\kappa, S_{n-2}))\|dy.
 \end{aligned} \tag{16}$$

In view of Lemma 1, we get

$$\begin{aligned}
 \|S_n(\kappa) - S_{n-1}(\kappa)\| &= \frac{2(1-\alpha)}{(2-\alpha)\mathcal{M}(\alpha)} l_1 \|S_{n-1} - S_{n-2}\| \\
 &\quad + \frac{2\alpha}{(2-\alpha)\mathcal{M}(\alpha)} l_1 \int_0^\kappa \|S_{n-1} - S_{n-2}\|dy.
 \end{aligned} \tag{17}$$

Therefore, we obtain

$$\|\chi_{1n}(\kappa)\| \leq \frac{2(1-\alpha)}{(2-\alpha)\mathcal{M}(\alpha)} l_1 \|\chi_{1(n-1)}(\kappa)\| + \frac{2\alpha}{(2-\alpha)\mathcal{M}(\alpha)} l_1 \int_0^\kappa \|\chi_{1(n-1)}(y)\|dy. \tag{18}$$

Thus, the rest of the equations in system (15) can be obtained in the same approach as:

$$\begin{aligned}
 \|\chi_{2n}(\kappa)\| &\leq \frac{2(1-\alpha)}{(2-\alpha)\mathcal{M}(\alpha)} l_1 \|\chi_{2(n-1)}(\kappa)\| + \frac{2\alpha}{(2-\alpha)\mathcal{M}(\alpha)} l_1 \int_0^\kappa \|\chi_{2(n-1)}(y)\|dy, \\
 \|\chi_{3n}(\kappa)\| &\leq \frac{2(1-\alpha)}{(2-\alpha)\mathcal{M}(\alpha)} l_1 \|\chi_{3(n-1)}(\kappa)\| + \frac{2\alpha}{(2-\alpha)\mathcal{M}(\alpha)} l_1 \int_0^\kappa \|\chi_{3(n-1)}(y)\|dy, \\
 \|\chi_{4n}(\kappa)\| &\leq \frac{2(1-\alpha)}{(2-\alpha)\mathcal{M}(\alpha)} l_1 \|\chi_{4(n-1)}(\kappa)\| + \frac{2\alpha}{(2-\alpha)\mathcal{M}(\alpha)} l_1 \int_0^\kappa \|\chi_{4(n-1)}(y)\|dy.
 \end{aligned} \tag{19}$$

Hence, we have

$$\begin{cases} S_n(\kappa) = \sum_{k=1}^n \chi_{1k}(\kappa), \\ I_n(\kappa) = \sum_{k=1}^n \chi_{2k}(\kappa), \\ R_n(\kappa) = \sum_{k=1}^n \chi_{3k}(\kappa), \\ V_n(\kappa) = \sum_{k=1}^n \chi_{4k}(\kappa). \end{cases} \tag{20}$$

The following theorem guarantees the existence of the solution.

Theorem 1 Consider the model given by (10), then there exist a solution if one can find κ_1 for which

$$\frac{2(1-\alpha)}{(2-\alpha)\mathcal{M}(\alpha)}l_k + \frac{2\alpha\kappa_1}{(2-\alpha)\mathcal{M}(\alpha)}l_k < 1, \quad k = 1, 2, \dots, 4,$$

holds.

Proof From Lemma 1 and Eqs. (18) and (19), applying the recursive technique we obtained below:

$$\begin{aligned} \|\chi_{1n}(\kappa)\| &\leq \|S_n(0)\| \left[\frac{2(1-\alpha)}{(2-\alpha)\mathcal{M}(\alpha)}l_1 + \frac{2\alpha\kappa_1}{(2-\alpha)\mathcal{M}(\alpha)}l_1 \right]^n, \\ \|\chi_{2n}(\kappa)\| &\leq \|I_n(0)\| \left[\frac{2(1-\alpha)}{(2-\alpha)\mathcal{M}(\alpha)}l_2 + \frac{2\alpha\kappa_1}{(2-\alpha)\mathcal{M}(\alpha)}l_2 \right]^n, \\ \|\chi_{3n}(\kappa)\| &\leq \|R_n(0)\| \left[\frac{2(1-\alpha)}{(2-\alpha)\mathcal{M}(\alpha)}l_3 + \frac{2\alpha\kappa_1}{(2-\alpha)\mathcal{M}(\alpha)}l_3 \right]^n, \\ \|\chi_{4n}(\kappa)\| &\leq \|V_n(0)\| \left[\frac{2(1-\alpha)}{(2-\alpha)\mathcal{M}(\alpha)}l_4 + \frac{2\alpha\kappa_1}{(2-\alpha)\mathcal{M}(\alpha)}l_4 \right]^n. \end{aligned} \tag{21}$$

This shows that the system solution exists and is continuous. Next, we show that (21) constructs the solution for the model (10), we proceed as follows:

$$\begin{aligned} S(t) - S(0) &= S_n(\kappa) - \mathcal{B}_{1n}(\kappa), \\ I(t) - I(0) &= I_n(\kappa) - \mathcal{B}_{2n}(\kappa), \\ R(t) - R(0) &= R_n(\kappa) - \mathcal{B}_{3n}(\kappa), \\ V(t) - V(0) &= V_n(\kappa) - \mathcal{B}_{4n}(\kappa). \end{aligned} \tag{22}$$

Thus, we obtain

$$\begin{aligned} \|\mathcal{B}_{1n}(\kappa)\| &= \left\| \frac{2(1-\alpha)}{(2-\alpha)\mathcal{M}(\alpha)}(\mathcal{K}_1(\kappa, S) - \mathcal{K}_1(\kappa, S_{n-1})) \right. \\ &\quad \left. + \frac{2\alpha}{(2-\alpha)\mathcal{M}(\alpha)} \int_0^\kappa (\mathcal{K}_1(\kappa, S) - \mathcal{K}_1(\kappa, S_{n-1})) dy \right\| \\ &\leq \frac{2(1-\alpha)}{(2-\alpha)\mathcal{M}(\alpha)} \|(\mathcal{K}_1(\kappa, S) - \mathcal{K}_1(\kappa, S_n))\| \\ &\quad + \frac{2\alpha}{(2-\alpha)\mathcal{M}(\alpha)} \int_0^\kappa \|(\mathcal{K}_1(\kappa, S) - \mathcal{K}_1(\kappa, S_{n-1}))\| dy \\ &\leq \frac{2(1-\alpha)}{(2-\alpha)\mathcal{M}(\alpha)} l_1 \|S - S_{n-1}\| + \frac{2\alpha\kappa}{(2-\alpha)\mathcal{M}(\alpha)} l_1 \|S - S_{n-1}\|. \end{aligned} \tag{23}$$

Repeating the same process as above, we get

$$\|\mathcal{B}_{1n}(\kappa)\| \leq \left(\frac{2(1-\alpha)}{(2-\alpha)\mathcal{M}(\alpha)} + \frac{2\alpha\kappa}{(2-\alpha)\mathcal{M}(\alpha)} \right)^{n+1} l_1^{n+1}b. \tag{24}$$

At κ_1 , we have

$$\|\mathcal{B}_{1n}(\kappa)\| \leq \left(\frac{2(1-\alpha)}{(2-\alpha)\mathcal{M}(\alpha)} + \frac{2\alpha}{(2-\alpha)\mathcal{M}(\alpha)}\kappa_1 \right)^{n+1} l_1^{n+1}b. \tag{25}$$

From (24), as $n \rightarrow \infty$, gives $\|\mathcal{B}_{1n}(\kappa)\| \rightarrow 0$. Similarly,

$$\|\mathcal{B}_{2n}(\kappa)\| \rightarrow 0, \|\mathcal{B}_{1n}(\kappa)\| \rightarrow 0, \|\mathcal{B}_{3n}(\kappa)\| \rightarrow 0, \|\mathcal{B}_{3n}(\kappa)\| \rightarrow 0.$$

Next, to show the solution is unique, suppose that there exist $S_1(\kappa)$, $I_1(\kappa)$, $R_1(\kappa)$, and $V_1(\kappa)$, then

$$\begin{aligned} S(\kappa) - S_1(\kappa) &= \frac{2(1-\alpha)}{(2-\alpha)\mathcal{M}(\alpha)} (\mathcal{K}_1(\kappa, S) - \mathcal{K}_1(\kappa, S_1)) \\ &+ \frac{2\alpha}{(2-\alpha)\mathcal{M}(\alpha)} \int_0^\kappa (\mathcal{K}_1(\kappa, S) - \mathcal{K}_1(\kappa, S_1)) dy. \end{aligned} \tag{26}$$

By taking the norm of (26), and from Lemma 1, we get

$$\begin{aligned} \|S(\kappa) - S_1(\kappa)\| &= \frac{2(1-\alpha)}{(2-\alpha)\mathcal{M}(\alpha)} \|\mathcal{K}_1(\kappa, S) - \mathcal{K}_1(\kappa, S_1)\| \\ &+ \frac{2\alpha}{(2-\alpha)\mathcal{M}(\alpha)} \int_0^\kappa \|\mathcal{K}_1(\kappa, S) - \mathcal{K}_1(\kappa, S_1)\| dy \\ &\leq \frac{2(1-\alpha)}{(2-\alpha)\mathcal{M}(\alpha)} l_1 \|S(\kappa) - S_1(\kappa)\| \\ &+ \frac{2\alpha t}{(2-\alpha)\mathcal{M}(\alpha)} l_1 \|S(\kappa) - S_1(\kappa)\|. \end{aligned} \tag{27}$$

It simplifies to

$$\|S(\kappa) - S_1(\kappa)\| \left(1 - \frac{2(1-\alpha)}{(2-\alpha)\mathcal{M}(\alpha)} l_1 + \frac{2\alpha\kappa}{(2-\alpha)\mathcal{M}(\alpha)} l_1 \right) \leq 0. \tag{28}$$

Theorem 2 *Given that the following inequality*

$$\left(1 - \frac{2(1-\alpha)}{(2-\alpha)\mathcal{M}(\alpha)} l_1 + \frac{2\alpha\kappa}{(2-\alpha)\mathcal{M}(\alpha)} l_1 \right) > 0,$$

holds. Then the solution of model (10) is unique.

Proof Suppose that (28) holds, then

$$\|S(\kappa) - S_1(\kappa)\| \left(1 - \frac{2(1-\alpha)}{(2-\alpha)\mathcal{M}(\alpha)} l_1 + \frac{2\alpha\kappa}{(2-\alpha)\mathcal{M}(\alpha)} l_1 \right) \leq 0. \tag{29}$$

Hence,

$$\|S(\kappa) - S_1(\kappa)\| = 0,$$

which leads to

$$S(\kappa) = S_1(\kappa).$$

Repeating the same techniques above can easily drive similar equality for the rest. Hence, we conclude that the solution is unique. ■

Positivity and boundedness of solution

One of the important characteristics of epidemiological models is that their solutions are both positive and bounded. In order to ensure this, we establish that all of the state variables are non-negative for any time $\kappa > 0$, which implies that a trajectory starting with a positive initial condition will stay positive for all $\kappa > 0$. Thus, system (10) gives

$$\begin{aligned} {}^{CF}D^\alpha S(\kappa)|_{S=0} &= \Omega + \eta V + \gamma R \geq 0, \\ {}^{CF}D^\alpha I(\kappa)|_{I=0} &\geq 0, \\ {}^{CF}D^\alpha R(\kappa)|_{R=0} &= \beta I \geq 0, \\ {}^{CF}D^\alpha V(\kappa)|_{V=0} &= \sigma I \geq 0. \end{aligned} \quad (30)$$

Since $N(\kappa) = S(\kappa) + I(\kappa) + R(\kappa)$ is the total human population. Thus, summing up the first three equations of (10) leads

$${}^{CF}D_{0,\kappa}^\alpha N(\kappa) = \Omega - \mu S - \mu I - \omega I - \sigma I - \mu R \leq \Omega - \mu S, \quad (31)$$

then one has

$$N(\kappa) \leq \left(N(0) - \frac{\Omega}{\mu} \right) E_\alpha(-\mu\kappa) + \frac{\Omega}{\mu}.$$

Thus, we obtain

$$\Theta = \left\{ (S(\kappa), I(\kappa), R(\kappa)) \in \mathbb{R}_+^3 : 0 \leq N(\kappa) \leq \frac{\Omega}{\mu} \right\}, \quad (32)$$

which gives the biologically feasible region for the model (10). Therefore, Θ is positively invariant. Hence, the proposed model (10) is mathematically and epidemiologically well-posed.

5 Sensitivity analysis

We conducted a sensitivity analysis in this section to ascertain the contribution of each parameter to the basic reproduction number (\mathcal{R}_0). This strategy determines the extent to which each parameter value contributes to the \mathcal{R}_0 . Thus,

$$\mathcal{R}_0 = \frac{1}{\mu} (\lambda\Omega - (\mu + \omega + \sigma + \beta)),$$

is the basic reproduction number of model (10); whereas the sensitivity index of the model parameter is given by the relation

$$\Gamma_X^{\mathcal{R}_0} = \frac{\partial \mathcal{R}_0}{\partial X} \times \frac{X}{\mathcal{R}_0}.$$

The sensitivity analysis presented in Table 3 and Figure 1 examines the impact of various

Table 3. Sensitivity analysis of the parameter values

Parameters	Value	Sensitivity value
λ	0.011	0.263839
Ω	0.000096275	0.263839
μ	0.00002536	-1.062007
ω	0.0005	-0.956416
σ	15	-2.3985
β	6	-1.1992

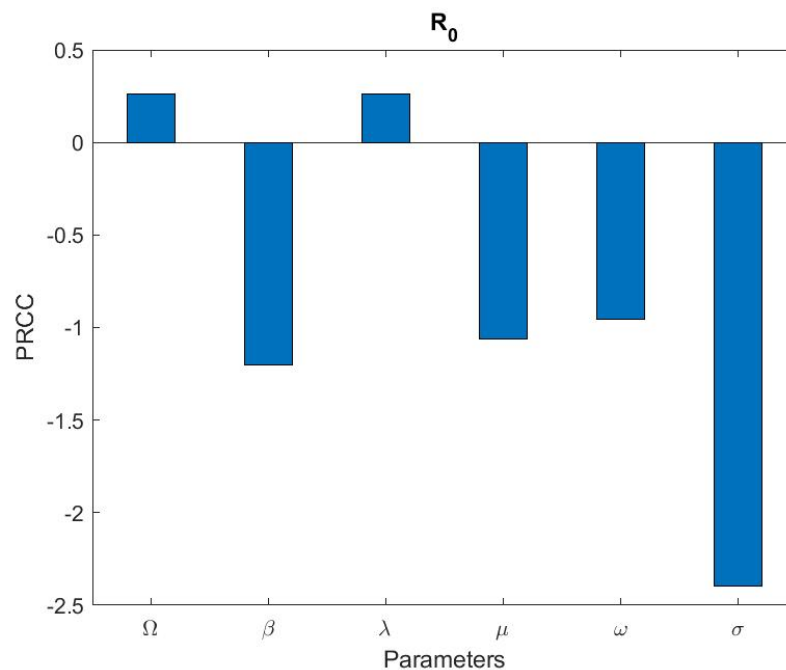


Figure 1. Sensitivity analysis of the parameter values

parameters on the \mathcal{R}_0 . The results show that the recruitment and contact rates are the most sensitive parameters, significantly contributing to the \mathcal{R}_0 increase. This suggests that increasing these parameters will increase the \mathcal{R}_0 . On the other hand, the recovery rate is less sensitive, indicating that an increase in the recovery rate will lead to a decrease in the \mathcal{R}_0 . A response surface plot has been generated to demonstrate how the behavior of \mathcal{R}_0 changes when varying the values of the most sensitive parameters, as shown in Figure 2. Figure 2(a) is the plot of \mathcal{R}_0 versus the rate of infection σ among Infected (I) individuals and Environment (V) and recruitment rate Ω . Figure 2(b) is the plot of \mathcal{R}_0 versus death rate due to infection ω and recruitment rate Ω . Figure 2(c) is the plot of \mathcal{R}_0 versus contact rate λ and recovery rate β . Figure 2(d) is the plot of \mathcal{R}_0 versus contact rate λ and recruitment rate Ω .

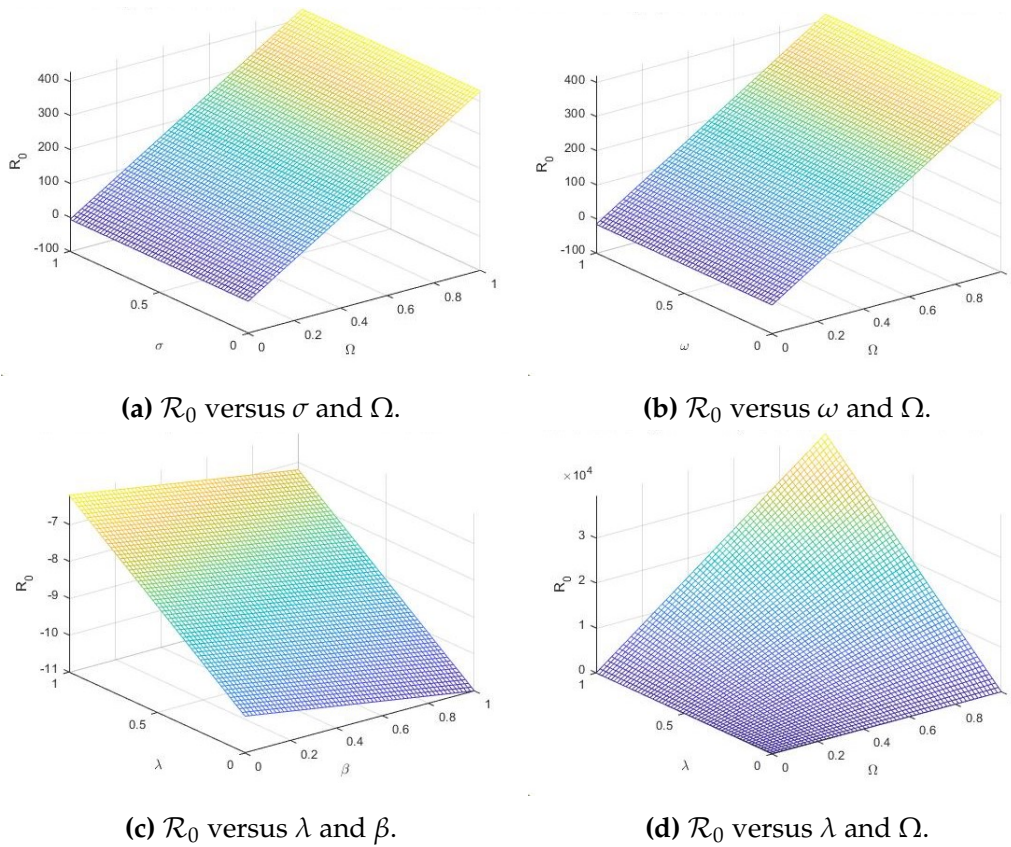


Figure 2. Behavior of \mathcal{R}_0 while varying the value of the most sensitive parameters

6 Numerical simulations and discussions

The classical and fractional-order models need numerical techniques to understand the behavior of the solution trajectories better. Here, we utilized a recent and effective numerical scheme introduced by [41] to gain insight into the solution trajectories. For a detailed analysis of this method's convergence, accuracy, and stability, please refer to [41, 42]. In Table 4, we provided the numerical values of the parameters used to find the proposed model's numerical simulations.

Interestingly, as we varied the fractional order, we observed distinct memory effects in each

Table 4. Parameters values

Parameters	Value
Ω	15
μ	0.02537
ω	0.004
β	0.0064
σ	0.0910
η	0.075
λ	0.061
γ	0.032

compartment, which were not present in the classical model, as shown in Figure 4. Figures 3 and 4 illustrate the dynamical behavior of each compartment in our study. We observed a decrease in the number of susceptible individuals as the number of recovered individuals increased over time. This trend can be attributed to the direct relationship between infectious and recovered individuals.

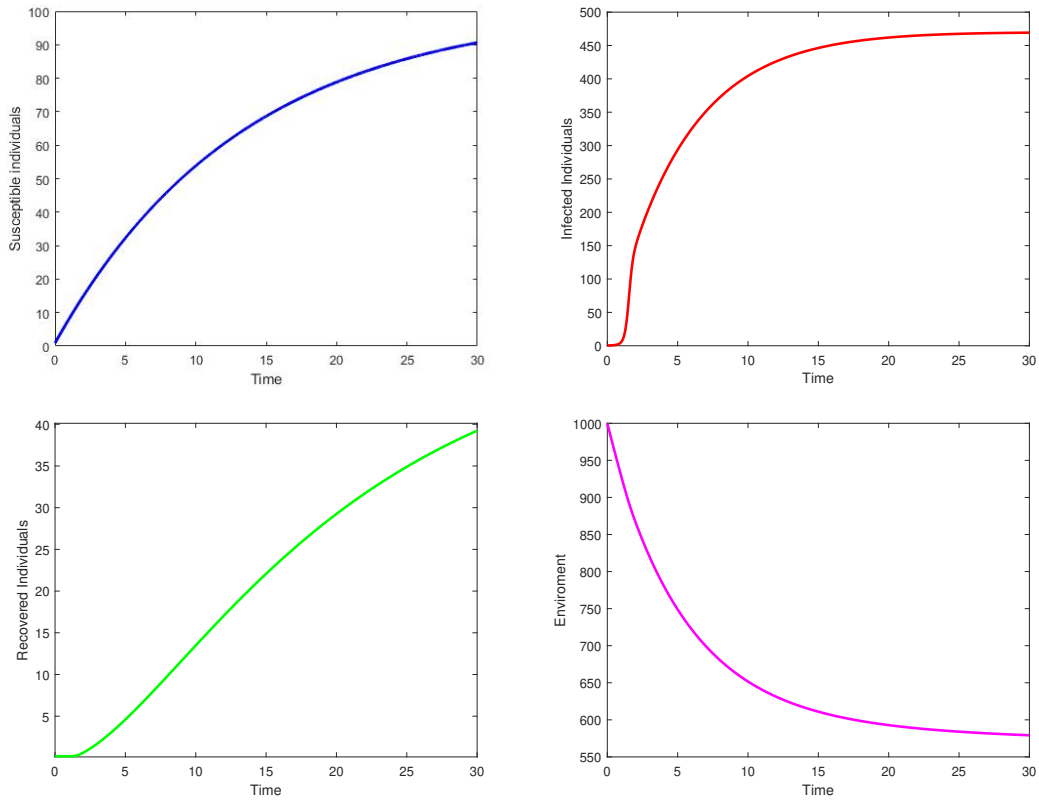


Figure 3. Classical dynamical behavior of each state variable

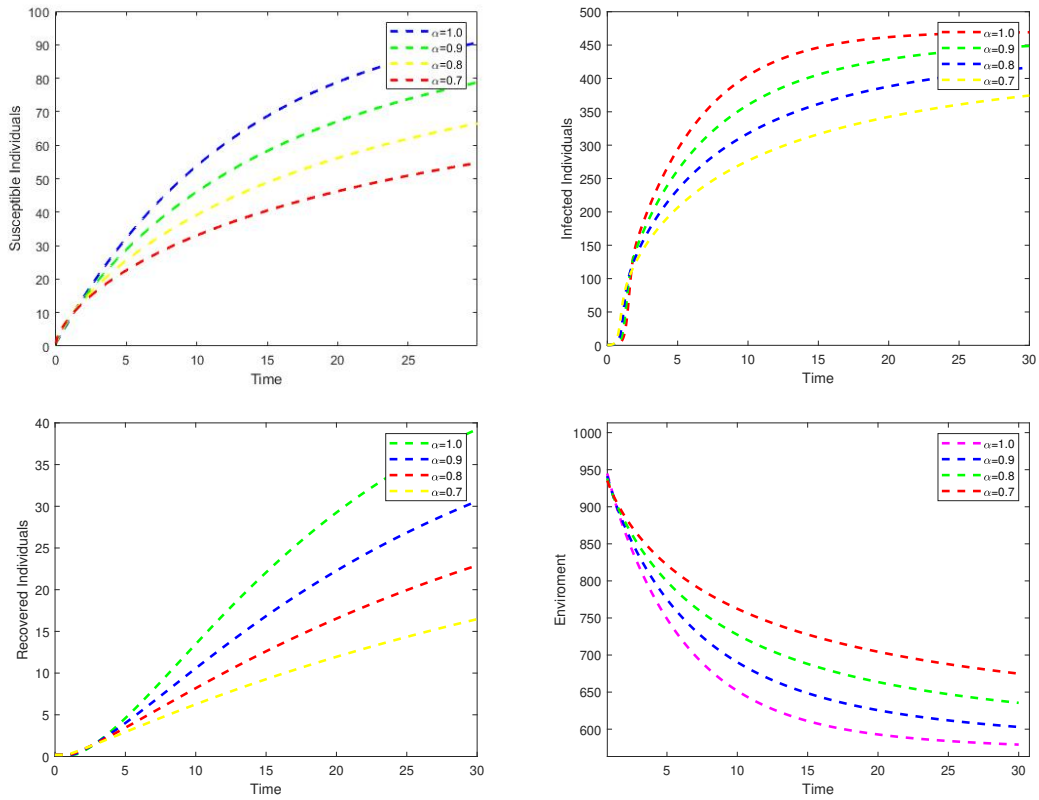


Figure 4. Caputo-Fabrizio fractional-order dynamical behavior of each state variable

Additionally, there was an increase in the concentration of bacteria, which could be linked to the contributions of infectious humans to environmental pollution. Human activities have continued to contaminate the environment, potentially contributing to the exponential increase in bacteria in the environment.

7 Conclusions

In this paper, we have successfully developed a fractional-order Cholera model to investigate the transmission dynamics of the disease using the Caputo-Fabrizio derivative and establish the existence and uniqueness of solutions via fixed point theorems. Furthermore, the sensitivity analysis of the basic reproduction number has highlighted the significant contributions of the parameters associated with the model. Specifically, the results indicate that the recruitment and contact rate are the most sensitive parameters, significantly increasing the \mathcal{R}_0 . We conclude that these findings provide valuable insights into the factors that contribute to the transmission dynamics of cholera and can inform public health policies and strategies for controlling the transmission of the disease.

Moreover, the findings indicate that as the number of infectious individuals in the population decreases, the number of recovered individuals in the system increases. This suggests a correlation between the decline in the infected population and the rise in the number of individuals who have successfully recovered from the disease. Moreover, results suggest that the proposed model provides valuable insights into disease transmission dynamics by utilizing fractional-order derivatives, thus the policymakers can gain a deeper understanding of disease outbreaks and devise effective strategies to manage disease outbreaks.

Declarations

Ethical approval

The authors state that this research complies with ethical standards. This research does not involve either human participants or animals.

Consent for publication

Not applicable.

Conflicts of interest

The authors declare that they have no conflict of interest.

Data availability statement

Data availability is not applicable to this article as no new data were created or analysed in this study.

Funding

This research received no specific grant from any funding agency in the public, commercial, or not-for-profit sectors.

Author's contributions

I.A.: Conceptualization, Methodology, Software, Data Curation, Writing-Original draft preparation, Writing-Reviewing and Editing. A.A.: Conceptualization, Methodology, Software, Data Curation, Writing-Original draft preparation, Visualization, Investigation, Writing-Reviewing and Editing. F.J.: Conceptualization, Methodology, Software, Writing-Reviewing and Editing.

Conceptualization, Methodology, Software, Data Curation, Writing-Original draft preparation, Visualization, Investigation. P.K.: Data Curation, Writing-Original draft preparation, Visualization, Investigation, Writing-Reviewing and Editing. K.N.: Data Curation, Writing-Original draft preparation, Visualization, Investigation, Writing-Reviewing and Editing. All authors discussed the results and contributed to the final manuscript.

Acknowledgements

The authors are thankful for the feedback provided by the anonymous reviewers and editor, which has enhanced the accuracy and readability of the paper. The first author acknowledged the support by Tertiary Education Trust Fund (TETFund) and Sule Lamido University for financial support under Post-Doctoral Fellowship.

References

- [1] Acosta, C.J., Galindo, C.M., Kimario, J., Senkoro, K., Urassa, H., Casals, C. et al. Cholera outbreak in southern Tanzania: risk factors and patterns of transmission. *Emerging Infectious Diseases*, 7, 583-587, (2001). [[CrossRef](#)]
- [2] Luquero, F.J., Rondy, M., Boncy, J., Munger, A., Mekaoui, H., Rymshaw, E. et al. Mortality rates during cholera epidemic, Haiti, 2010–2011. *Emerging Infectious Diseases*, 22(3), 410-416, (2016). [[CrossRef](#)]
- [3] Mgonja, D.S., Massawe, E.S. and Makinde, O.D. Computational modelling of Cholera Bacteriophage with treatment. *Open Journal of Epidemiology*, 5(3), 172-186, (2015). [[CrossRef](#)]
- [4] Moore, M., Gould, P. and Keary, B.S. Global urbanization and impact on health. *International Journal of Hygiene and Environmental Health*, 206(4-5), 269-278, (2003). [[CrossRef](#)]
- [5] Biswas, D. and Pal, S. Role of awareness to control transmission of HIV/AIDS epidemic with treatment and sensitivity analysis. *Journal of Statistics and Management Systems*, 25(3), 617-644, (2022). [[CrossRef](#)]
- [6] Abimbade, S.F., Olaniyi, S., Ajala, O.A. and Ibrahim, M.O. Optimal control analysis of a tuberculosis model with exogenous re-infection and incomplete treatment. *Optimal Control Applications and Methods*, 41(6), 2349-2368, (2020). [[CrossRef](#)]
- [7] Mukandavire, Z., Garira, W. and Tchuente, J.M. Modelling effects of public health educational campaigns on HIV/AIDS transmission dynamics. *Applied Mathematical Modelling*, 33(4), 2084-2095, (2009). [[CrossRef](#)]
- [8] Ahmed, I., Yusuf, A., Ibrahim, A., Kumam, P., and Ibrahim, M. J. A mathematical model of the ongoing coronavirus disease (COVID-19) pandemic: a case study in Turkey. *Science and Technology Asia*, 27(4), 248-258, (2022). [[CrossRef](#)]
- [9] Peter, O.J., Qureshi, S., Yusuf, A., Al-Shomrani, M. and Idowu, A.A. A new mathematical model of COVID-19 using real data from Pakistan. *Results in Physics*, 24, 104098, (2021). [[CrossRef](#)]
- [10] Layton, A.T. and Sadria, M. Understanding the dynamics of SARS-CoV-2 variants of concern in Ontario, Canada: a modeling study. *Scientific Reports*, 12, 2114, (2022). [[CrossRef](#)]
- [11] Duran, S., Durur, H., Yavuz, M. and Yokus, A. Discussion of numerical and analytical techniques for the emerging fractional order murnaghan model in materials science. *Optical and Quantum Electronics*, 55, 571, (2023). [[CrossRef](#)]
- [12] Sun, G.Q., Xie, J.H., Huang, S.H., Jin, Z., Li, M.T. and Liu, L. Transmission dynamics of cholera: mathematical modeling and control strategies. *Communications in Nonlinear Science*

- and *Numerical Simulation*, 45, 235-244, (2017). [[CrossRef](#)]
- [13] Senderovich, Y., Izhaki, I. and Halpern, M. Fish as reservoirs and vectors of *Vibrio cholerae*. *PloS one*, 5(1), e8607, (2010). [[CrossRef](#)]
- [14] Islam, M.S., Zaman, M.H., Islam, M.S., Ahmed, N. and Clemens, J.D. Environmental reservoirs of *Vibrio cholerae*. *Vaccine*, 38, A52-A62, (2020). [[CrossRef](#)]
- [15] Chac, D., Dunmire, C.N., Singh, J. and Weil, A.A. Update on environmental and host factors impacting the risk of *Vibrio cholerae* infection. *ACS Infectious Diseases*, 7(5), 1010-1019, (2021). [[CrossRef](#)]
- [16] Tilahun, G.T., Woldegerima, W.A. and Wondifraw, A. Stochastic and deterministic mathematical model of cholera disease dynamics with direct transmission. *Advances in Difference Equations*, 2020, 670, (2020). [[CrossRef](#)]
- [17] Adewole, M.O. and Faniran, T.S. Analysis of Cholera model with treatment noncompliance. *International Journal of Nonlinear Analysis and Applications*, 13(1), 29-43, (2022). [[CrossRef](#)]
- [18] Diethelm, K. and Ford, N.J. Analysis of fractional differential equations. *Journal of Mathematical Analysis and Applications*, 265(2), 229-248, (2002). [[CrossRef](#)]
- [19] Kilbas, A.A., Srivastava, H.M. and Trujillo, J.J. *Theory and Applications of Fractional Differential Equations* (Vol. 204). Elsevier: Netherlands, (2006).
- [20] Uçar, S., Evirgen, F., Özdemir, N. and Hammouch, Z. Mathematical analysis and simulation of a giving up smoking model within the scope of non-singular derivative. In *Proceedings, Institute of Mathematics and Mechanics, National Academy of Sciences of Azerbaijan* (Vol. 48) pp. 84–99, Baku, Azerbaijan, (2022). [[CrossRef](#)]
- [21] Uçar, S. Existence and uniqueness results for a smoking model with determination and education in the frame of non-singular derivatives. *Discrete and Continuous Dynamical Systems Series S*, 14(7), 2571-2589, (2021). [[CrossRef](#)]
- [22] Uçar, E. and Özdemir, N. A fractional model of cancer-immune system with Caputo and Caputo–Fabrizio derivatives. *The European Physical Journal Plus*, 136, 1-17, (2021). [[CrossRef](#)]
- [23] Yokus, A., Durur, H., Kaya, D., Ahmad, H. and Nofal, T.A. Numerical comparison of Caputo and Conformable derivatives of time fractional Burgers-Fisher equation. *Results in Physics*, 25, 104247, (2021). [[CrossRef](#)]
- [24] Ahmad, S., Dong, Q.I.U. and Rahman, M.U. Dynamics of a fractional-order COVID-19 model under the nonsingular kernel of Caputo-Fabrizio operator. *Mathematical Modelling and Numerical Simulation with Applications*, 2(4), 228-243, (2022). [[CrossRef](#)]
- [25] Atede, A.O., Omame, A. and Inyama, S.C. A fractional order vaccination model for COVID-19 incorporating environmental transmission: a case study using Nigerian data. *Bulletin of Biomathematics*, 1(1), 78-110, (2023). [[CrossRef](#)]
- [26] Ullah, S., Khan, M.A., Farooq, M., Hammouch, Z. and Baleanu, D. A fractional model for the dynamics of tuberculosis infection using Caputo-Fabrizio derivative. *Discrete and Continous Dynamical System Series S*, 13(3), (2020). [[CrossRef](#)]
- [27] Özköse, F., Habbireeh, R. and Şenel, M.T. A novel fractional order model of SARS-CoV-2 and Cholera disease with real data. *Journal of Computational and Applied Mathematics*, 423, 114969, (2023). [[CrossRef](#)]
- [28] Ahmed, I., Goufo, E.F.D., Yusuf, A., Kumam, P., Chaipanya, P. and Nonlaopon, K. An epidemic prediction from analysis of a combined HIV-COVID-19 co-infection model via

- ABC-fractional operator. *Alexandria Engineering Journal*, 60(3), 2979-2995, (2021). [[CrossRef](#)]
- [29] Ahmed, I., Yusuf, A., Sani, M.A., Jarad, F., Kumam, W. and Thounthong, P. Analysis of a Caputo HIV and malaria co-infection epidemic model. *Thai Journal of Mathematics*, 19(3), 897-912, (2021).
- [30] Din, A., Li, Y., Yusuf, A., Liu, J. and Aly, A.A. Impact of information intervention on stochastic hepatitis B model and its variable-order fractional network. *The European Physical Journal Special Topics*, 231, 1859-1873, (2022). [[CrossRef](#)]
- [31] Addai, E., Zhang, L., Preko, A.K. and Asamoah, J.K.K. Fractional order epidemiological model of SARS-CoV-2 dynamism involving Alzheimer's disease. *Healthcare Analytics*, 2, 100114, (2022). [[CrossRef](#)]
- [32] Hanif, A., Butt, A.I.K., Ahmad, S., Din, R.U. and Inc, M. A new fuzzy fractional order model of transmission of Covid-19 with quarantine class. *The European Physical Journal Plus*, 136, 1179, (2021). [[CrossRef](#)]
- [33] Uçar, S., Özdemir, N., Koca, İ. and Altun, E. Novel analysis of the fractional glucose–insulin regulatory system with non-singular kernel derivative. *The European Physical Journal Plus*, 135, 414, (2020). [[CrossRef](#)]
- [34] Duran, S., Yokuş, A. and Durur, H. Surface wave behavior and refraction simulation on the ocean for the fractional Ostrovsky–Benjamin–Bona–Mahony equation. *Modern Physics Letters B*, 35(31), 2150477, (2021). [[CrossRef](#)]
- [35] Durur, H., Yokuş, A. and Yavuz, M. Behavior analysis and asymptotic stability of the traveling wave solution of the Kaup–Kupershmidt equation for conformable derivative. In *Fractional Calculus: New Applications in Understanding Nonlinear Phenomena* (Vol. 3) pp. 162-185, (2022). [[CrossRef](#)]
- [36] Joshi, H., Yavuz, M. and Stamova, I. Analysis of the disturbance effect in intracellular calcium dynamic on fibroblast cells with an exponential kernel law. *Bulletin of Biomathematics*, 1(1), 24-39, (2023). [[CrossRef](#)]
- [37] Rashid, S., Jarad, F., Alsubaie, H., Aly, A.A. and Alotaibi, A. A novel numerical dynamics of fractional derivatives involving singular and nonsingular kernels: designing a stochastic cholera epidemic model. *AIMS Mathematics*, 8(2), 3484-3522, (2023). [[CrossRef](#)]
- [38] Baleanu, D., Jajarmi, A., Mohammadi, H. and Rezapour, S. A new study on the mathematical modelling of human liver with Caputo–Fabrizio fractional derivative. *Chaos, Solitons and Fractals*, 134, 109705, (2020). [[CrossRef](#)]
- [39] Losada, J. and Nieto, J.J. Properties of a new fractional derivative without singular kernel. *Progress in Fractional Differentiation and Applications*, 1(2), 87-92, (2015).
- [40] Eustace, K.A., Osman, S. and Wainaina, M. Mathematical modelling and analysis of the dynamics of cholera. *Global Journal of Pure and Applied Mathematics*, 14(9), 1259-1275, (2018).
- [41] Atangana, A. and Owolabi, K.M. New numerical approach for fractional differential equations. *Mathematical Modelling of Natural Phenomena*, 13(1), 3, (2018). [[CrossRef](#)]
- [42] Evirgen, F., Uçar, E., Uçar, S. and Özdemir, N. Modelling influenza a disease dynamics under Caputo-Fabrizio fractional derivative with distinct contact rates. *Mathematical Modelling and Numerical Simulation with Applications*, 3(1), 58-72, (2023). [[CrossRef](#)]

Mathematical Modelling and Numerical Simulation with Applications (MMNSA)
(<https://dergipark.org.tr/en/pub/mmnsa>)



Copyright: © 2023 by the authors. This work is licensed under a Creative Commons Attribution 4.0 (CC BY) International License. The authors retain ownership of the copyright for their article, but they allow anyone to download, reuse, reprint, modify, distribute, and/or copy articles in MMNSA, so long as the original authors and source are credited. To see the complete license contents, please visit (<http://creativecommons.org/licenses/by/4.0/>).

How to cite this article: Ahmed, I., Akgül, A., Jarad, F., Kumam, P. & Nonlaopon, K. (2023). A Caputo-Fabrizio fractional-order cholera model and its sensitivity analysis. *Mathematical Modelling and Numerical Simulation with Applications*, 3(2), 170-187. <https://doi.org/10.53391/mmnsa.1293162>